Infiltration, Void Formation and Thermal Conductivity Improvement in Thermal Energy Storage Composites of Graphite Foam/Phase Change Materials

by

Mahmoud Moeini Sedeh

A dissertation submitted to the Graduate Faculty of
Auburn University
in partial fulfillment of the
requirements for the Degree of
Doctor of Philosophy

Auburn, Alabama
August 2, 2014

Keywords: Infiltration, Freezing, Melting, Phase Change Materials,
Thermal Conductivity Enhancement, Thermal Energy Storage Composite

Approved by

Jay M. Khodadadi, Chair, Alumni Professor of Mechanical Engineering
W. Robert Ashurst, Associate Professor of Chemical Engineering
Daniel W. Mackowski, Associate Professor of Mechanical Engineering
Brian S. Thurow, Associate Professor of Aerospace Engineering

Abstract

Thermal energy storage (TES) composites open new opportunities in utilization of renewable energies and recycling waste heat. Development, utilization and thermal conductivity improvement of TES composites were investigated in this dissertation. Development of such composites mainly depends on the characteristics of the infiltration process that is linked to the formation of voids and was investigated numerically and experimentally. The numerical investigation was conducted with the purpose of extracting the details of liquid interface evolution and behavior during the infiltration. The penetration of wetting and non-wetting liquids into a porous structure (graphite foam) was studied using the volume-of-fluid (VOF) method. The effects of different driving forces and interface behavior were investigated as well as the observed phenomena during the infiltration of wetting (interface pinning and wicking flow) and non-wetting liquids (void formation). The numerical results were verified against those obtained from the coupled VOF-Level Set method, known to have higher accuracy in capturing the interface. Furthermore, the numerical results of horizontal wicking flow through a network of pores in series were validated against the experimental results with good agreement.

Regarding the utilization of TES composites, the numerical simulation of the phase change processes was performed considering presence of voids and corresponding effects. The proposed combined VOF and enthalpy-porosity method takes into account the variation of density with temperature, making it capable of predicting the shrinkage void. Numerical simulations were conducted at the pore level and the evolution of the freezing and melting fronts were extracted along with the volume of shrinkage void. With regard to verification of results, it was found that

the volume of the shrinkage void is in good agreement with the theoretical volume change due to density variation and its distribution was found in accordance with the observed convection patterns within the pore. During the phase change processes, a temperature gradient was observed along the interface between phase change material (PCM) and void. Therefore, thermocapillary effect was included by considering the variation of the surface tension with temperature. The final status of phase change processes, position and shape of infiltration and shrinkage voids, convection patterns within the pore and phase change duration were extracted and compared between cases with and without thermocapillary convection. It was found that thermocapillary forces influence the convection pattern within the pore and cause a reduction of about 8% in duration of phase change.

As a novel method for thermal characterization of graphite foam/PCM composite, the effective thermal conductivity was investigated numerically and experimentally. A three-dimensional body-centered cube arrangement of uniform spherical pores saturated with PCM was considered as the numerical model. Unidirectional thermal analysis of the model was conducted and the total heat flux was integrated over hot/cold surfaces. Knowing the applied heat flux and temperature difference, the effective thermal conductivity was evaluated based on the Fourier's law. Experimental investigations were conducted on samples of graphite foam and graphite foam/PCM composite using the direct (absolute) method of thermal conductivity measurement. Applying a unidirectional heat flux on the sample, the temperature distribution was measured within the sample and the effective thermal conductivity was evaluated using the direct method, based on the Fourier's law. The numerical and experimental results were found to be in good agreement. It was concluded that highly-conductive and highly-porous structures such as graphite foam are excellent candidates for thermal conductivity improvement of PCM.

Acknowledgments

One of the joys of completion is to look over the journey past and remember all those who have truly supported me along this road. I would like to express my gratitude to my advisor, Professor J. M. Khodadadi, who provided this opportunity for me and his continuous support during the course of study. I would also like to appreciate my PhD Committee members, Professor W. R. Ashurst, Professor D. W. Mackowski and Professor B. S. Thurow, for being great teachers and providing me with constructive feedbacks. I have gained in-depth knowledge from the courses taught by them and I have learned much more through receiving valuable comments during several discussions throughout my PhD which is greatly appreciated here. I am grateful for several thoughtful comments I have received from different experts as reviewers of my work and during the conferences. Thank you for helping me to find the direction of the work with your careful and instructive comments.

I would like to sincerely thank Professor Sushil Bhavnani and Mr. N. Thiagarajan for helping me with sample preparations during my experiments. I would also like to sincerely appreciate Professor German Mills, Mr. M. S. Hossain and Mr. J. R. Darvin from the Department of Chemistry and Biochemistry at Auburn University for providing laboratory facilities and helping me with performing several infiltration and void measurement experiments. I am also very grateful from Dr. M. Miller of the Auburn University Research Institute for Scanning Electron Microscopy (SEM) training and support during my SEM measurements and analysis of the structure of graphite foam samples. My special thanks also go to Professor Jose G.

Vasconcelos in Department of Civil Engineering for serving as the Outside Reader of this dissertation.

I would like to thank all the faculty and graduate students in the NePCM Group (http://nepcm.eng.auburn.edu/) for their collaboration, support and helpful discussions and comments during the review meetings of this project. Furthermore, I appreciate all the faculty and staff in the Department of Mechanical Engineering at Auburn University for their help and support throughout my PhD during different occasions such as meetings, conferences, poster competitions, etc.

This dissertation was funded by the US Department of Energy and I would like to thank this department for supporting the research and development of thermal energy storage systems as a gateway to utilize renewable energy, recycle waste heat and enhance energy efficiency. I would like to acknowledge the Samuel Ginn College of Engineering at Auburn University for their gracious support through Dean's Fellowship. I would also like to acknowledge the Samuel Ginn College of Engineering and Engineering Network Services for providing high performance computing facilities and their continuous support during this course of study. Furthermore, the Department of Mechanical Engineering provided partial financial support which is appreciated here.

I am truly grateful for the kind attention and support of all my colleagues and friends in the Auburn community. I have received encouragements and constructive comments in numerous occasions and through several discussions, for which I am truly grateful. Finally and most importantly, I would like to sincerely express my appreciation to all my family members. I would not have completed this dissertation without their support and patience during these years.

Your continuous encouragements, understanding, kindness and love are invaluable and I always appreciate it affectionately.

This dissertation is based upon work partially supported by the US Department of Energy under Award Number DE-SC0002470. This report was prepared as an account of work sponsored by an agency of the United States Government. Neither the United States Government nor any agency thereof, nor any of their employees makes any warranty, express or implied, or assumes any legal liability or responsibility for the accuracy, completeness, or usefulness of any information, apparatus, product, or process disclosed, or represents that its use would not infringe privately owned rights. Reference herein to any specific commercial product, process, or service by trade name, trademark, manufacturer, or otherwise does not necessarily constitute or imply its endorsement, recommendation, or favoring by the Unites States Government or any agency thereof. The views and opinions of authors expressed herein do not necessarily state or reflect those of the United States Government or any agency thereof.

Table of Contents

List of Tables

List of Figures

List of Symbols

Abbreviations

1D	One-Dimensional
2D	Two-Dimensional
3D	Three-Dimensional
BCC	Body-Centered Cube
CFD	Computational Fluid Dynamics
CICSAM	Compressive Interface Capturing Scheme for Arbitrary Meshes
CPU	Central Processing Unit
CSF	Continuum Surface Force (model)
CVI	Chemical Vapor Infiltrated
CVOFLS	Coupled Volume-of-Fluid / Level-Set Method
DAQ	Data Acquisition
DOE	Department of Energy
HPCC	High-Performance Computing Cluster
LCM	Liquid Composite Molding
LS	Level-Set (method)
NePCM	Nanostructure-enhanced Phase Change Materials
PCM	Phase Change Materials
REV	Representative Elementary Volume

SEM	Scanning Electron Microscope
TEH	Thermo Electric Heater
TES	Thermal Energy Storage
THW	Transient Hot Wire
TPS	Transient Plane Source
US	United States
VOF	Volume of Fluid (method)

Nomenclature

A	mushy zone constant, (5×10^5)
Bo	Bond number, $\rho U/\sigma$
c	specific heat, $J\ kg^{-1}\ K^{-1}$
C_p	specific heat, $J\ kg^{-1}\ K^{-1}$
C_w	Correction of the radius of the capillary (modified Washburn equation), m
Ca	Capillary number, $\mu U/\sigma$
Ca^*	modified Capillary number, $\mu U/(\sigma.\cos\theta)$
d	pore diameter, m
E	energy per unit mass, $J.kg^{-1}$
f_i	body force per unit mass, $N.kg^{-1}$
g	gravitational acceleration, $m\ s^{-2}$
Gr	Grashof number, $g.\beta.(T_h-T_c).d^3/\nu^2$
h	enthalpy, J/kg
I	Identity tensor or electric current, A

k	thermal conductivity, $W\,m^{-1}.K^{-1}$
K	interface curvature, m^{-1}
L	liquid penetration length, m
Ma	Marangoni number, $d\,(d\sigma / dT)\,(T_h - T_c) / (\mu\alpha)$
$\boldsymbol{n_g}$	gravity unit vector
$\boldsymbol{n_t}$	liquid-gas interface tangential unit vector
$\boldsymbol{N_t}$	liquid-gas interface tangential vector, m
p	dimensionless pressure, $Pd^2/(\rho_l.\alpha_l^2)$
P	pressure, $N\,m^{-2}$
Pr	Prandtl number, ν/α
$q"$	heat flux, $W.m^{-2}$
r	radius of the capillary, m
Ra	Rayleigh number, $g\beta(T_h - T_c)d^3/(\alpha\nu)$
Re	Reynolds number, $\rho Ud/\mu$
S_h	volumetric heat source, $W.m^{-3}$
Ste	Stefan number, $c_l.(T_h - T_c)/\Delta h$
t	time, s
T	temperature, K
u_i	velocity components, $m.s^{-1}$
$\boldsymbol{u}$	dimensionless velocity vector, Ud/α_l
$\boldsymbol{U}$	velocity vector, $m\,s^{-1}$
U	velocity, $m\,s^{-1}$
V	electric voltage, V

x_i dimensionless coordinates, X_i / d

X_i Cartesian coordinates, m

Greek Symbols

α volume fraction in chapter 2 or thermal diffusivity in chapter 3 ($m^2\ s^{-1}$)

β thermal expansion coefficient, K^{-1}

δ_{ij} Kronecker delta

Δh latent heat of fusion, J/kg

Δp dimensionless pressure difference

ΔP pressure difference, $N.\ m^{-2}$

ε liquid fraction in solidification

θ wall contact angle in chapter 2 or dimensionless temperature in chapter 3, $(T–T_c)/(T_h–T_c)$

λ dilatational viscosity in chapter 2 ($kg.m^{-1}.s^{-1}$), or volume fraction in chapter 3

μ dynamic viscosity, $kg.m^{-1}.s^{-1}$

ν kinematic viscosity, $m^2\ s^{-1}$

ρ density, $kg.m^{-3}$

$\overline{\rho}$ dimensionless density, $\rho\sigma d / \mu^2$

σ surface tension, $N\ m^{-1}$

τ dimensionless time

τ_{ij} shear stress tensor, $N.m^{-2}$

Subscripts

α	fluid index in the VOF model
avg	average quantity of phases in the VOF method
c	cold (wall thermal boundary condition)
cap	capillary
dyn	dynamic
eff	effective quantities
h	hot (wall thermal boundary condition)
i	fluid index in the VOF method or index for tensor notation
in	inlet
j	fluid index in the VOF method or index for tensor notation
k	index for tensor notation
l	liquid
mz	mushy zone
out	outlet
s	solid
st	surface tension

Superscripts

T	Transpose

Chapter 1 Introduction

The background of the research reported in the present dissertation is discussed in this chapter along with the motivation behind the established objectives and corresponding adopted methods. The structure of the dissertation is then outlined based on the objectives and their priorities.

1.1 Background

The usage of energy has been greatly transformed during the recent years due to growing crises of energy accessibility, increasing demand, environmental issues and global warming. Exploiting/utilizing the existing accessible sources of energy (mainly fossil fuels) more effectively as well as harvesting renewable sources of energy have been the main strategies toward managing the emerging crises. While different processes, energy conversion units and applications are constantly improved to achieve higher energy efficiencies and fuel savings (Diakaki et al., 2008; Popli et al., 2012; Moeini Sedeh and Khodadadi, 2013), growing attention is focused on various sources of renewable energy (Lund, 2007; Shen et al., 2010; Panwar et al., 2011).

Employing renewable sources of energy demands reliable storage/conversion systems due to their intermittent nature and unreliable availability. More specifically, thermal energy storage (TES) and re-use or conversion of thermal energy can play a major role due to the abundance of this form of energy among renewable sources. Furthermore, thermal energy storage can be employed to capture waste heat from different conventional sources and applications for later use

and/or utilization in other applications. This will provide a new balance between energy consumption and demand under higher efficiencies with lowering the energy consumption.

Regardless of the source of the stored energy (renewable or waste heat recovery), TES systems reduce the environmental concerns due to their minimal negative impacts (unlike fossil fuels), and potentially lead to a low-carbon future. Due to energy efficiency and environmental advantages, energy storage in general and thermal energy storage, in particular are known to offer great potentials toward sustainability and energy management. These are the reasons that thermal energy storage attracts more attention among other means of energy storage such as batteries, flywheels and pumped hydro.

1.2 Motivation

As it is shown in figure 1.1, about 22.2%, 18.5% and 31.5% percent of the US energy consumption is related to residential, commercial and industrial sectors, respectively (Annual Energy Reviews 2011, 2012) and about 47, 54 and 23 percent of the energy consumption in these sectors is related to losses and can be greatly reduced by employing energy storage. The large portions of the energy dedicated to these sectors emphasizes the great potential and important role that thermal energy storage might play in fuel saving and energy consumption reduction. There are a variety of industrial/commercial and waste heat recovery applications during which thermal energy can be stored as a sensible or latent heat in a storage medium. In sensible heat storage systems, thermal energy is stored in the storage medium and effectively raises its temperature. Alternately, in latent heat storage systems thermal energy is stored in the storage medium by means of phase change and using the heat of fusion. Latent heat thermal energy storage systems have the advantages of higher energy density and use the phase change processes of melting and freezing to store and extract thermal energy from the storage medium at

a constant temperature. The suitable materials for the storage medium are those with relatively high heat of fusion that can store/release higher energy contents (energy per mass), and are also known as phase change materials (PCM). There are a variety of different PCM such as water, hydrocarbons, fatty acids, salt hydrates, etc. for operation in different ranges of temperature.

Although PCM have relatively high values of heat of fusion, their thermal conductivity is low (especially in liquid phase). This undesirable property negatively affects their performance in TES systems by limiting the achievable heat flux and suppressing charging/discharging rates of energy. To overcome this shortcoming, the thermal conductivity of PCM needs to be improved. Several methods have been proposed for enhancing the thermal conductivity of PCM including introducing high-conductivity fixed structures (Tong et al., 1996; Shatikian et al., 2005; Fan and Khodadadi, 2011) and suspended additives of different shapes and materials (Khodadadi and Hosseinizadeh, 2007; Wang and Mujumdar, 2007).

One of the effective methods in enhancing the thermal conductivity and heat transfer in TES systems is to infiltrate the PCM into a highly-conductive porous structure. Graphite/carbon foams are among the best candidates for developing TES systems and enhancing their performance due to their high thermal conductivity and porosity (which provides high ratio of heat transfer surface to volume). Infiltration of PCM into such porous media will result a TES composite with an improved effective thermal conductivity. Infiltration is a process during which a liquid penetrates into a porous medium and the infiltration rate depends on several properties such as thermo-physical properties of the liquid and porous structure, the structure and size of the pores, the interfacial effects between the liquid and solid walls, etc. However, the infiltration process, as the key process in developing TES composites, is not understood in detail since according to the experimental studies, reported in the literature mainly in the field of liquid

composite molding, it can contribute to undesirable formation of voids that adversely affects the mechanical and thermal properties of the resulting composite.

Furthermore, the utilization of TES composites involves phase change processes including melting and solidification of PCM during charge and discharge of thermal energy. The details of the phase change processes are critical in understanding the behavior and evaluating the performance of TES composites during the freezing/thaw cycles in their lifetime. Thus, such details should be investigated to elucidate the advantages and disadvantages of TES composites. Additionally, there are other concerns such as the influence of voids on the phase change duration, PCM volume change during the phase change, formation of shrinkage voids and thermocapillary effects due to the presence of voids. Understanding the detailed role of such phenomena during phase change processes is critical and possible advantages and disadvantages should be investigated. Finally, an investigation should be devoted to determination of the level of thermal conductivity enhancement in TES composites and thermal characterization of these composites. Most of TES thermal characterizations, reported in the literature, have focused on evaluating the phase change durations or heat transfer rates (or heat flux) during the phase change processes. However, in this dissertation the effective thermal conductivity of TES systems was investigated numerically and experimentally. The need for considering the above-mentioned aspects in developing and utilization TES composites is the motivation toward the objectives and methodology considered in the present research.

1.3 Objectives and Methodology

Based on the discussions in section 1.2, in order to gain a better understanding about the development (infiltration) and utilization (phase change) of TES composites, the following objectives were considered in this dissertation:

1- Investigation of the infiltration process in PCM/graphite foam composites including the relevant phenomena (such as void formation) and determination of the importance of involving parameters (such as various driving forces).
2- Investigation of the phase change processes in PCM/graphite foam composites including solidification and melting and the relevant phenomena (effect of voids).
3- Investigation of the effective thermal conductivity in PCM/graphite foam composites and determination of the level of improvement.

The associated methodologies employed for conducting each objective are as the followings:

1- Numerical investigation of infiltration of liquids into porous structures at pore level using a multi-phase approach to take into account the liquid penetration into pores, initially filled with air. Due to the importance of the infiltration as a key process in developing TES composites, this investigation will be followed by both numerical verification and experimental validation for the obtained results.
2- Numerical investigation of phase change processes (solidification and melting) after infiltration at pore level using a proper approach capable of incorporating volume change and thermocapillary effects during the phase change. A theoretical verification will also be provided for the numerical results obtained from this investigation.
3- Numerical investigation of the effective thermal conductivity in PCM/graphite foam composites using an integrated model of the composite containing both solid (porous structure) and liquid (PCM) components. This effort will be validated experimentally using the absolute (or direct) method of thermal conductivity measurement, known to be appropriate for composite materials.

1.4 Outline of the Dissertation

The literature survey and investigation of infiltration of liquids into porous structures is presented in chapter 2. This study was performed originally using the Volume-of-Fluid (VOF) method approach during which the effect of different driving forces and thermo-physical properties was studied using non-dimensional groups governing the infiltration. The behavior of the interface (shape, position and progress), void formation and the general characteristics of the infiltration (such as infiltration time and its dependence on pore pressure difference) were studied numerically using the VOF method. Due to the importance of liquid interface behavior in infiltration, such behavior was verified numerically using the coupled Level-Set and VOF method which is known to be more accurate in tracking/capturing the liquid interface. Furthermore, wicking flow, as a special case of the infiltration, was investigated experimentally and compared to the numerical results for verification purposes.

Numerical investigation of solidification and melting of PCM is presented in chapter 3 including a literature survey. A combination of the VOF and enthalpy-porosity methods was used to simulate the phase change processes as well as the associated volume change in PCM (i.e. shrinkage and expansion). For verification, the results of shrinkage volume were compared to the theoretical volume change due to different densities between the solid and liquid phases.

Since thermal conductivity enhancement is the main goal of making TES composites, the literature survey and investigation of the effective thermal conductivity of PCM/graphite foam composites is presented in chapter 4. A three-dimensional representative elementary volume (REV) model was developed for the composite and thermal analysis was carried out. An experimental validation was also provided for the effective thermal conductivity using the absolute (direct) method of thermal conductivity measurement. Finally, concluding remarks and further aspects of research in this field are presented in Chapter 5.

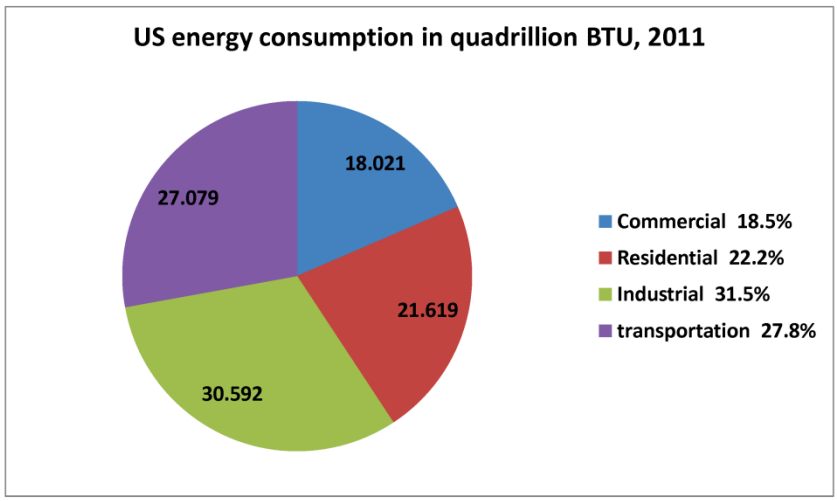

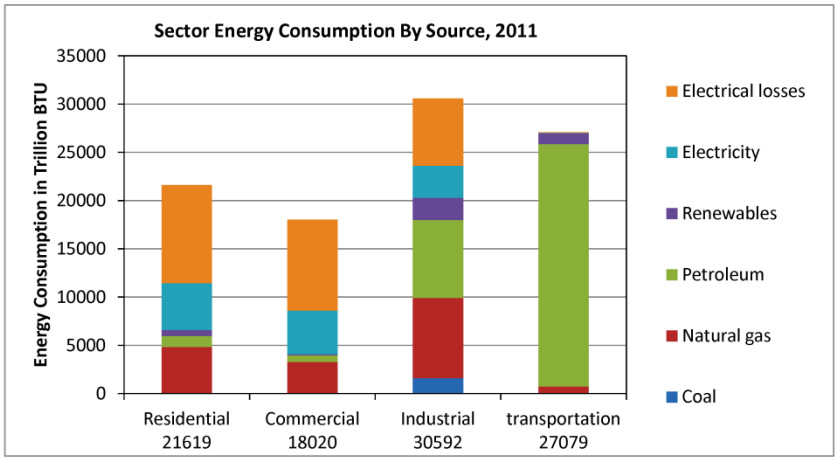

Figure 1.1 US Energy consumption by different sectors (upper) and sector energy consumption by source (lower) in 2011 (reproduced from US Energy Information Administration, Annual Energy Review 2011, 2012)

Chapter 2 Infiltration of Liquids into Porous Structures

Infiltration of liquids into porous structures is investigated at the pore level using a multiphase approach and the detailed findings are presented in this chapter. The importance of different driving forces and the role of the interfacial interactions (surface tension and wall contact angle) are explored. The pertinent phenomena that occur during infiltration are studied and the associated findings are reported. These include detailed information on interface pinning and wicking flow in wetting liquids, as well as pore-level fingering and void formation in non-wetting liquids. Presentation of numerical verification and experimental validation of the results will mark the conclusion of this chapter.

2.1 Introduction

Infiltration of liquids into porous structures is encountered in a wide range of physical phenomena and industrial applications. These include permeation of water through soil and aquifers, extraction of underground oil, filtration, flow through catalyst packings, etc. In particular, infiltration of phase change materials (PCM) in liquid state into high thermal conductivity porous structures (such as graphite foam) is a common approach to enhance the effective thermal conductivity of thermal energy storage (TES) composites (Mills et al., 2006; Fan and Khodadadi, 2011; Liu et al., 2012; Moeini Sedeh and Khodadadi, 2013B). Such porous structures have been used in thermal transport applications due to their high thermal conductivity and high porosity. Thus, investigation of infiltration, as a primary process in development of

TES composites, is crucial in understanding the composition, phase change and thermal behavior of such composite systems.

A numerical approach was proposed to simulate time-dependent evolution of the liquid interface during the infiltration of liquids into porous structures. The method considers the multiphase problem of liquid penetration into the pore(s) initially occupied with air and the simultaneous escape of air. The Volume-of-Fluid (VOF) method was employed using a two-dimensional model of the graphite pore structure. The proposed method is capable of tracking the evolution of liquid interface and yields the infiltration criteria for wetting and non-wetting liquids. Contribution of various driving forces (resulting from pressure gradient, gravity and interfacial effects) to infiltration and interface behavior including the liquid interface shape, position and velocity was investigated. Interface pinning (temporary and permanent) and wicking flow through the pore(s) were identified and studied during infiltration of wetting liquids, whereas pore-level fingering and void formation (entrapment of air within the pore) were observed for non-wetting liquids.

The results of the interface shape and position for infiltration of both wetting and non-wetting liquids were verified against the predictions of the CVOFLS method, another numerical method that is known to be more accurate in interface tracking. Moreover, infiltration of a wetting liquid (cyclohexane) into the porous structure of graphite foam was investigated experimentally through unidirectional horizontal wicking. The numerical results of the liquid penetration length during the wicking flow through a network of pores in series were validated against the experimental results with good agreement. Furthermore, a modified Washburn equation was proposed base on Washburn theory for wicking across horizontal capillaries. Both numerical and experimental results of unidirectional horizontal wicking through graphite foam

are in agreement with the modified Washburn equation. The results of the present study were recently published (Moeini Sedeh and Khodadadi, 2013C).

2.2 Literature Review

Infiltration, as a primary process in developing TES composites, entails penetration of a liquid into a porous structure in which pores are initially filled with a gas (usually air) and is governed by the surface tension, pressure gradient and gravitational effects. For the case of non-wetting liquids, this process can also lead to entrapment of air and formation of voids within the pores of the porous structure. Formation of voids occurs in a variety of applications and processes and has usually undesirable effects on the mechanical and thermal properties of the composite. The early reported results on this topic contain mainly experimental work conducted on visualization of polymer resin flow through glass fiber preforms.

Peterson and Robertson (1991) experimentally investigated the flow characteristics of polymer resin through glass fiber preforms. They found that the flow of the resin and displacement of air (and void formation) were affected by diameter, volume fraction and distribution of fibers. They reported that the shape of the flow front and the size of retained voids are affected by the injection pressure, i.e. pressure gradient.

Mahale et al. (1992) used the matching refractive index technique to visualize the impregnation of non-woven multi-filament glass networks and study the entrapment of air. They carried out forced radial planar impregnation experiments of liquids with different surface tension and viscosity on two different glass mats with different average filament diameters to quantify and map the void content. They found that the void content is a function of the flow capillary number (defined based on the interstitial velocity) and reported a critical capillary number below which the void content increases exponentially by decreasing the capillary

number. They observed negligible entrapment of voids above the reported critical capillary number.

Rohatgi et al. (1993) conducted experiments to correlate the microscale flow behavior and micro and macro-void formation in glass fiber mats in liquid composite molding (LCM). They found that void formation during the flow of liquid through the fiber mats is primarily related to the microscale flow behavior, which in turn depends on liquid properties and the capillary number. Macro-voids were formed between the fiber tows for low capillary numbers (i.e. low flow rates), whereas micro-voids were observed in the fiber tows for high capillary numbers. Fingering at the flow front and transverse flow were the two types of mechanisms that are responsible for formation of macro-voids between the fiber tows. However, they observed different behaviors in axial and transverse flow leading to micro-void formation. In axial flow, a round-up behavior causes the leading flow fronts loop back to meet the lagging flow fronts and form micro-voids. In transverse flow, micro-voids are formed by meeting of the wicking streams from opposite directions. They also found that vacuum-assisted liquid injection reduces the void content.

Patel et al. (1995) performed flow visualization experiments to investigate fiber wetting and void formation mechanism during mold filling. They examined different non-reactive liquids impregnating a unidirectional stitched fiberglass mat to visualize the microscale flow pattern and study the primary and wicking flow fronts in relation to the formation of voids. They found that the fingering phenomenon occurs in fiber mats due to the difference between permeabilities in fiber tows and the gap between the fiber tows. They found the extent of fingering to depend on the capillary number and hydrodynamic pressure. They reported that fingering at the flow front in combination with transverse or cross flow (that happens after fingering due to instabilities in

flow front) lead to formation of voids that are trapped in the fiber mat. They also correlated void formation to the capillary number and the liquid-fiber-air contact angle.

Bickerton and Advani (1997) performed an experimental investigation of isothermal, constant flow rate injection mold filling process during the resin transfer molding in a non-planar geometry. Throughout the mold injection, they observed the 'race tracking phenomenon' during which the resin flow first fills the areas of lower resistance (such as air cavities and some high porosity regions). This phenomenon is in fact fingering in liquid interface in the scale of the pores between fiber tows and causes unexpected deformations of the interface shape which may lead to formation of voids.

These studies revealed that void formation is primarily related to the microscale flow behavior, which in turn depends on liquid properties and the interfacial effects (i.e. capillary number). Fingering at the flow front and transverse flow were the two types of micro-flow mechanisms that are mainly responsible for formation of voids during infiltration of different composite structures. These studies also highlighted the contribution of different driving forces in infiltration including pressure gradient, surface tension and contact angle.

Infiltration and void formation were investigated in a number of studies using simplified mathematical models. Chan and Morgan (1992) developed a model for infiltration and void formation in resin transfer molding of unidirectional composite preforms for the case of resin flow parallel to the fiber axis. Focusing on the flow front, they postulated that the flow front consists of a flow in the direction of fiber tows and a radial flow transverse to the fiber tows. According to this postulation and using the Darcy's law for the flow transverse to the fiber tows, a theoretical formulation was developed. The resulting equations were solved numerically based on the quasi-steady state approximation. They found that for correlating this model with

experimental results especially for slow infiltration rates (i.e. small capillary numbers), the model should be modified to include surface tension effects.

An analytical model was developed by Binetruy et al. (1998) based on the contribution of axial and transverse flow mechanisms for unidirectional impregnation of fiber tows where the flow is parallel to the fiber axis. The model did not take into account the capillary forces; hence, they predicted that the flow front in fiber tows has a pointed meniscus shape. They observed two mechanisms responsible for air entrapment and formation of voids. One mechanism occurs in tow scale (i.e. macro-scale) due to the difference in transverse flow velocity at different points and is responsible for formation of large bubbles (i.e. macro-voids). The second mechanism takes place at the fiber scale (i.e. micro-scale) due to coalescence of the micro-flow fronts and entraps micron-size bubbles.

Spaid and Phelan (1998) used the lattice Boltzmann method for simulating multi-component infiltration and void formation dynamics (entrapment of air) in the microstructure of a fiber preform. Their numerical results for transverse flow over circular porous tows indicated that larger voids are forming as the porosity of the microstructure increases.

Kang et al. (2000) studied formation of micro-voids during the resin transfer molding process. They developed a mathematical model for resin flow within and between tows by approximating the resin velocity within the channels, located between tows, using a shape factor function that depended on the porosity. Using more simplifying assumptions, they modeled the size and number of voids mathematically. However, the model constants should be extracted from experimental results.

Recently, infiltration has been investigated numerically using more inclusive models for a variety of applications. In the field of LCM, infiltration and void formation were investigated by

a number of researchers using the notion of dual-scale porous medium suggested for better understanding of flow front and void formation mechanism (Binetruy et al, 1998; Breard et al., 2003; Simacek and Advani, 2003).

Breard et al. (2003) presented a procedure for mold filling and void formation in LCM. Assuming that the permeability and strain tensor of the porous structure depend on the degree of saturation (i.e. the volume fraction of the pores occupied by resin), they developed a transport equation for the degree of saturation by modifying the continuity and the Darcy's equations. Introducing the notion of dual-scale porous structure and using an experimental pressure field, they were able to solve the derived equation numerically and predict void formation. They also found that the spatial pressure distribution in an unsaturated porous medium varies quadratically, unlike the linear variation predicted by the Darcy's law in a saturated preform.

Simacek and Advani (2003) offered a numerical model to predict fiber tow saturation during the LCM process. The model was developed based on a concept of dual-scale porous medium in which flow through the porous medium was described by the Darcy's law and mass conservation for the flow within the larger pores, while the smaller pores were included as a sink term in the equations. They used a standard finite element/control volume approach to model the sink term for keeping the problem linear and solving the flow explicitly within the time domain. For a one-dimensional linear injection case, the results were in agreement with experimental findings.

Dimitrovova and Advani (2004) conducted numerical simulations at the scale of fiber tows for tracking flow front due to hydrodynamic pressure gradient and capillary action. Their findings indicated that longitudinal wicking flows within intra-tow spaces play an important role

in infiltration and cannot be neglected. They suggested further studies to elucidate the effect and importance of the contact angle.

Soukane and Trochu (2006) used a combination of the Level-Set (LS) and boundary element methods to simulate resin transfer molding and study the motion of the flow front and air entrapment during the mold filling. They utilized the boundary element method to solve the isothermal resin flow governing equation and the LS method to track the flow front in the mold. Several cases of two-dimensional filling with single or multiple injection gates were discussed to determine the ability of this method to predict the position of the flow front and entrapment of air (dry spot formation).

Gourichon et al. (2006) modified the procedure developed by Simacek and Advani (2003) to predict dynamic void content in LCM process. They assumed that the main process of air entrapment occurs within transverse tows. Using one-dimensional elements for axial and transverse tows, they described the air entrapment process by modification of the volume fraction of the one-dimensional elements. They found good agreement in void content with experimentally-measured data for one-dimensional flow. They reported a critical pressure so that when the inlet pressure exceeds it, the resulting elimination of air bubbles will lead to complete saturation of fiber tows (i.e. no void content). Based on the variations in local void content, they concluded that the void content should be considered on both macro- and micro-scales. As a further validation, Gourichon et al. (2008) conducted an experimental analysis of radial flow to analyze the formation of voids and found good agreement between numerical and experimental pressure profiles.

Lee et al. (2006) proposed a numerical method for analysis and control of the formation and transport of voids during the mold filling process. The flow front was detected by solving

flow equations considering a macroscopic flow model for mass-momentum balance of resin flow within the mold combined with a microscopic flow model for resin flow within and between tows. They also detected the flow front experimentally using optical sensors for verification purposes.

Yamaleev and Mohan (2006) developed a numerical model illustrating the microscopic isothermal flow perpendicular to a fiber tow under a high external fluid pressure to study the effect of phase transition on flow behavior and void formation during the liquid molding process. Their model takes into account the entrapment of air as well as liquid/vapor phase transition occurring in entrapped bubbles within the tows (using the Peng–Robinson equation of state). They found that the condensation of the resin and water vapors, which occurs under high external pressures during infiltration process, reduces the void size considerably as compared to that of a perfect gas. They concluded that the phase transition inside the fiber tow affects the void size, and the void dynamics depends on the thermodynamic properties of the entrapped gas and the surrounding liquid.

Schell et al. (2007) investigated the evolution of meso-scale voids in LCM numerically and experimentally. In extending the numerical model of Gourichon et al. (2006), they used a combination of one-dimensional elements to represent transverse bundles and two-dimensional elements to represent the inter-bundle spaces and the longitudinal fiber bundles. They found that capillary pressure becomes the dominant force for tow impregnation when resin pressure gradient is low. Therefore, meso-scale voids form in moderate pressure gradients in contrast to micro-voids that are created at high pressure gradients. Moreover, they determined the void content as a function of the modified capillary number, Ca*.

The effects of different parameters, such as contact angle, on infiltration were studied by a number of researchers through theoretical analysis. Landeryou et al. (2005) developed similarity solutions for growth of wetted regions resulting from wicking from a saturated line or a constant-flux line source characterized by the strength of the source, gravitational and capillary forces. They reported a good agreement with experimental results. Using a similarity solution for wetted patch growth issued by capillary-driven and constant-flux point source on a horizontal plane, they reported a good agreement with measured moisture profiles and rates of spreading. Additionally, they developed an approximate analytical solution for growth of wetted region issued by point sources on an inclined sheet that was in agreement with the numerical calculations and experimental measurements.

The effect of the dynamic contact angle was explored by Chebbi (2007) and Hilpert (2009) on liquid infiltration into horizontal and inclined capillary tubes and by Hilpert and Ben-David (2009) for infiltration of liquid droplets into porous media. In a recent study on liquid infiltration into capillary tubes, Hilpert (2010) considered both constant and dynamic contact angles and neglected inertial forces and found analytical solutions for the interface position, velocity and acceleration as a function of time. Distinguishing among five infiltration scenarios for penetration into capillary tubes, the necessary criteria for each scenario were identified based on four governing dimensionless parameters.

Lately, with advancement of computational power, more attention has been paid to direct simulation of flow for different single- and multi-phase problems. Flow pattern and air entrapment during the filling of a vertical die cavity was studied numerically and experimentally by Hernandez-Ortega et al. (2010). They used the solution algorithm Volume-of-Fluid method to

solve the momentum and mass conservation equations (no surface tension effects due to size of the problem) and finding the flow front behavior for different Reynolds and Froude numbers.

The effect of the dynamic contact angle on the capillary filling of microfluidic channels was studied by Saha and Mitra (2009) using the VOF method. They evaluated different dynamic contact angle models for different microchannel geometries. They found that the dynamic contact angle models had very minor effect on the capillary flow within microchannels. Upon experimental validation, they concluded that application of static contact angle approach is adequate when using the VOF model in microfluidic applications.

Recently, the capillary-driven unidirectional flow of wetting liquids into porous medium was investigated numerically and experimentally by Markicevic et al. (2012). Study of multiphase capillary flows was also performed by Maggi and Alonso-Marroquin (2012) to present a model of the meniscus movement within uniform capillaries. They developed a mathematical model as a second-order nonlinear differential equation that describes the meniscus progression within a capillary under the action of gravity, interfacial tensions, viscous friction along the capillary, energy dissipation near the inlet, and retardation effect of the fluids in the reservoirs at the capillary ends.

Reviewing the above-mentioned papers, one can conclude that investigation of infiltration and void formation depends on micro-scale representation and modeling of flow and reliable tracking of the flow front which demands a multiphase analysis. Moreover, multiple driving forces (pressure gradient, gravity, interfacial forces) may contribute to infiltration, during which interfacial forces may play a significant role depending on the scale of the pores. Therefore, in the present work a numerical method was proposed based on the multiphase VOF and LS methods to solve the governing equations associated with each phase and to investigate the

interface behavior and formation of voids. Different effects such as gravity, pressure gradient, interfacial tensions, contact angle and viscous effects were considered and their importance was evaluated through the scale analysis of the nondimensional parameters. The numerical solution was conducted over a two-dimensional model in order to focus on the interface behavior and the effect of different parameters such as the pressure gradient and contact angle. Finally, the numerical results were compared to the experimental results exhibiting good agreement.

2.3 Details of Numerical Method

The infiltration process was considered as a multiphase problem involving liquid penetration into a porous structure, initially occupied by air. The capillary effects play an important role in flow through porous media. In order to have an in-depth understanding of infiltration and the contributing effects, it is necessary to consider all phases as well as the interfacial effects between them (Maggi and Alonso-Marroquin, 2012). Therefore, the volume-of-fluid (VOF) method (Hirt and Nichols, 1981) was selected to solve the governing equations of each phase including the interfacial effects. As mentioned by different references, the microscale flow behavior and interface (flow front) deformations are sources of void formation (Rohatgi et al., 1993; Patel et al., 1995; Binetruy et al. 1998 and Gourichon et al., 2006). Thus, a pore-level modeling and analysis was considered to study these effects. The influence of different conservative and non-conservative driving forces was mentioned in different references (role of injection pressure or pressure gradient by Peterson and Robertson, 1991; role of surface tension effects by Chan and Morgan, 1992; gravity and contact angle by Hilpert, 2010; and a combination of effects by Maggi and Alonso-Marroquin, 2012). Consequently, different driving forces resulting from gravity, pressure gradient, surface tension, contact angle were considered in

the proposed numerical method. However, an analysis of their role and importance is presented in the next section based on the nondimensional parameters governing this problem.

Since part of this research focuses on the behavior and evolution of liquid interface under the influence of different effects, interface tracking is of great importance. Several studies have been conducted regarding precision of interface tracking and its improvement in the VOF method (Lopez and Hernandez, 2008; Weymouth and Yue, 2010). In the VOF method, tracking of the interface is accomplished by solving an advection equation for the volume fraction function which is defined as a step function at the interface changing from one to zero. Due to using a discontinuous step function for interface tracking, the normal vector calculation could be inaccurate, causing difficulties in tracking and sharp-capturing of the interface. Thus, it makes it inaccurate to track the interface position and velocity especially at later time instants and in surface tension-dominant flows and over unstructured grids (Gerlach et al., 2006, Yang et al., 2006).

Two different strategies were mainly used to enhance interface tracking. One is coupling the VOF method with the LS method. In the LS method (Osher and Sethian, 1988), an advection equation is solved for a LS function, defined as a signed distance function from the interface and therefore the interface is where the LS function is zero. Therefore, this smooth continuous function has advantages in calculating the interface normal vector and tracking the interface position and velocity compared to the step function used in VOF method (Yang et al., 2006, Gerlach et al., 2006). However, the LS method is not conservative, tending to lose mass specially over coarse grids (Sussman and Puckett, 2000). Since the VOF is a conservative method, a coupled VOF and Level-Set (CVOFLS) method is widely used to include the advantages of both

methods and was shown to have benefits compared to each method (Sussman and Puckett, 2000, Yang et al., 2006).

The second strategy is improving the interface tracking schemes in the VOF method. This was done by a number of researchers using higher-order interface capturing schemes or via new techniques for evaluating the interface normal vector (Ubbink and Issa, 1999; Dendy et al., 2002; Pilliod and Puckett, 2004 and Wang et al., 2012). Consequently, in this dissertation, we used both the VOF method with high-order interface capturing scheme and a CVOFLS method to verify the obtained results of interface evolution (shape and position at different time instants). The criteria for selection of compressive interface capturing scheme for arbitrary meshes (CICSAM) as an interface tracking and capturing method in VOF method are the ability of this scheme to capture the interface subjected to strong deformations (as reported by Waclawczyk and Koronowicz, 2008), the ability to track the interface over the unstructured grids, and capturing the interface as a sharp boundary between phases. It was observed that the interface predicted using other capturing schemes is not very sharp and is widen in later time steps. The high-resolution interface capturing methods (HRIC) and compressive interface capturing scheme for arbitrary meshes (CICSAM) predict more features of the interface with better resolution compared to other schemes, such as geometric reconstruction. The ability of HRIC and CICSAM schemes in capturing the interface was studied by Waclawczyk and Koronowicz (2008) and the interface predictions were compared to experiments. They found that even though both interface capturing schemes are capable of predicting the main features of the flow, the CICSAM results contains less error (in the form of artificial time shift in pressure history) and are less affected by the diffusivity (which results a sharper interface between phases). Therefore, the CICSAM scheme was selected in this study as the interface capturing scheme in the VOF method.

In order to include the effect of interfacial forces during the infiltration process, the continuum surface force (CSF) model developed by Brackbill et al. (1992) was used. For simulation of the infiltration process and in order to focus on evolution of the interface, infiltration time and void formation, a simplified two-dimensional model was developed since there are complicating aspects in a real porous structure such as three-dimensional pore connectivity and pore size/shape distributions. There are also limitations in accuracy of interface capturing and tracking schemes in three dimensions, especially over unstructured grids, which can mask the physical behavior of phases during the infiltration. As to simplifications in development of the model, the pores were assumed uniform in size and shape and the surface roughness was neglected. The model retains the average geometric features of typical graphite foam (figure 2.1a) for impregnation of a pore through a pair of inlet and exit channels, as shown in figure 2.1b. The numerical results of the VOF method were verified against the CVOFLS method and eventually validated against the experimental results.

2.4 Governing Equations and Dimensionless Parameters

In order to illustrate the adopted VOF method, relevant dimensionless parameters were identified for the model problem. Pore diameter, d, was selected as the characteristic length and since surface tension plays a major role in infiltration, σ/μ was chosen as the characteristic velocity (which leads to the characteristic time of $\mu\, d/\sigma$) with σ and μ standing for surface tension and dynamic viscosity, respectively. This selection will lead to σ/d as the characteristic pressure and $\mu^2/\sigma d$ as the characteristic density. Equations 2.1 and 2.2 emerge as the dimensionless continuity and momentum equations for a Newtonian fluid:

$$\frac{\partial \bar{\rho}}{\partial \tau} + \left(\nabla \bullet \bar{\rho}\, \boldsymbol{u}\right) = 0\,, \qquad (2.1)$$

$$\frac{\partial \boldsymbol{u}}{\partial \tau}+(\boldsymbol{u}\bullet\nabla)\boldsymbol{u}=\frac{\mu^2\bar{g}\,d}{\sigma^2}-\frac{1}{\bar{\rho}}\nabla p+\frac{1}{\bar{\rho}}\nabla\bullet\left[\left(\nabla\boldsymbol{u}+(\nabla\boldsymbol{u})^T\right)+\frac{\lambda}{\mu}(\nabla\bullet\boldsymbol{u})I\right]+\frac{(d\,K_i)\nabla\alpha_i}{\frac{1}{2}(\bar{\rho}_i+\bar{\rho}_j)}\ , \tag{2.2}$$

where $\bar{g}$ and λ stand for gravitational acceleration and dilatational viscosity, respectively. Quantities $\bar{\rho}$, p and τ represent nondimensional density, pressure and time, respectively. Also, $\boldsymbol{u}$ represents the dimensionless velocity vector (defined as Ud/α with U as velocity), I is the identity tensor and superscript T stands for transpose operator. On the right side of the momentum equation, the last term represents the surface tension effects for a two-phase flow (based on the continuum surface force (CSF) model developed by Brackbill et al., 1992) in which i and j indices represent different phases, e.g. liquid and gas, respectively. Quantities α_i and K_i stand for the volume fraction and the interface curvature of phase i, respectively. The first term on the right hand side of equation (2.2) can be rearranged as:

$$\frac{\mu^2 gd}{\sigma^2}=\left(\frac{\mu U}{\sigma}\right)\left(\frac{\rho g d^2}{\sigma}\right)\left(\frac{\mu}{\rho U d}\right)=Ca.Bo.\frac{1}{Re_d}\ , \tag{2.3}$$

to highlight the various dimensionless parameters governing this problem. The capillary (Ca), Bond (Bo) and Reynolds (Re_d) numbers in this problem represent the ratios of the viscous to surface tension forces, gravitational to surface tension forces and inertial to viscous forces, respectively.

An estimation of the scales of the three dimensionless parameters is given in table 2.1 for two cases. The first case is the infiltration of cyclohexane into a porous structure with an average pore size of 400 microns at 20 °C, while the second case represents the infiltration of water into a porous medium with an average pore size of 800 microns at 50 °C. A typical velocity of the order of 10^{-2} m/s was assumed for both cases. Silva et al. (2009) was used for the thermophysical properties of cyclohexane.

The small Bond numbers indicate that gravitational effects are nearly two orders of magnitude weaker compared to the surface tension effects. The small values of the capillary number indicate that the surface tension effects are significant compared to viscous effects. Therefore, surface tension is expected to play the dominant role during the infiltration of liquids into micron-size pores.

Another important parameter in infiltration is the wetting properties of the liquid/surface which affect the interface shape and behavior. The contact angle represents the interfacial interaction among the liquid, gas and solid phases on the contact line. Considering the contact angle (θ), the capillary pressure is defined as $p_{cap} = 4\sigma\cos\theta / d$ and the modified dimensionless parameters will be defined as:

modified capillary number: $Ca^* = \mu.U /(\sigma.\cos\theta)$, (2.4)

dimensionless time: $\tau = \frac{t.\sigma.\cos\theta}{\mu.d}$, (2.5)

dimensionless pressure: $p = \frac{P}{P_{cap}} = \frac{P.d}{4\sigma\cos\theta}$, (2.6)

which leads to dimensionless pressure difference in the form of $\Delta p = \frac{(P_{in} - P_{out})d}{4\sigma\cos\theta}$, while t represents time, P stands for pressure and subscripts *cap*, *in* and *out* stand for capillary (pressure) and quantities at inlet and outlet of the pore, respectively.

2.5 Boundary Conditions and Computational Details

In pore-level analysis, details such as velocity profiles and mass flow rates are not known at the inlet and outlet of the pore, as shown in figure 2.1b. The only applicable condition for this case is a pressure boundary condition. Thus, an average of the hydrostatic pressure of the liquid

at the inlet port was selected as the boundary condition at the inlet. Pressure at the outlet port was selected as the ambient pressure, assuming that in a porous structure with interconnected pores, the gas can easily escape from the pore under negligible pressure drop during the infiltration. However, for infiltration of liquids into the porous structure, the liquid pressure at the inlet varies for different pores located at different heights. Furthermore, the pressure at the outlet may vary due to pressure drop in discharge of air from the pore. Both conditions cause a variation in pressure difference within the pore. Therefore, the variation of the pressure difference within the pore was also studied to elucidate the influence of pore pressure difference on the interface shape/position and the time duration of infiltration. In cases of having a small pressure at the inlet and/or pressure drop in air discharge from the outlet, the pressure difference within the pore becomes negligible. This case was also studied as the zero pressure gradient infiltration (wicking) during which interfacial forces (resulting from surface tension and contact angle) are the major driving forces of infiltration.

No-slip boundary condition was used on the walls of the pore for each phase. Considering the mean free path of the gas (air) at the ambient pressure and 25°C as 67 nm (Jennings, 1988), and the characteristic length of 400 μm (pore diameter), the resulting Knudsen number is $Kn=1.675\times10^{-4}$ which is smaller than 1, meaning that continuum mechanics and the no-slip boundary conditions on the walls of the pore are valid. It should be noted that the mean free path is smaller in liquids compared to gases. Therefore, the Knudsen number is even smaller for the liquid phase in comparison with the gas phase and no-slip boundary condition remains valid.

It should be mentioned that the no-slip boundary condition applied to each phase. However, the interface between liquid and gas progresses as a result of the driving forces (gravity, pressure difference and interfacial forces). Specifically, the surface tension forces are applied to the

interface as surface forces and the contact angle between the liquid and walls leads to forces acting on the contact points of the interface and the walls. Such forces are mainly responsible for the advancement of the interface and were modeled using the continuum surface force (CSF) method (Brackbill et al., 1992) and were included in the momentum equation. Furthermore, satisfying the continuity equation for each time step of the transient simulation ensures the conservation of mass in the VOF-based methods.

The governing equations for each phase were discretized using second order schemes and solved numerically using the finite volume approach. The computational fluid dynamics (CFD) package, Fluent 13.0 was used with a pressure-based formulation (Fluent 13.0, 2010). Both VOF method with higher order interface capturing scheme (compressive interface capturing scheme for arbitrary meshes, CICSAM, Ubbink and Issa, 1999) and CVOFLS method were used and the results were compared. For this purpose, a preliminary study was conducted on verification of the VOF method incorporated in Fluent package using a classical two-dimensional problem of dam-break, well-reported in the literature. The results of this study are presented in Appendix A and found to be in agreement with recent findings of dam-break problem. Upon verification of the method, the simulations were conducted and further verification (using CVOFLS method) and validation (using experimental method) were investigated for the obtained results.

The liquid phase was defined as an incompressible pure fluid and the infiltration process was isothermal (negligible Marangoni effects along the interface between two phases). For the gas phase, air was defined as a compressible fluid, even though the pressure changes are small. The graphite foam was considered as a solid porous structure and model dimensions were extracted from its structure. In this pore-level analysis, the walls of the pore were considered to be impermeable according to Klett et al. (2000, 2004) and based on our observation of graphite

foam walls obtained from SEM images of the foam samples (figure 2.1a). However, in general, depending on the application, the walls can be defined as permeable surfaces, for instance in case of infiltration of fibrous structures.

2.6 Grid Independence Study

Different unstructured grid systems were generated for the selected two-dimensional model and spatial and temporal grid independence was checked using a transient flow through the pore model. First, the spatial grid independence was studied for pressure-driven flow of cyclohexane through the pore using grids with 18000 to 250,000 quadrilateral cells, as shown in Figure 2.2a, and a final grid with 35000 cells was selected. Using the final grid, temporal grid independence was studied using different time step sizes under constant pressure difference. The result, presented in Figure 2.2b, indicates that time step sizes less than 5 μs are suitable for numerical simulations. A time step size of 1 μs was selected and used in future simulations. The grid is dense near the walls (compared to the interior of the pore, as shown in Figure 2.2c), thus providing higher accuracy in capturing the liquid interface contact point and tracking the interface. The simulation of infiltration is transient and continues in time until it reaches the steady-state condition of liquid mass exchange through inlet and outlet channels.

2.7 Results and Discussions

The effects of different parameters on the interface shape and behavior were studied numerically. Most importantly, the interface behavior is greatly affected by the contact angle which represents wettability of the porous structure by the liquid. In general, different interface shapes and phenomena were observed for wetting liquids compared to non-wetting liquids. The shape of the interface changes with the contact angle from concave in wetting liquids to convex

in non-wetting liquids. Therefore, results of infiltration of wetting liquids (corresponding to hydrophilic surfaces) and non-wetting liquids (corresponding to hydrophobic surfaces) are presented separately in sections 2.7.1 and 2.7.2, respectively. For each case, the effect of the inlet pressure variation on the interface shape, interface position, and infiltration time was evaluated. The role of pressure was finally generalized in each section for infiltration of the pore with wetting and non-wetting liquids.

2.7.1 Infiltration of Wetting Liquids

For wetting liquids (corresponding to hydrophilic walls, $\theta < 90°$), the interface generally has a concave shape and tends to wet the walls. However, a detailed consideration of the interface behavior and capillary forces is helpful in understanding the different phenomena that occur during infiltration such as wicking, interface pinning and fingering. These phenomena are responsible for the possibility of infiltration, formation of voids and void content within the pore.

A case of θ=30°, d=400 μm, $\overline{\rho} = 8\times10^3$, σ = 0.025 N.m^{-1} and dimensionless pressure difference of $\Delta p = (P_{in} - P_{out})d/(4\sigma\cos\theta) = 0.3$ (representing the infiltration of cyclohexane into graphite foam) was selected first to study the interface behavior and capillary pressure variations. For this case, the contours of the liquid volume fraction, exhibiting the evolution of the interface during the infiltration, are given at selected time instants in figure 2.3 and qualitative temporal variation of the capillary pressure as the main driving force of infiltration of wetting liquids is presented in figure 2.4. In a liquid with constant surface tension (due to isothermal infiltration) and contact angle, the capillary pressure is proportional to the interface curvature. Thus, figure 2.4 also presents the qualitative variations of the interface curvature.

The shape of the interface is concave and the meniscus shape and curvature remain unchanged at the early instants of infiltration when the liquid is entering through the inlet channel with a constant diameter and thus the capillary pressure remains constant (figure 2.3a). Liquid and gas phases are identified as red and blue colors, respectively. Since the inlet channel diameter is smaller than the pore diameter, the interface curvature and the resulting capillary pressure are higher when the meniscus is at the inlet channel (between points 1 and 2 in figure 2.4).

When the contact line touches the intersection of the inlet channel and the pore, progress of the interface stops temporarily, while a reduction of the interface curvature is observed. In fact, an interface temporary pinning occurs before the expansion from the inlet channel to the pore (figure 2.3b). A time-resolved evolution of the liquid interface shape and position is given in figure 2.5a for the liquid flow through the expansion at the intersection of the inlet channel to the pore. This reduction in curvature continues until the interface becomes flat (figure 2.3c). This curvature reduction reduces the capillary pressure to zero (point 2 to 3 in figure 2.4). After this point, the liquid starts expanding into the pore space while the interface is slightly convex (figure 2.3d). This will cause a slight negative capillary pressure (due to convex interface) and will continue for a brief period (from point 3 to 4 in figure 2.4) until the interface starts to progress on the walls again. Then, the shape of the interface starts changing again. In fact, the shape of the interface after this instant is two symmetric concave meniscuses connected together smoothly on the convexity at the middle of the interface, as shown in figure 2.6a. Interestingly, the velocity distribution for the interface at this instant exhibits the wetting behavior of the liquid due to the wall adhesion forces, as the interface velocity is higher near the walls compared to the bulk region of the pore. Accordingly, each meniscus at this time is moving mainly toward wetting the

walls of the pore, and not tending to fill the bulk of the pore, as figure 2.6b depicts the velocity distribution of the interface during this time period (for θ=30°).

Progression of the two meniscuses causes a reduction in the interface convexity and increases the capillary pressure again until the interface becomes nearly flat again as shown in figure 2.3e (from point 4 to 5 in figure 2.4). From this point on, the progress of the interface on the walls makes the interface concave again (figures 2.3f and g). This concavity is resulting from wall adhesion, i.e. the liquid tendency to wet the walls causing the interface to curve inward and have a meniscus shape. The capillary pressure increases and becomes positive again due to concave interface providing a driving force for the infiltration while the pore is being infiltrated. However, due to lower curvature of the interface within the pore (due to larger pore diameter than inlet channel), the resulting capillary pressure is smaller compared to the inlet channel (from point 5 to 6 in figure 2.4). As the interface progresses on the walls of the pore, it reaches the upper corner of the outlet channel intersection with the pore and is pinned there at one end, while the other end of the interface continues progression on the bottom wall (figure 2.3g, h and i). This progress in one end causes the interface curvature to increase due to the geometry of the pore. Thus, the capillary pressure increases as shown between points 6 and 7 in figure 2.4. This progress continues until the free end of the interface touches the other connecting corner of the outlet channel and the pore (figure 2.3k). At this time instant, the interface curvature and capillary pressure are maximum due to the geometry of the pore and the wetting nature of the liquid (point 7 in figure 2.4).

At this moment, another interface temporary pinning (and reduction of interface curvature) occurs while the liquid is experiencing a contraction flowing from the pore into the outlet channel. Temporal evolution of the interface during this temporary pinning is presented in figure

2.5b. As the interface curvature reduces, the liquid starts filling the outlet channel slowly (figure 2.3l) and the interface curvature and capillary pressure return to same levels as the inlet channel since the channels sizes are the same (between points 7 and 8 in figure 2.4). Upon filling the outlet channel, the infiltration process is complete.

As a general behavior, during the infiltration, the liquid's tendency for wetting the walls makes the walls wet before occupying the bulk of the pore. Consequently, the meniscus surrounds the air in the bulk of the pore (figure 2.3h, i and j) and pushes the air outward through the outlet channel. Therefore, the pore will be entirely infiltrated with the liquid and there is no void formation in this case. It should be noticed that among the driving forces in this problem, the capillary pressure plays the major role for wetting liquids. In addition, it dynamically changes with the interface curvature. The interface curvature changes from concave to convex at some moments although the liquid is wetting and the convex interface produces negative capillary pressure resisting infiltration (from point 3 to 5 in figure 2.4, i.e. expansion from the inlet channel to the pore). Similar phenomenon was reported by Broesch and Frechette (2012) based on their experimental observations on pinning and interface curvature changing from concave to convex for liquid bridges in slit pore geometries with variation of the aspect-ratio. Also, Sui and Spelt (2011) studied the flow of a viscous, wetting liquid in a tube including the inertial, viscous and capillary effects. They reported a change in the interfacial curvature from concave to convex at the center of the tube, with increasing of the Reynolds number. The infiltration process is continued even though the capillary pressure is negative since in addition to the capillary forces, the liquid is also under the influence of the pressure difference and dynamic pressure. As a result, the total pressure can be considered as the net driving force of the infiltration process. Since the velocities are relatively small (of order of 10^{-1} to 10^{-2} $m.s^{-1}$ for this problem), the dynamic

pressure has a minor effect. Thus, the variation of capillary pressure and pressure difference affect the infiltration behavior markedly. Therefore, these effects can be summarized using the dimensionless pressure difference (pressure difference divided by capillary pressure) which are presented in sections 2.7.1.1 and 2.7.1.2.

Furthermore, temporary pinning of the interface was observed in two situations during the infiltration of the pore. The first case is when the liquid is experiencing an expansion entering the pore through the inlet channel. The second case is when the liquid contracts while flowing from the pore into the outlet channel. Temporary pinning of the interface, as shown for the expansion and contraction cases in figures 2.5a and b, respectively, was also observed in wicking flow through microchannels by Mehrabian et al. (2011) and on micropillar edges by Berthier et al. (2009).

2.7.1.1 Infiltration in the Absence of Pressure Gradient (Wicking Flow)

For wetting liquids, infiltration may occur under zero pressure gradient and be governed by capillary forces, known as wicking flow. In wetting liquids, the capillary forces favor infiltration in combination with the pressure difference and dynamic pressure, as it was shown in figure 2.3 for a case of a positive pressure difference. Depending on the balance of the total pressure components, the infiltration may occur even in the absence of a pressure gradient in the pore. Under such condition, the motion of the liquid is driven by the capillary pressure generated by interface curvature (concave) known as wicking.

The zero pressure gradient infiltration was investigated by applying the same pressure at the inlet and outlet channels. The results are presented in figure 2.7 in the form of the liquid fraction contours at selected time instants for θ=30° with cyclohexane as the liquid. In the absence of the pressure gradient, infiltration occurs due to the capillary pressure. However, the

capillary pressure (as qualitatively discussed by figure 2.4) can be negative when the liquid is expanding into the pore through the inlet port (between points 3 and 5 in figure 2.4) and the interface is convex. During that period, infiltration continues if the dynamic pressure can overcome the negative capillary pressure. In fact, the total pressure as the net driving force of infiltration can be defined for this case as:

$$P_{total} = P_{cap} + P_{dyn} = K.\sigma.\cos\theta + \frac{1}{2}\rho U^2, \qquad (2.7)$$

where K stands for the interface curvature, U represents the interface velocity and infiltration takes place when $P_{total} > 0$. The subscripts *dyn* and *total* represent the dynamic and total pressure.

In order to consider the effect of the contact angle on wicking through the pore, different numerical analyses were performed using the same liquid properties and different contact angles. It was concluded that increasing the contact angle increases the curvature (as well as negative capillary pressure) during the period when the liquid is expanding into the pore that is accompanied with a decrease of velocity; thus the total pressure decreases with increasing the contact angle. Therefore, wicking through the pore occurs only for a narrow range of contact angles. For the pore geometry considered in this problem, wicking happens when the contact angle is less than 38°. For higher values of the contact angle, when the liquid enters the pore, the curvature increases while the interface is convex. This will produce a negative capillary pressure, acting against infiltration (figure 2.8b, c for the contact angle of θ=45°). As the liquid is entering the pore and convexity of the interface increases, the negative capillary pressure decreases until its value becomes equal to the dynamic pressure. Due to this balance, the total pressure vanishes and the progress of the interface is terminated (figure 2.8d) causing the velocity components and accordingly the dynamic pressure diminish to zero. With the dynamic pressure nonexistent,

negative capillary forces become dominant causing the interface to retreat (figure 2.8e, f). The interface then becomes unstable and recedes. Upon retreating into the inlet channel, the interface becomes slightly concave again and produces positive capillary pressure (figure 2.8g). This will cause a slight oscillation of the interface until it finally reaches a new equilibrium flat state and is pinned there permanently. Upon permanent pinning, both terms of the capillary and dynamic pressures will vanish to zero due to zero interface curvature (for flat interface) and zero interface velocity (figure 2.8h, i).

2.7.1.2 Effect of the Pore Pressure Difference (Wetting Liquids)

Variation of the inlet pressure (e.g. due to variation of liquid pressure with height) affects the pressure difference within the pore (ΔP). With negligible gravitational effects, the combination of the pressure difference, capillary pressure and dynamic pressure acts as the driving force of infiltration. As the ratio of pressure difference to capillary pressure, the dimensionless pressure will summarize the effects of the pressure difference and capillary pressure during infiltration. Variation of pore pressure difference not only influences the interface shape and position, but also affects the time duration of the infiltration process. As one can contrast the infiltration time instants between figures 2.3 and 2.7, reduction of the pressure difference increases the infiltration time. The interface shape and position within the pore are presented at t=500 μs in figure 2.9 under various inlet pressure conditions for the contact angle of θ=30°. As observed from figure 2.9, upon increasing the inlet pressure (i.e. pressure difference), the interface shape and position are highly affected and the amount of infiltrated liquid during the 500 μs rises. In effect, the pore infiltration time decreases with increasing the pressure difference.

In order to establish the relation between the pressure difference and pore infiltration time, several numerical simulations were performed for different values of the contact angle and pressure difference and the results are presented in figure 2.10a. For a constant value of the contact angle, the infiltration time decreases with increasing pore pressure difference. The infiltration time was defined as the time instant when the liquid interface passes through the outlet boundary. For high values of the pressure difference, same behavior is observed for different values of the contact angle. This is because for high values of pressure difference, it dominates other driving forces and overshadows their effects.

Using nondimensional time and pressure relations, as defined by equations 2.4–2.6, the results of various analyses with different contact angles, pressure differences and pore diameters collapse into a single curve representing the general infiltration behavior (time vs. pressure) as shown in figure 2.10b. When the dimensionless pressure difference approaches zero, the infiltration time approaches infinity asymptotically. The physical interpretation of this behavior is permanent pinning of the interface for such cases. This behavior can be explained by considering the total pressure of the liquid:

$$P_{total} = \Delta P + P_{cap} + P_{dyn} = \Delta P + K.\sigma.\cos\theta + \frac{1}{2}\rho U^2 . \qquad (2.8)$$

The capillary and dynamic pressures depend on the interface curvature and velocity, respectively. To maintain infiltration, the total pressure should remain positive as the net driving force. Since the dynamic pressure is always positive and capillary forces of wetting liquids help infiltration, the total pressure usually remains positive. The only situation during which the capillary pressure becomes negative (acting against infiltration) is when the liquid is entering the pore through the inlet channel and the interface is convex as discussed in figure 2.4. For wetting liquids with small contact angles, the amount of this negative capillary pressure is not

considerable due to the smooth interface curvature at that moment. Therefore, the total pressure during that period remains positive due to the positive dynamic pressure term. Even for small negative values of the pressure difference, the total pressure can remain positive and this is the reason infiltration can occur under such conditions for wetting liquids as shown in figures 2.10a and b.

Further reduction of negative pressure difference (due to a decrease in pressure difference or an increase in curvature of the interface) will drive the total pressure to zero and negative values. When the total pressure reaches zero, the interface stops progressing and the velocity components go to zero as well as the dynamic pressure. Losing positive dynamic pressure changes the force balance on the interface and it retreats until it goes back to an equilibrium state between the pressure difference and capillary pressure, ensued by permanent pinning of the interface. Interface pinning was studied by Koplik et al. (1985), Narayan and Fisher (1993), Delker and Pengra (1996) and observed in spontaneous imbibition by Dube et al. (2001). The pressure balance after permanent pinning of the interface can be described as:

$$P_{total} = \Delta P + P_{cap} = \Delta P + K.\sigma.\cos\theta = 0\,, \tag{2.9}$$

which leads to:

$$K = -\frac{\Delta P}{\sigma \cos\theta}\,, \tag{2.10}$$

(ΔP being negative) as the interface curvature for the permanent pinning. Upon decreasing the pressure difference, the permanent pinning of the interface occurs at higher interface curvatures, i.e. closer to the inlet channel. When the negative pressure difference is equal to the inlet channel capillary pressure, the total pressure is zero at the inlet channel and therefore, interface permanent pinning occurs at the inlet channel without any liquid entering the pore. From this

point forward, further reduction of negative pressure difference will cause the total pressure to be negative at the inlet channel. Under this condition, infiltration cannot occur since the negative pressure difference is strong enough to overcome the inlet channel capillary pressure and drive the liquid meniscus backward. Therefore, according to equation 2.9, the criterion for infiltration can be identified as

$$\Delta P > \left(-K.\sigma.\cos\theta\right)_{in} = -\frac{4\sigma.\cos\theta}{d_{in}} = -P_{cap,in}\,. \tag{2.11}$$

This criterion is presented schematically in figure 2.10c. Since the interface curvature and velocity magnitude are changing with time and position, the total pressure changes temporally and spatially during the evolution of the liquid front. Thus, at any moment/location that the total pressure goes to zero, the interface progress will be impeded and permanent pinning will occur. In other words, the total pressure may dynamically reduce from a positive amount at the inlet channel (with maximum capillary pressure) to zero due to change of the interface shape and curvature (from concave to convex) which can lead to interface permanent pinning. Permanent pinning of the interface within the pore is shown in figure 2.11 for a pressure difference of -20 Pa and θ=30° is shown in figure 2.11, whereas the flow arrest, retreat and permanent pinning within the inlet channel is given in figure 2.12 for a pressure difference of –40 Pa and θ=30°.

2.7.2 Infiltration of Non-Wetting Liquids

For non-wetting liquids (corresponding to hydrophobic surfaces) unlike wetting liquids, the contact angle is greater than 90° and the interface generally has a convex shape which leads to negative capillary pressure, acting against infiltration. Since gravitational effects are negligible and dynamic pressure is small, a positive pressure difference is always necessary to overcome negative capillary pressure in order to promote infiltration.

As a general behavior for non-wetting liquids, the interface shape is convex and is not tending to wet the walls of the pore. Accordingly, the interface progresses mainly toward filling the bulk of the pore during infiltration, especially for relatively high pressure differences which leads to higher values of interface velocity. When the interface progresses more toward the bulk of the pore, there is a possibility of air entrapment and void formation in the pore. The roles of the pressure difference, capillary pressure and dynamic pressure are discussed in section 2.7.2.1. The air entrapment and void formation within the pore is presented in section 2.7.2.2.

2.7.2.1 Effect of Pore Pressure Difference (Non-Wetting Liquids)

Since the interface is convex and the capillary pressure is negative for non-wetting liquids, infiltration will not occur in the absence of pressure gradient and therefore there is no wicking flow. Infiltration occurs when $P_{total} = \Delta P + P_{cap} + P_{dyn} > 0$ which implies that a positive pressure difference greater than the negative capillary pressure needs to be established. Furthermore, small capillary and Bond numbers (of the order of 10^{-4} and 10^{-2}, respectively, according to table 2.1) suggest that viscous and gravitational forces are not significant compared to interfacial forces. Thus, the pressure drop and interfacial forces play the main roles during the pore infiltration.

For a wall contact angle of θ=120° and dimensionless pressure difference of Δp=10, the instantaneous contours of the liquid volume fraction are displayed in figure 2.13. As observed from figure 2.13, the interface remains convex and no interface pinning was observed. The interface is advancing toward the interior of the pore (and not wetting the inner walls of the pore) due to the pressure difference and its convexity (θ > 90°) which leads to a fingering phenomenon at pore level (as shown in figure 2.13b, c and d). In this case, advancement of the interface

continues until the interface impinges the wall of the pore opposite to the inlet channel (figure 2.13e). Then, the interface advances in other directions, mainly toward the outlet (figure 2.13e and f). Due to the shape of the interface and its impingement on the wall of the pore, a portion of air is trapped within the pore in the form of an air bubble and it persists as a stable void (blue color areas in figure 2.13g, h and i).

Pore pressure difference influences the interface curvature (shape) and velocity as well as the void content in the pore. The effect of the pressure difference on the shape of the interface and its position is shown in figure 2.14 for a contact angle of 120° after 0.5 *ms*. It is concluded that a higher value of the pressure difference will increase the interface velocity and decrease the infiltration time. Moreover, when the interface velocity is high, it advances through the pore quickly (fingering-like phenomena) and its impingement on the wall leads to the entrapment of a larger portion of air within the pore.

The pore infiltration process was investigated for different values of the pressure difference and contact angles (greater than 90°) and the nondimensional infiltration time are presented versus the dimensionless pressure along with general infiltration criterion for non-wetting liquids in figure 2.15. As observed, increasing the pressure difference lowers the infiltration time, whereas decreasing the pressure difference reduces the void content of the pore. In fact, reducing the pressure difference causes the interface to progress on the walls and in the interior of the pore with nearly the same pace. Therefore, less air is entrapped under moderate values of the pressure difference.

Contours of the liquid fraction during the pore infiltration for $\theta > 90°$ and a pressure difference of $|\Delta p|=5$ (in contrast with pressure difference of $|\Delta p|=10$ in figure 2.13) are given in Figure 2.16. One should notice that the nondimensional pressure difference and infiltration time

as defined by equations 2.5 and 2.6 are negative due to $\theta > 90°$. Thus, the magnitude of the pressure difference was used in the discussion. As observed from figure 2.16, for moderate values of the pressure difference, the size and position of the void is different than the cases of high pressure difference, shown in figure 2.13.

When the value of the pressure difference decreases further, the pore infiltration time approaches infinity which corresponds to interface permanent pinning. It should be noticed that permanent pinning for non-wetting liquids always occurs under positive pressure differences since the capillary pressure is always negative. Therefore, the total pressure goes to zero under positive values of the pressure difference and the permanent pinning of the interface occurs as equilibrium between the pressure difference and capillary pressure. A case of permanent pinning of the interface for a contact angle of 120° and a pressure difference of $|\Delta p|=2$ is shown in figure 2.17. Further reduction of the pressure difference causes a negative total pressure due to negative capillary pressure and moves the interface backward in the inlet channel, and no infiltration will be realized. Similar to figure 2.10b, the general criterion for infiltration is depicted schematically in figure 2.15b. It should be noticed that the total pressure consists of three components of pressure difference that is constant, the dynamic pressure that varies with velocity and the capillary pressure that changes with the interface curvature.

2.7.2.2 Formation of Voids (Non-Wetting Liquids)

As observed in figures 2.14 through 2.17, for non-wetting liquids, the variation of pressure does not influence the convex shape of the interface. However, it affects the void content of the pore through influencing the interface progress. Void formation mainly depends on the fingering phenomenon in the pore. When fingering occurs, the void content is noticeably greater due to the advancement of the convex interface in the interior of the pore and its impingement on the wall

of the pore. Void content in this case depends on the interface velocity and interfacial effects (surface tension and contact angle). Since the interface velocity is variable at different points and time instants, a characteristic velocity should be defined to characterize the interface velocity during infiltration. This characteristic velocity can be defined as the mean flow front velocity through the porous structure, which is identified as the liquid penetration distance, L, as shown in figure 2.18 divided by the infiltration time.

Using this characteristic velocity, the void content can be related to the modified capillary number, Ca^*, since the capillary number takes into account the characteristic velocity, viscosity, surface tension and contact angle. Therefore, void content was correlated with the modified capillary number for different cases of the contact angle and pore pressure gradient and the results are summarized in figure 2.19. One should notice that the modified capillary number for non-wetting liquids is negative for the contact angles being greater than 90°.

As discussed in section 2.7.2.1, the void content within the pore rises with increasing the pressure difference due to pore-level fingering phenomenon. Increasing the pressure difference within the pore increases the interface convexity and boosts its velocity while it is progressing quickly through the pore like a fluid column or finger. This expedites the liquid impingement on the wall of the pore and leads to entrapment of a larger portion of air at the bottom part of the pore, e.g. higher void content in the porous structure.

As a result, for higher values of the modified capillary number, the occurrence of the fingering phenomenon is more likely which leads to higher void contents. Below the modified capillary number of nearly –0.25, fingering was not observed in the pore and there is no void formation. Above that value, the void content of the pore increases noticeably due to the

fingering phenomenon. Same void formation behavior was reported by Rohatgi et al. (1993), Kang et al. (2000), and Park et al. (2011).

2.8 Numerical Verification of the Results

To obtain the numerical results and investigate the interface behavior, the VOF method was used with higher-order interface capturing schemes, mainly CICSAM (compressive interface capturing scheme for arbitrary meshes). Since tracking and capturing the interface is of great importance, the numerical results were verified using the CVOFLS method as another conservative method in modeling immiscible multiphase flows. As shown in figure 2.20, comparison of the interface evolution (shape and position of liquid interface at different time instants for wetting and non-wetting liquids) predicted using two numerical methods (the VOF method with higher-order capturing scheme versus the CVOFLS method) reveals a good agreement in the interface shape/position during infiltration.

Furthermore, the values of the pore infiltration time and void content predicted by the VOF and CVOFLS methods are compared in table 2.2. As one can observe from Figure 2.20, the interface shapes at different time instances have slight differences. However, these slight differences do not affect the general characteristics of the pore infiltration as summarized in table 2.2. In effect, there is relatively good agreement between the results of the two methods with the CVOFLS technique consistently predicting a slower rate of infiltration. Further experimental validation is presented in section 2.9.

2.9 Experimental Validation of the Results

For validation purposes, the present numerical predictions were compared to the experimental and theoretical results of horizontal wicking flow through a horizontal network of

pores in series (i.e. no pressure gradient and no gravitational effects). Firstly, numerical results of liquid penetration length into networks of pores in series with different number of pores were obtained. A typical two-dimensional model of 4 pores in series and the penetration length, *L*, are shown in figure 2.18. The penetration length versus time data was extracted from the numerical simulations and is shown in figure 2.21. A power-law curve fit to these data reveals that the penetration length is proportional to $t^{0.555}$ which is qualitatively in accordance with the Washburn's equation (Washburn, 1921).

Considering cylindrical capillaries, Washburn (1921) found that the instantaneous liquid penetration length, *L*, into a horizontal capillary is proportional to the square root of the elapsed time, *t*, and derived the following equation,

$$L^2 = \left(\frac{\sigma}{\mu} \frac{\cos\theta}{2} \right) r\, t\,, \tag{2.12}$$

in which *r* stands for the radius of the capillary.

The deviation of predictions of the present model from the Washburn's equation originate from the fact that in this study, the liquid is penetrating on the periphery of cylindrical capillaries and not along them. Thus, the instantaneous radius of the capillary is not constant. Consequently, we proposed a modified Washburn equation for the penetration length in the form of

$$L^2 = C_w \left(\frac{\sigma}{\mu} \frac{\cos\theta}{2} \right) t \quad , \tag{2.13}$$

in which C_w has dimensions of length, standing for correction of the variable radius of the capillaries for the wicking flow across the pores and along the inter-connecting channels between the pores. The average value of C_w was found to be 7.66×10^{-6} *m*, based on the obtained numerical results of wicking flow through a network of pores in series (i.e. penetration length versus time).

The comparison of the modified Washburn equation (equation 2.13) with the numerical predictions of the liquid penetration length versus the elapsed time is also given in figure 2.21.

Furthermore, the liquid penetration length as a function of the elapsed time was measured experimentally for the case of horizontal wicking flow through samples of graphite foam. The average pore size of the graphite foam is 400 μm and its porosity is 75% (PocoFoam®, Poco Graphite Inc., 2012). Based on these specifications, the number of pores in series was estimated for different samples of graphite foam and horizontal wicking flow through the foam was investigated experimentally. An experimental setup (shown schematically in figure 2.22a) was arranged for unidirectional flow of cyclohexane (as the liquid with a contact angle of about 30° with graphite) into the foam samples. Liquid flows from a reservoir full of cyclohexane that is maintained at a constant level. The liquid discharges to an empty reservoir at the opposite side of the sample, thus establishing a unidirectional horizontal wicking through the sample. The graphite samples have a thickness of 10 mm in order to minimize the pressure difference in the vertical direction within the penetrating liquid. The reservoirs and the graphite sample are exposed to the ambient from the top side (as observed by the camera, figure 2.22a). Thus, liquid penetration is driven by interfacial forces, whereas gravity and pressure gradient play negligible roles during infiltration. Experimental measurements of the liquid penetration time and length were performed using video recording of wicking flow through the porous structure and frame analysis of the recorded videos for various experiments over three different samples of graphite foam. Selected picture frames of liquid penetration into one of graphite foam samples are presented in figure 2.22b.

Finally, liquid penetration length and time measurements during the horizontal wicking flow were compared to the numerical and theoretical (modified Washburn equation) models as

presented in figure 2.23. Generally, good agreement was found among the numerical, experimental and theoretical results. For each experimental measurement, the penetrating liquid interface is not flat. Thus, variations in each of the experimental measurements are noted due to the randomness of the pore diameter, pore density and pore connections within the graphite foam samples. In addition, the graphite foam is not homogeneous and factors such as pore size distribution, impurities and dead-end pores in the structure of graphite foam (with 96% open porosity) are the main reasons why the liquid front is not flat. These variations of flow penetration lengths at each time instant, resulting from the curved shape of penetrating liquid interface, are presented in figure 2.23. Furthermore, the experiment was repeated four times to ensure repeatability and obtain the uncertainties associated with liquid penetration length measurements, as shown in figure 2.24 (Moeini Sedeh and Khodadadi, 2013D). In conclusion, the general behavior of penetration length versus time is in agreement with the numerical model and the modified Washburn equation.

2.10 Conclusions

Infiltration of wetting and non-wetting liquids was investigated at the pore level using the VOF method. The time-dependent evolution of the interface (liquid front) was investigated numerically for both wetting and non-wetting liquids. The effect of different driving forces and interfacial effects (especially wettability) on infiltration process and liquid interface behavior was studied.

The concave shape of the interface and its time-dependent variation during infiltration of wetting liquids was investigated as well as the temporary and permanent pinning of the interface. The infiltration criterion for wetting liquids was studied and the global infiltration time versus pressure was obtained using dimensionless quantities. Infiltration under zero pressure gradient

(and no gravity, i.e. horizontal liquid penetration into porous structure), also known as wicking flow was studied for wetting liquids. No void formation was observed for wetting liquids, due to the high tendency of the liquid to wet the walls of the pore ($\theta < 90°$). However, it should be noted that void formation might occur due to vaporization during infiltration (not considered in this dissertation).

Likewise, the interface behavior was studied for non-wetting liquids. The proposed numerical method was capable of tracking the interface and predicting the formation of the void within the pore that exhibited a fingering-like phenomenon in the pore. The volume and distribution (shape) of the voids (air pockets) in the pore was predicted for non-wetting liquids and correlated to the modified capillary number.

The numerical results were also verified against those obtained from the CVOFLS method, known to have higher accuracy in capturing the interface. The predicted time-evolving liquid interfaces based on these two methods and pore infiltration time were compared and found to be in good agreement. Moreover, the numerical results of horizontal wicking flow through the network of pores in series (no pressure gradient and no gravity) were validated against the experimental results of unidirectional horizontal wicking of cyclohexane into graphite foam samples and theoretical results based on the Washburn equation. Good agreement was found between the numerical, experimental and theoretical results.

Table 2.1 Comparison of the dimensionless parameters for two infiltration cases

Case	Properties	Ca †	Bo	Re_d †
Cyclohexane infiltration, $d=400\ \mu m$ $T=20\ °C$	$\rho= 778.7\ kg.m^{-3}$ $\sigma= 0.025\ N.m^{-1}$ $\mu = 9.8467\times10^{-4}$ $kg.m^{-1}.s^{-1}$	3.94×10^{-4}	4.89×10^{-2}	3.16
Water infiltration, $d=800\ \mu m$ $T=50\ °C$	$\rho= 987.7\ kg.m^{-3}$ $\sigma= 0.072\ N.m^{-1}$ $\mu = 5.3185\times10^{-4}$ $kg.m^{-1}.s^{-1}$	7.39×10^{-5}	2.15×10^{-2}	7.43

† Based on a typical velocity of $0.01\ m.s^{-1}$ for liquid flow during the infiltration process and $9.81\ m.s^{-2}$ for gravitational acceleration.

Table 2.2 Comparison of pore infiltration time predicted by the VOF and CVOFLS methods

Pore diameter, d, μm	Contact angle, θ, degrees	Pore pressure difference, ΔP, Pa	Pore infiltration time, VOF method, μs	Pore infiltration time, CVOFLS method, μs	Deviation, %
400	30	0	3990	4200	5.26
400	30	100	2485	2550	2.62
400	60	200	2300	2410	4.78
400	120	400	2500	2640	5.6

(a)

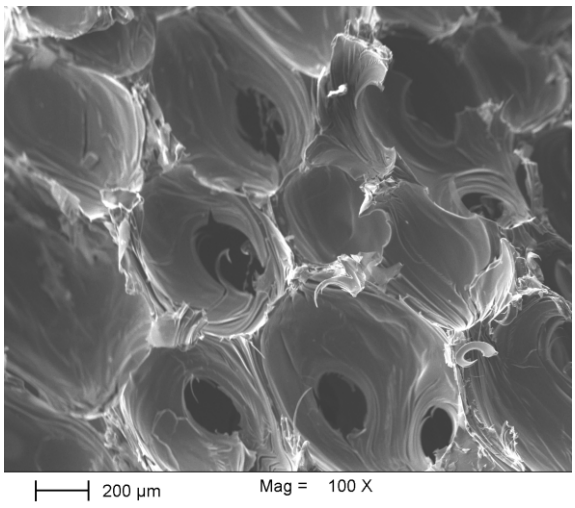

(b)

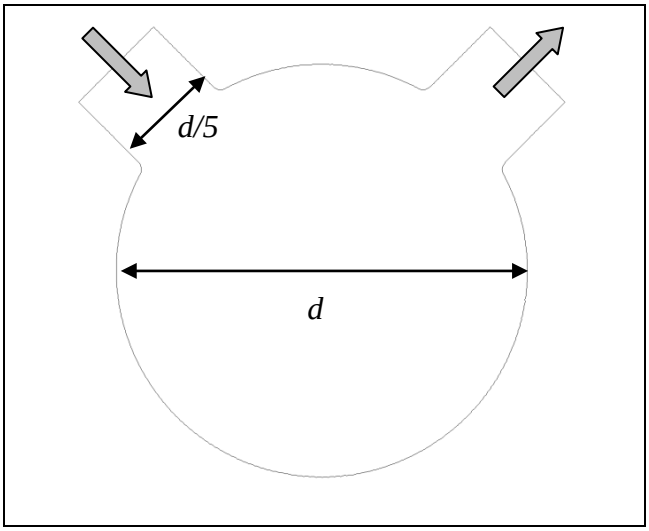

Figure 2.1 (a) Scanning electron microscope (SEM) image of graphite foam (PocoFoam®) with interconnecting pores and average pore size of 400 µm and 75% porosity, (b) Simplified two-dimensional model of the pore based on the geometric features of the porous structure.

(a)

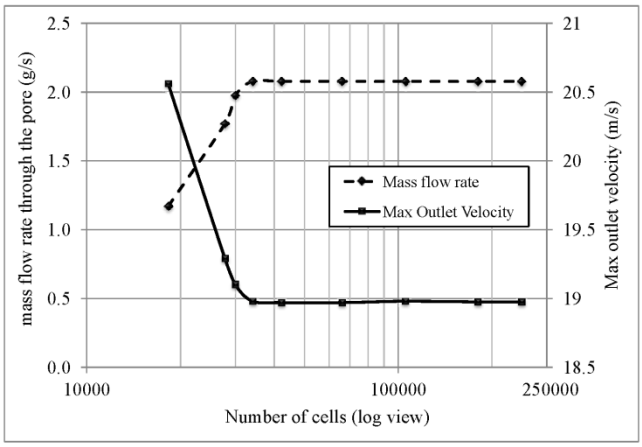

(b)

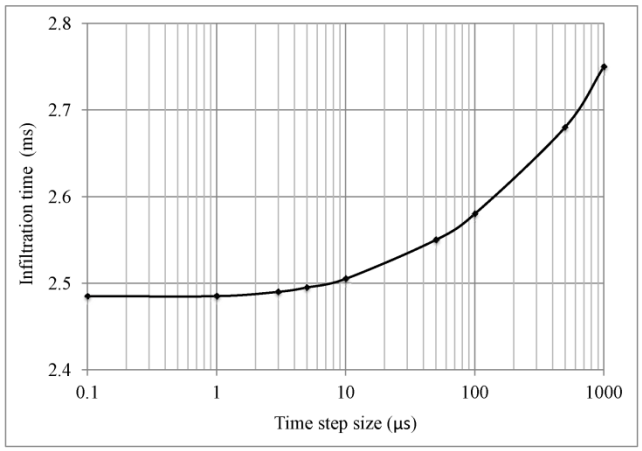

(c)

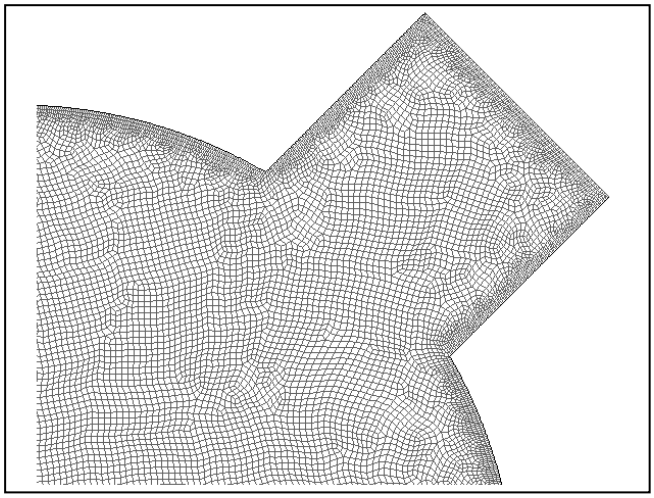

Figure 2.2 (a) Spatial grid independence study, (b) temporal grid independence study, and (c) detailed view of the grid

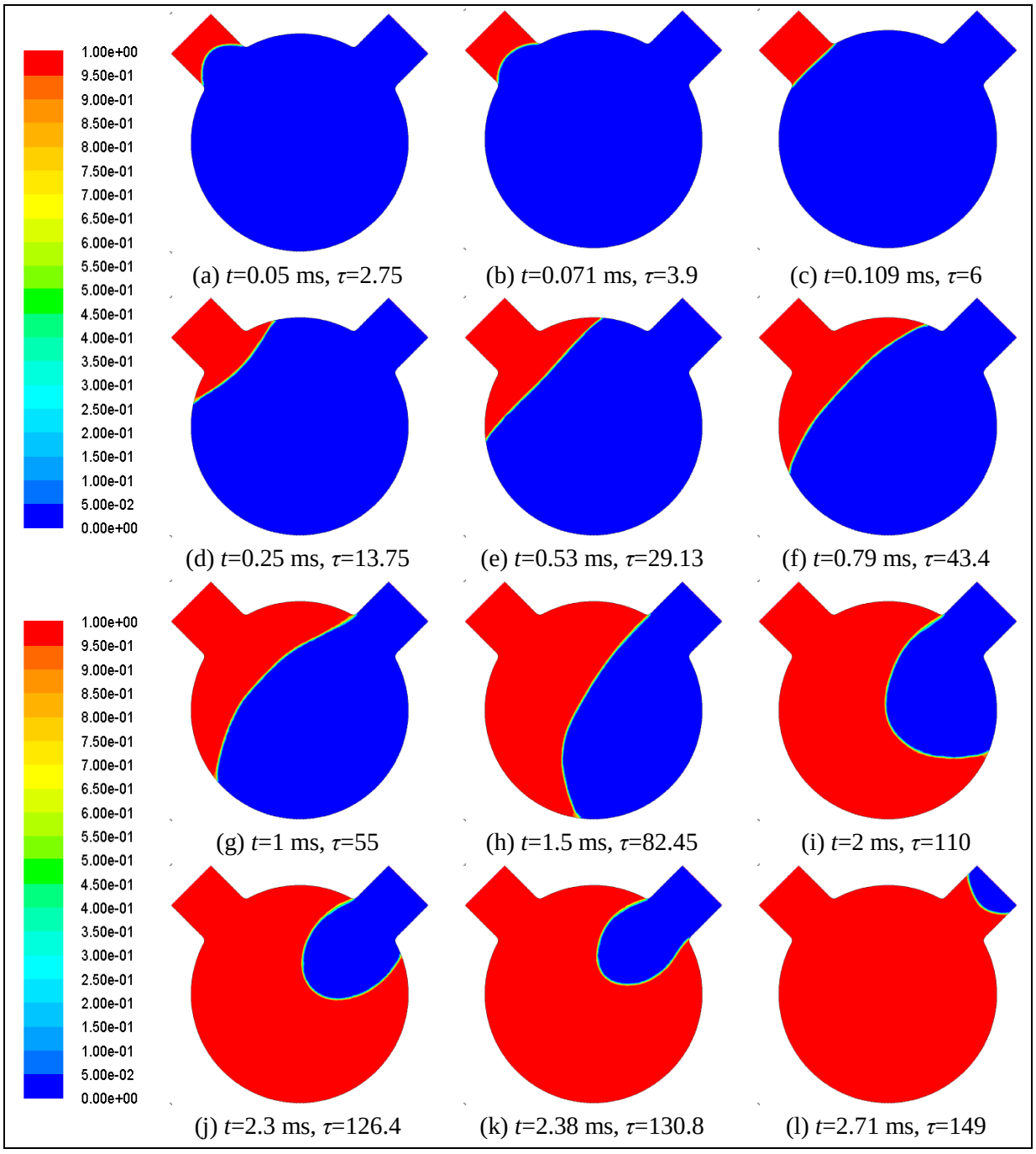

Figure 2.3 Evolving liquid fraction distribution (flow front) during the infiltration of cyclohexane into a graphite pore for the wall contact angle of 30° and pressure difference of 65 Pa ($\Delta p = 0.3$) at different time instants (τ represents dimensionless time).

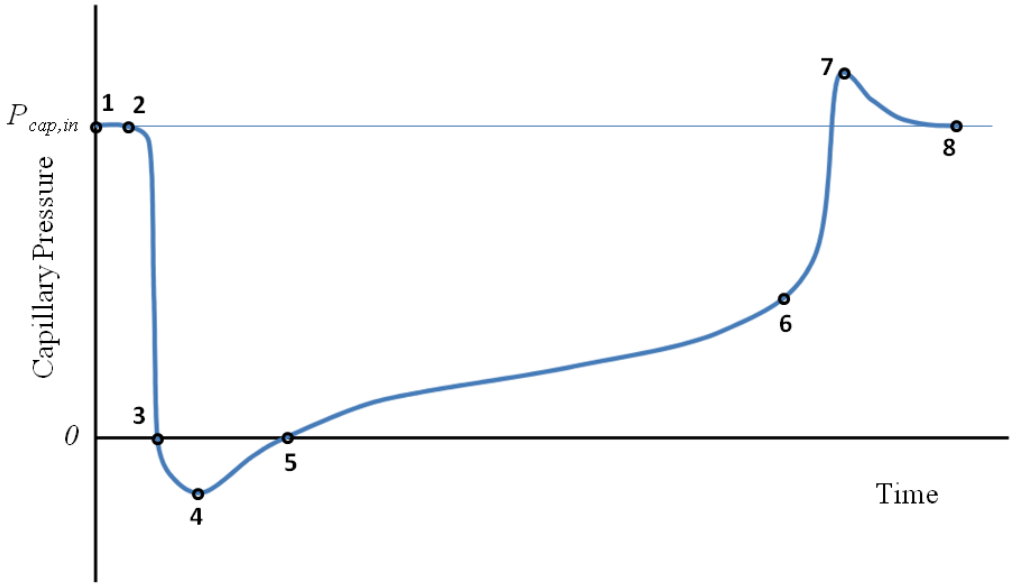

Figure 2.4 Qualitative variation of the capillary pressure with time during pore infiltration. Since for a liquid with constant surface tension and contact angle, the capillary pressure is proportional to the interface curvature, the qualitative variation of interface curvature is the same. $P_{cap,in}$ represents the capillary pressure in the inlet channel corresponding to interface curvature of $4/d_{in}$.

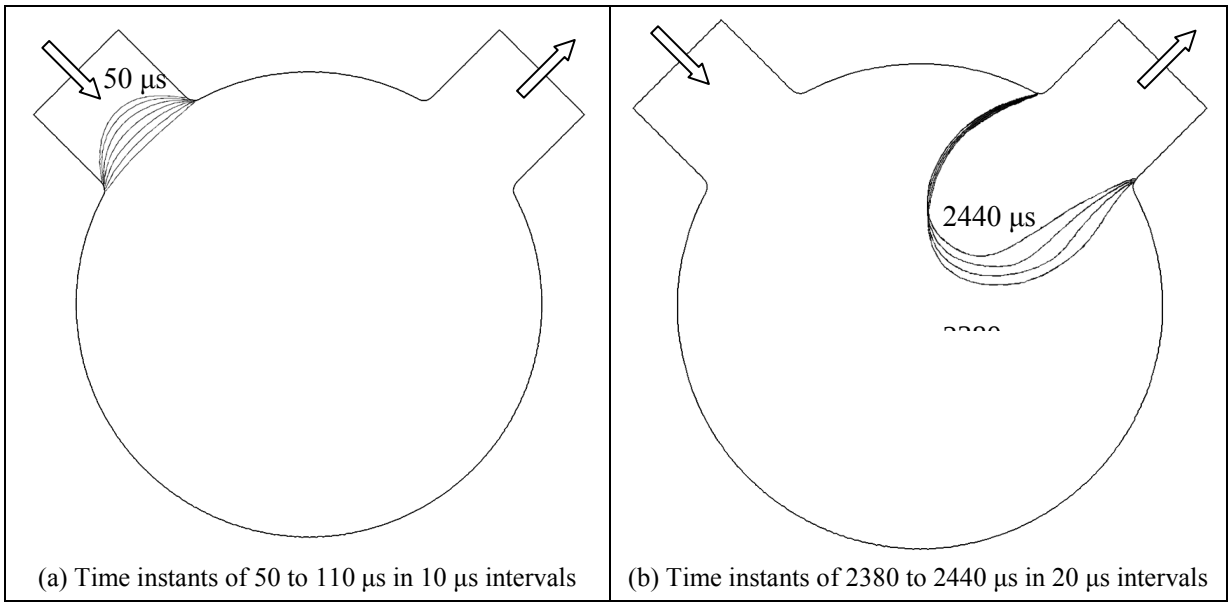

Figure 2.5 Interface positions during the interface temporary pinning for: (a) the liquid expansion flowing from the inlet channel to the pore and (b) the liquid contraction at the intersection of outlet channel to the pore.

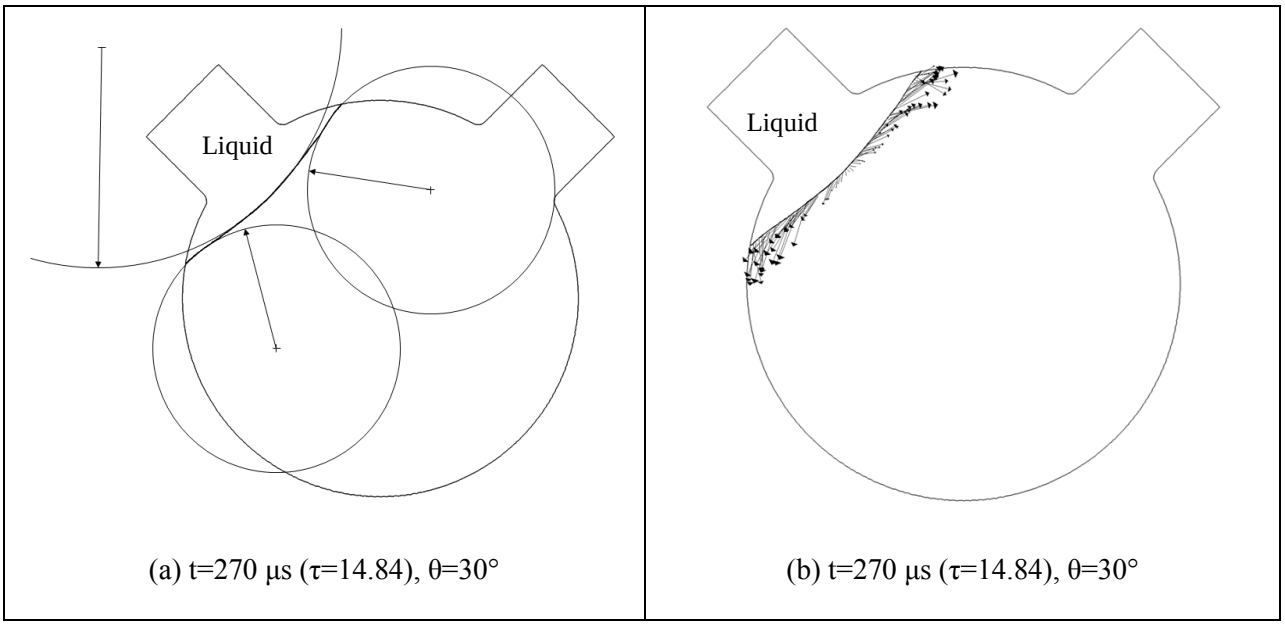

(a) t=270 μs (τ=14.84), θ=30°

(b) t=270 μs (τ=14.84), θ=30°

Figure 2.6 (a) Details of the interface shape and curvature after expansion from the inlet channel and (b) the velocity vectors along the interface (vector length is proportional to velocity magnitude).

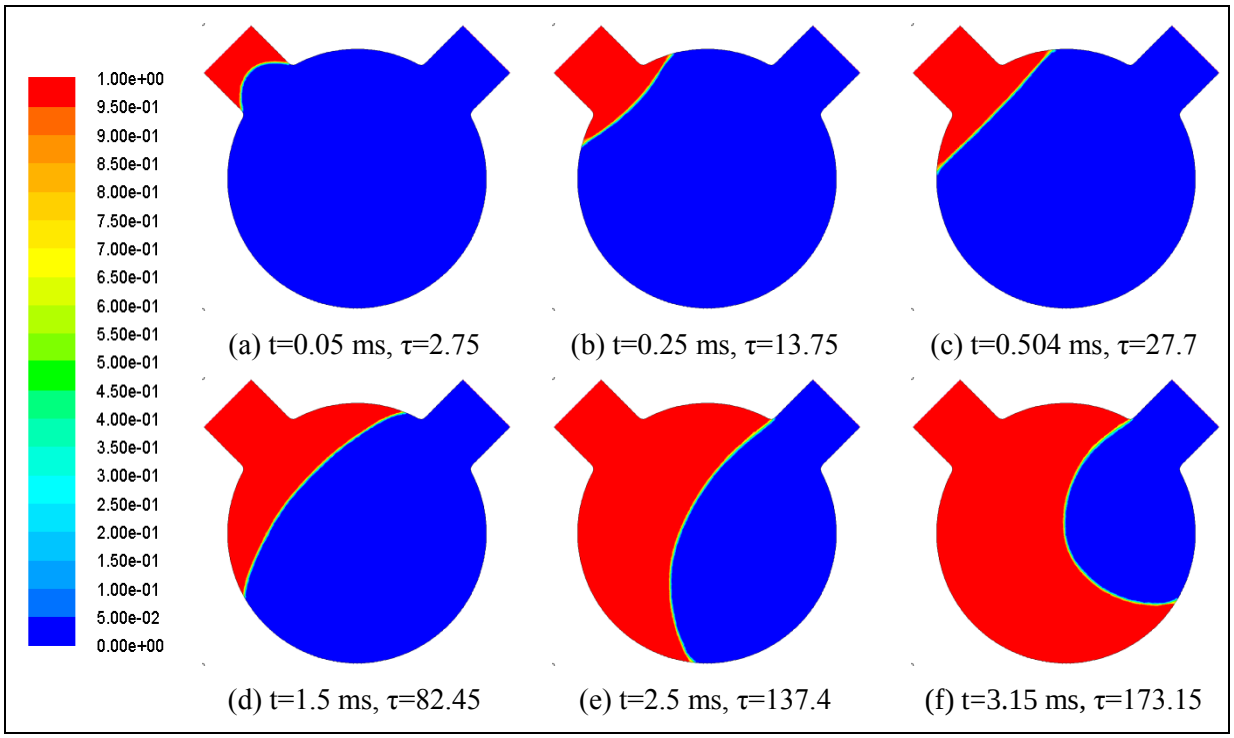

Figure 2.7 Evolving liquid fraction distribution (flow front) during infiltration for a wall contact angle of 30° and zero pressure gradient (wicking flow) at selected time instants.

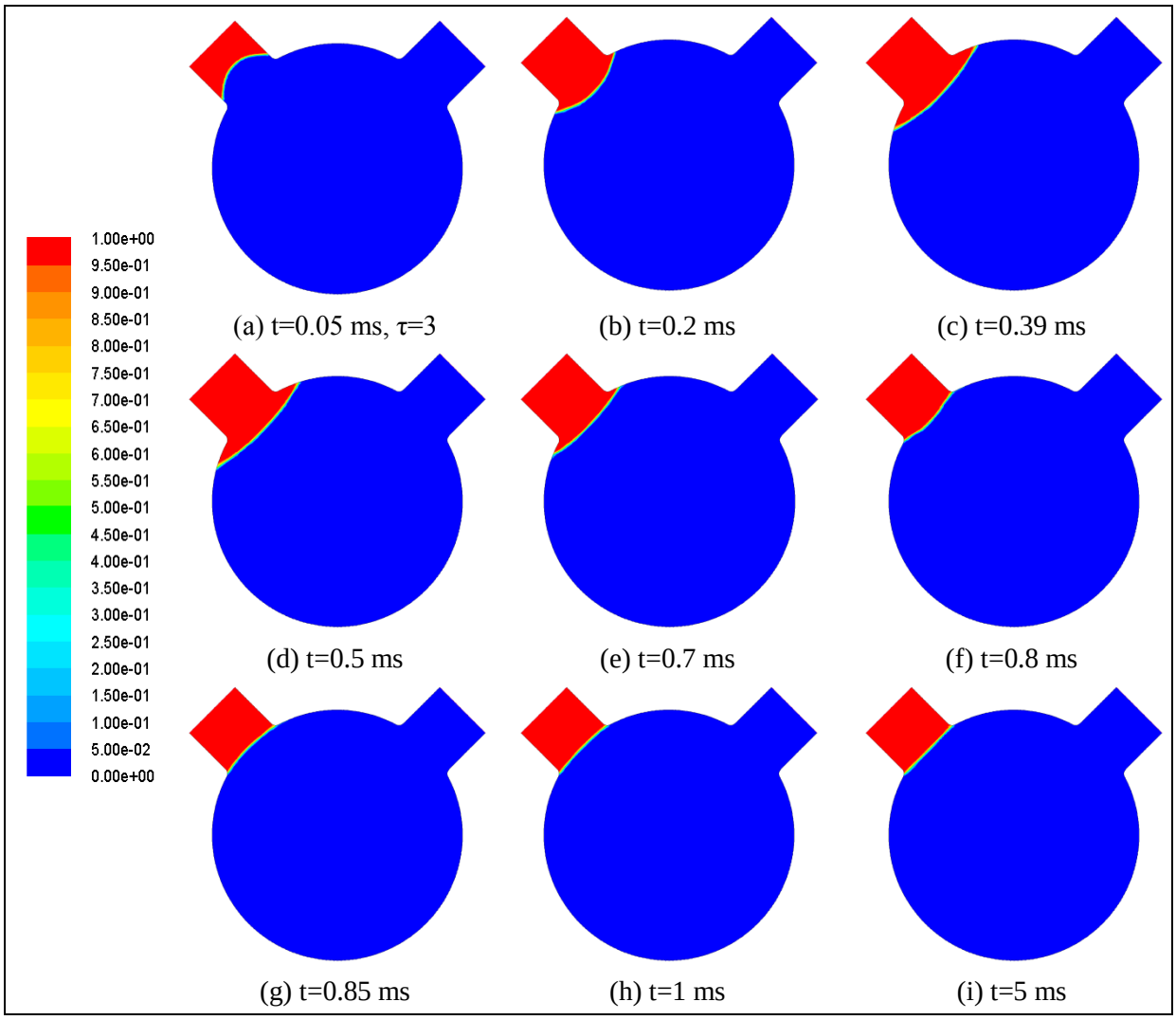

Figure 2.8 Evolving liquid fraction distribution (flow front) during the zero pressure gradient infiltration (wicking flow) for a wall contact angle of 45° at selected time instants.

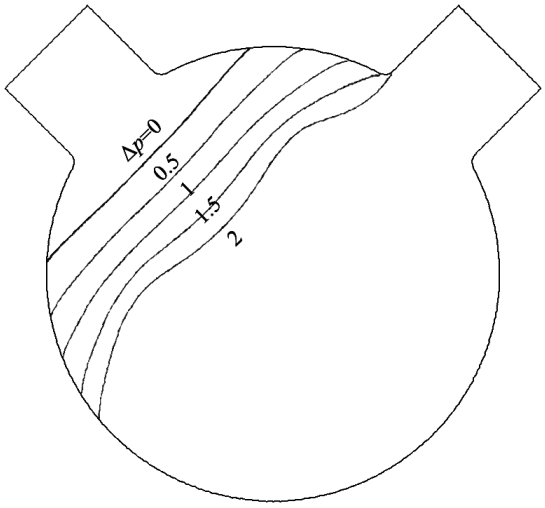

Figure 2.9 Position and shape of the interface at t=500 μs and θ=30° for different values of the dimensionless pressure difference.

(a)

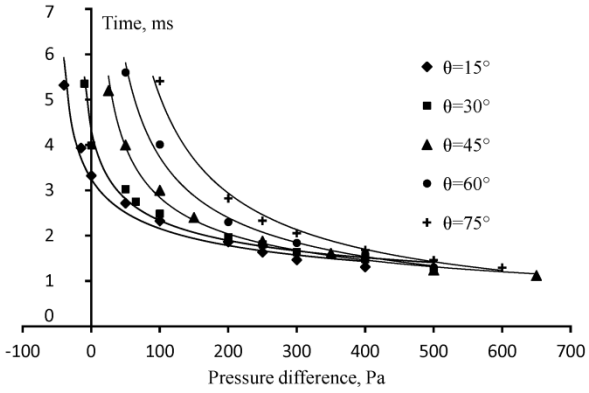

(b)

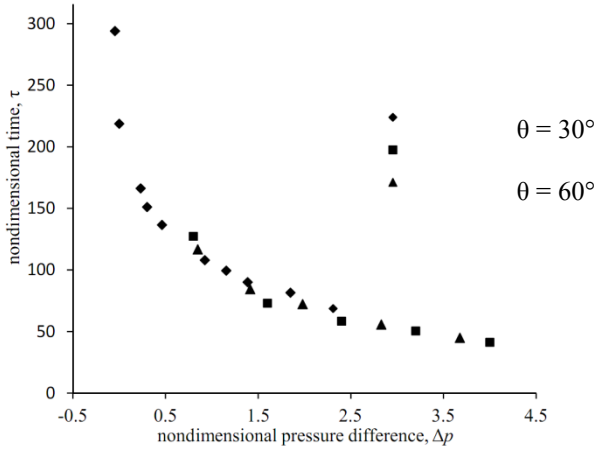

(c)

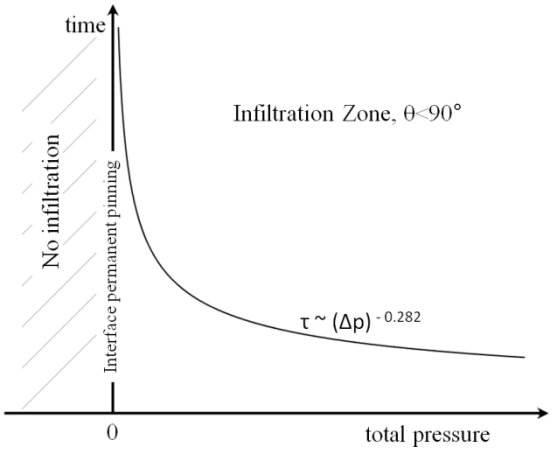

Figure 2.10 (a) Infiltration time versus pressure difference in wetting liquids for different contact angles, (b) Generalized infiltration behavior using nondimensional time versus pressure and (c) Pore infiltration criterion along with permanent pinning regions for wetting liquids.

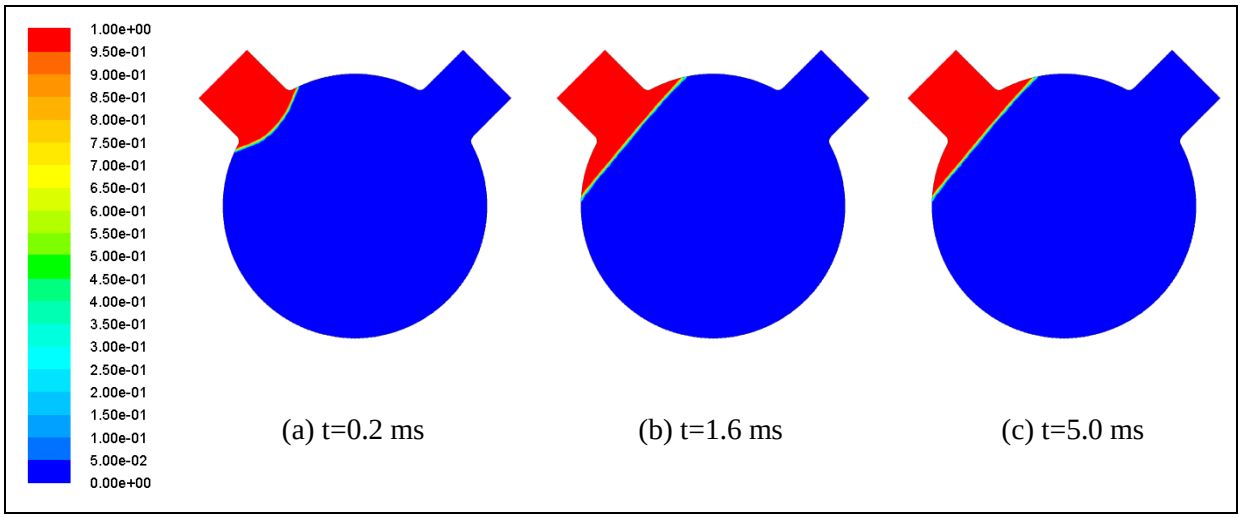

Figure 2.11 Permanent pinning of liquid interface within the pore under a pressure difference of –20 Pa and a contact angle of 30°.

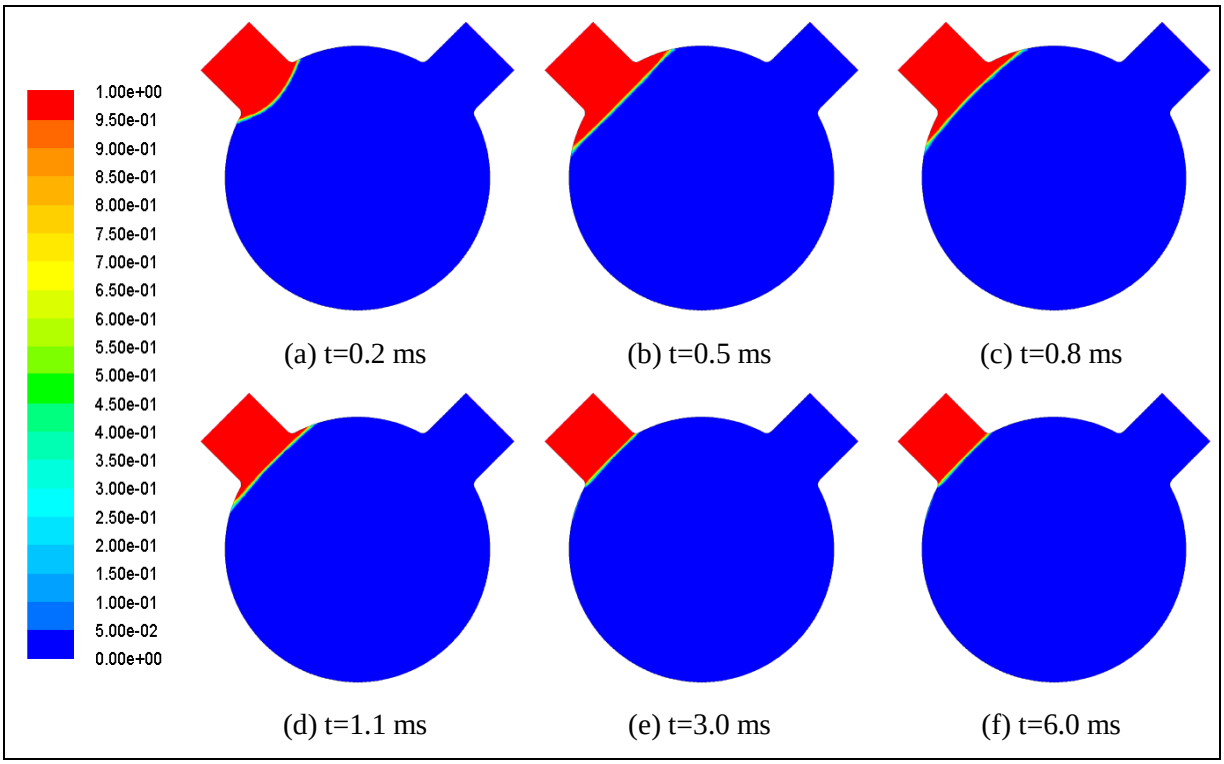

Figure 2.12 Permanent pinning of the interface within the inlet channel under a pressure difference of -40 Pa with interface recession (contact angle is 30°).

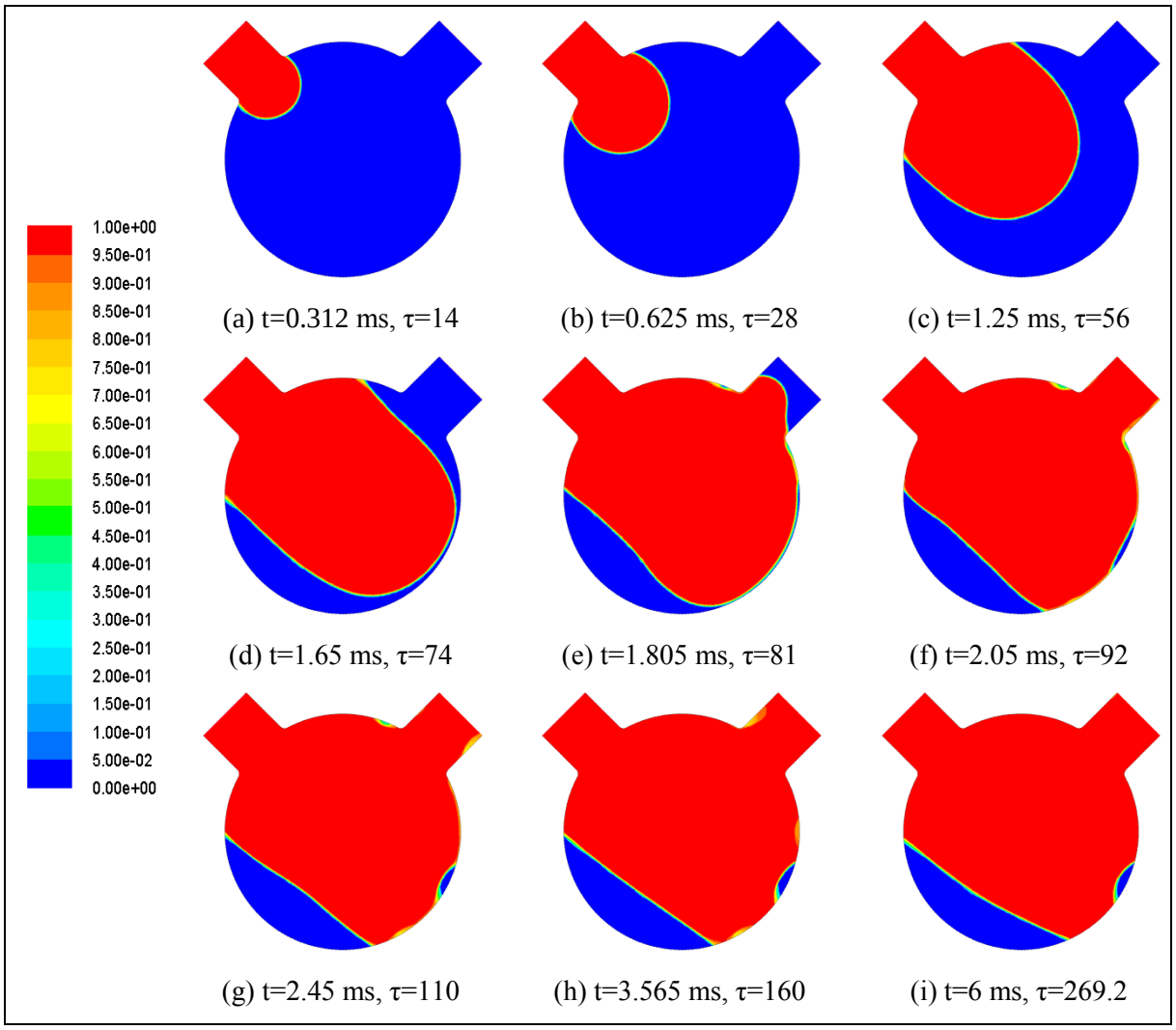

Figure 2.13 Evolving liquid fraction distribution during infiltration of the pore for the wall contact angle of 120° and a pressure difference of $|\Delta p|$=10 at different time instants.

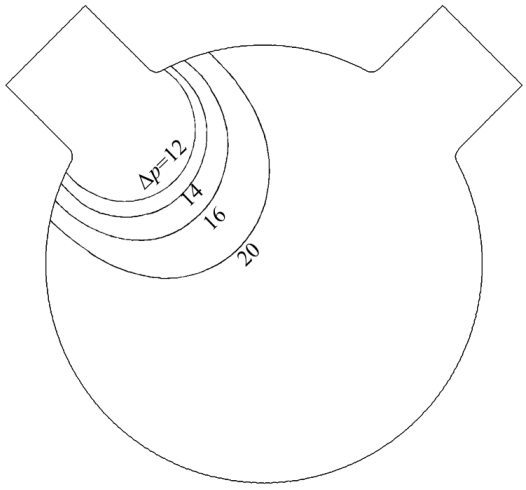

Figure 2.14 Position and shape of the interface at t=500 μs and θ=120° for different values of the dimensionless pressure difference.

(a)

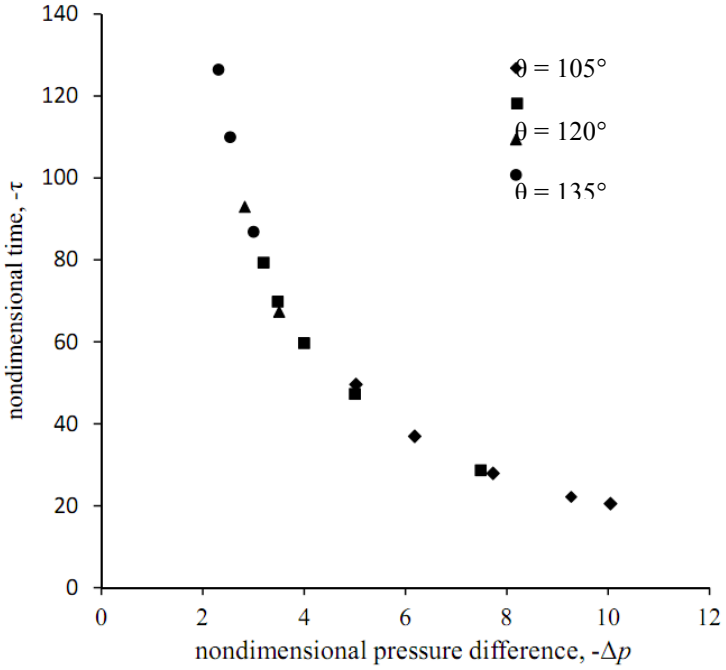

(b)

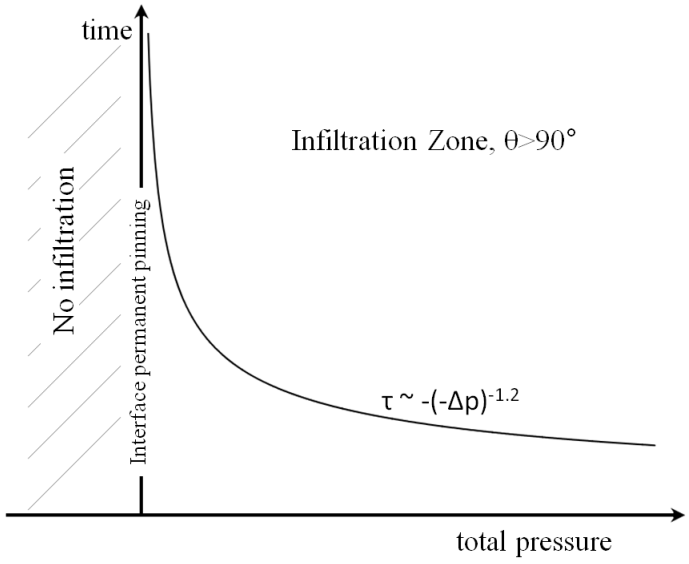

Figure 2.15 (a) Pore infiltration time versus pressure difference for non-wetting liquids (nondimensional variables), and (b) Schematic diagram of pore infiltration criterion along with the permanent pinning regions.

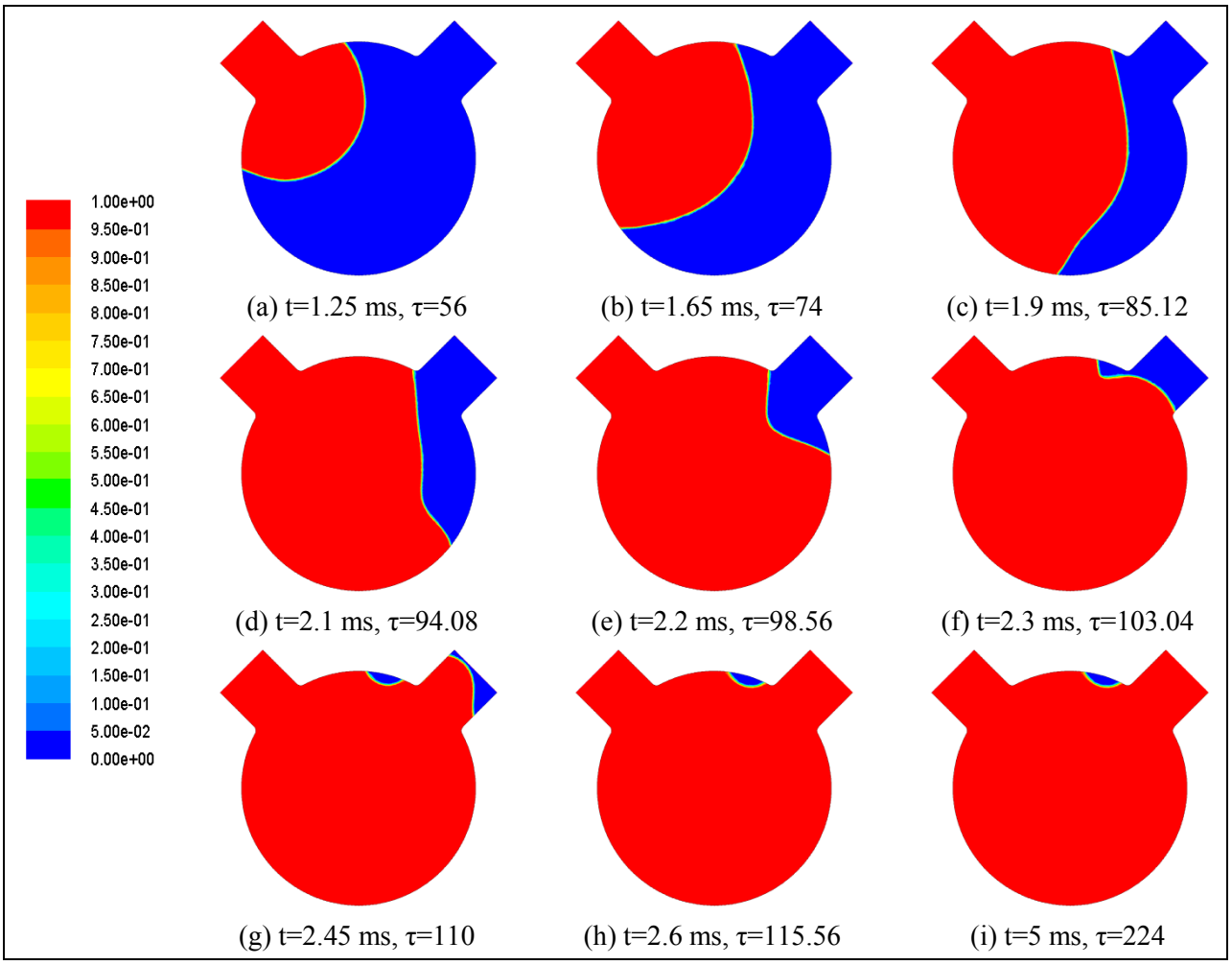

Figure 2.16 Evolving liquid fraction distribution during infiltration of the pore for a wall contact angle of 120° and a pressure difference of $|\Delta p|$=5 at different time instants.

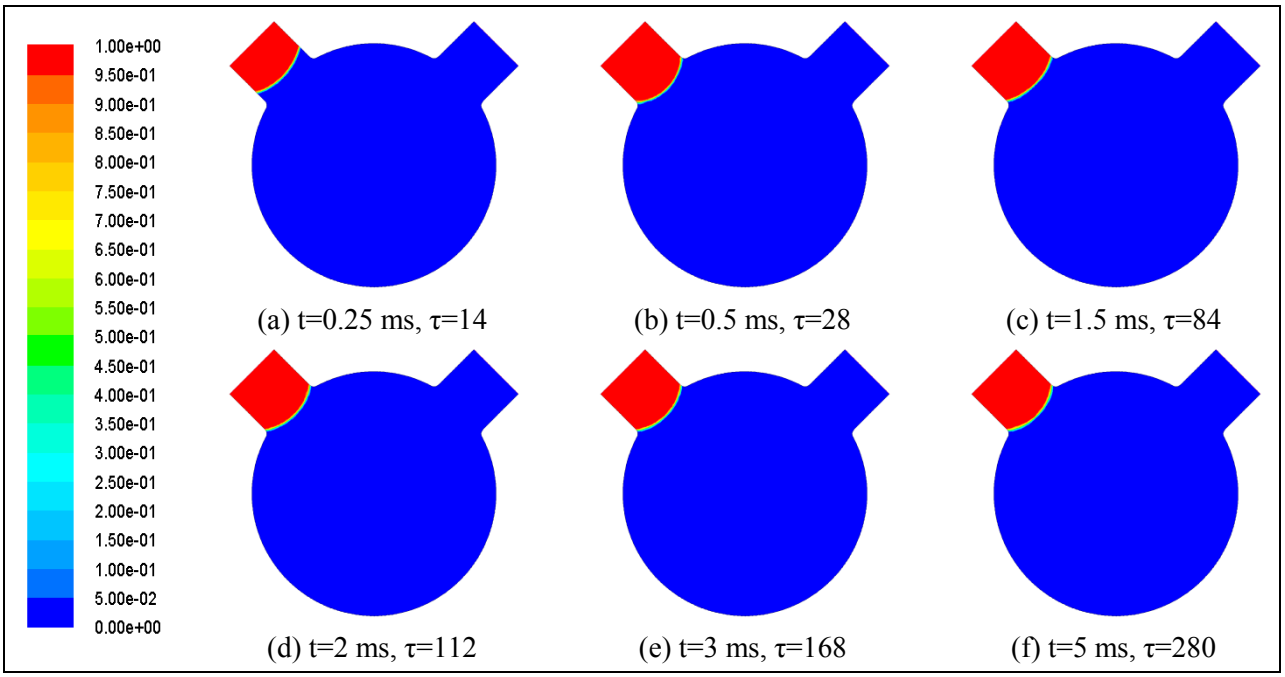

Figure 2.17 Evolving liquid fraction distribution highlighting the permanent pinning of the interface for a wall contact angle of 120° and a pressure difference of $|\Delta p|=2$ at different time instants.

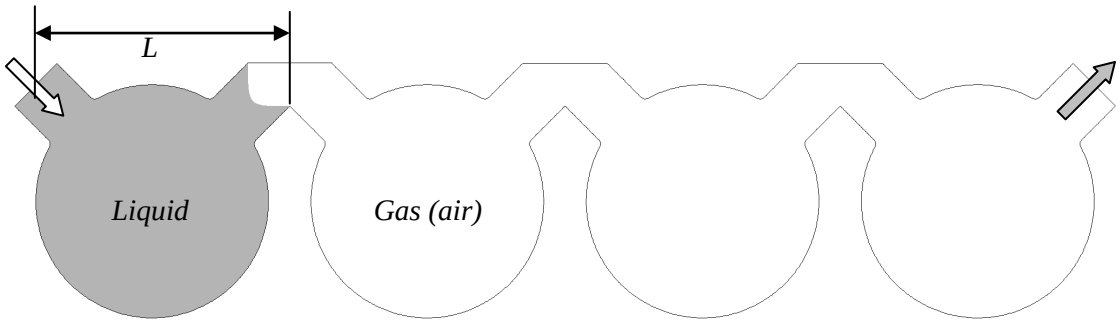

Figure 2.18 Two-dimensional model for network of pores in series and liquid penetration length into the porous structure.

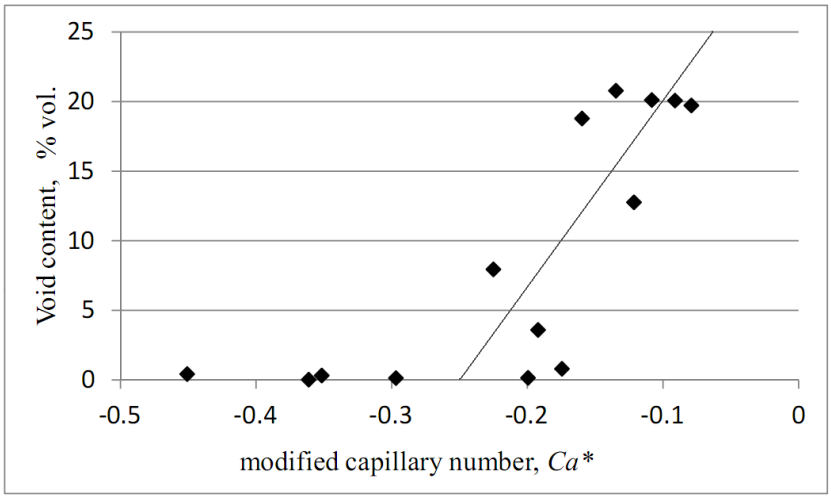

Figure 2.19 Void content of the pore versus the modified capillary number.

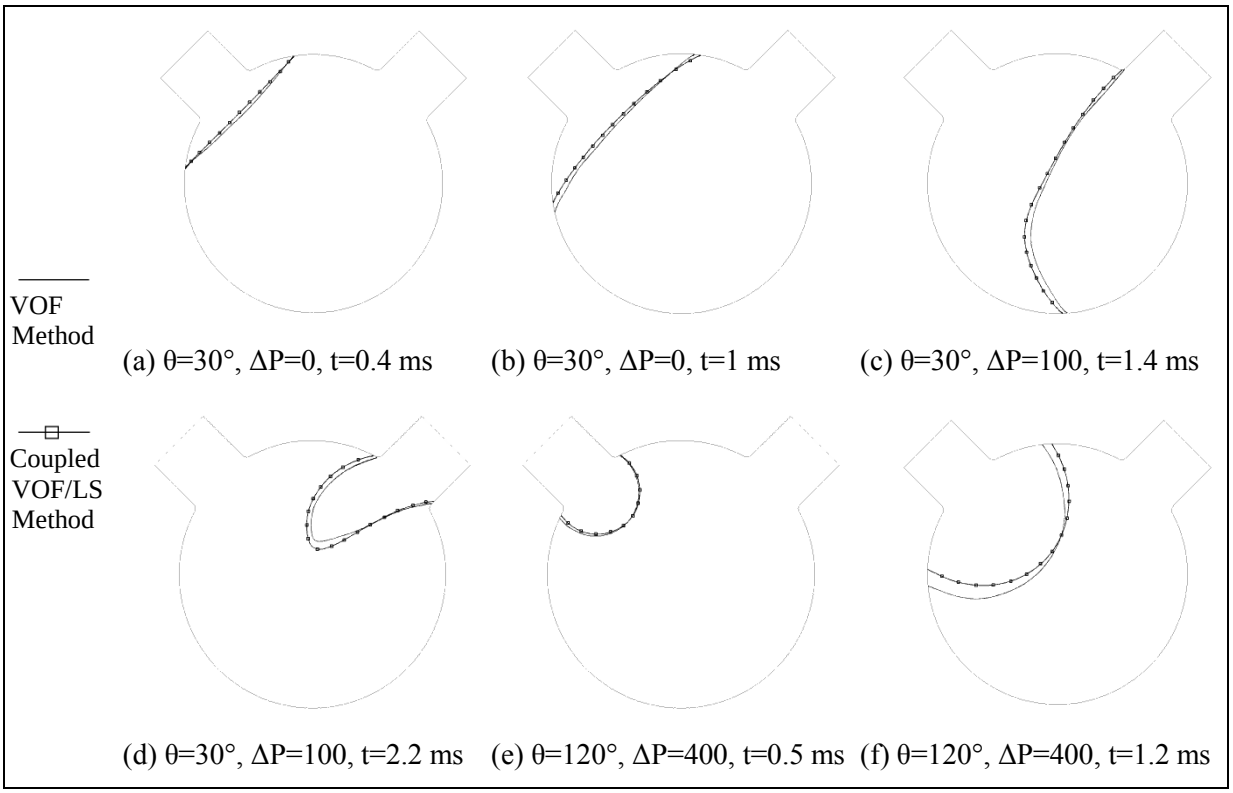

Figure 2.20 Comparison of the shape and position of liquid interface predicted by the VOF and CVOFLS methods for wetting and non-wetting liquids under different pore pressure differences.

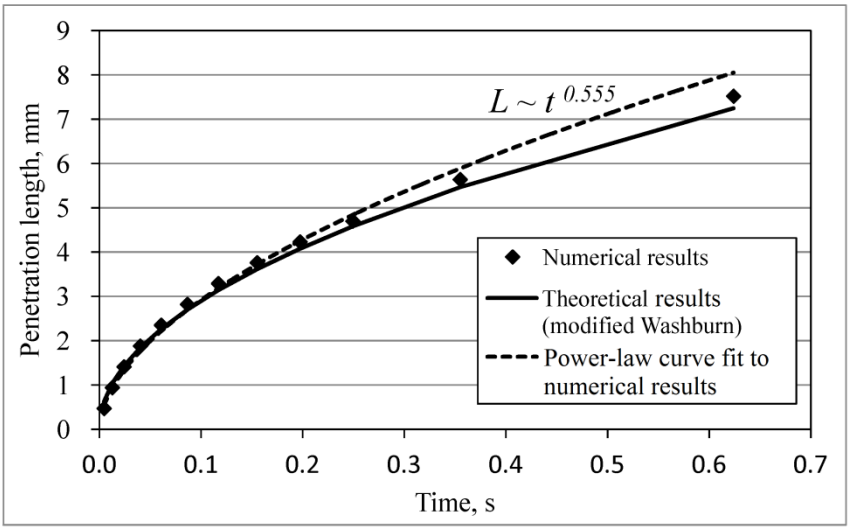

Figure 2.21 The liquid penetration length versus elapsed time in horizontal wicking flow (numerical versus theoretical results).

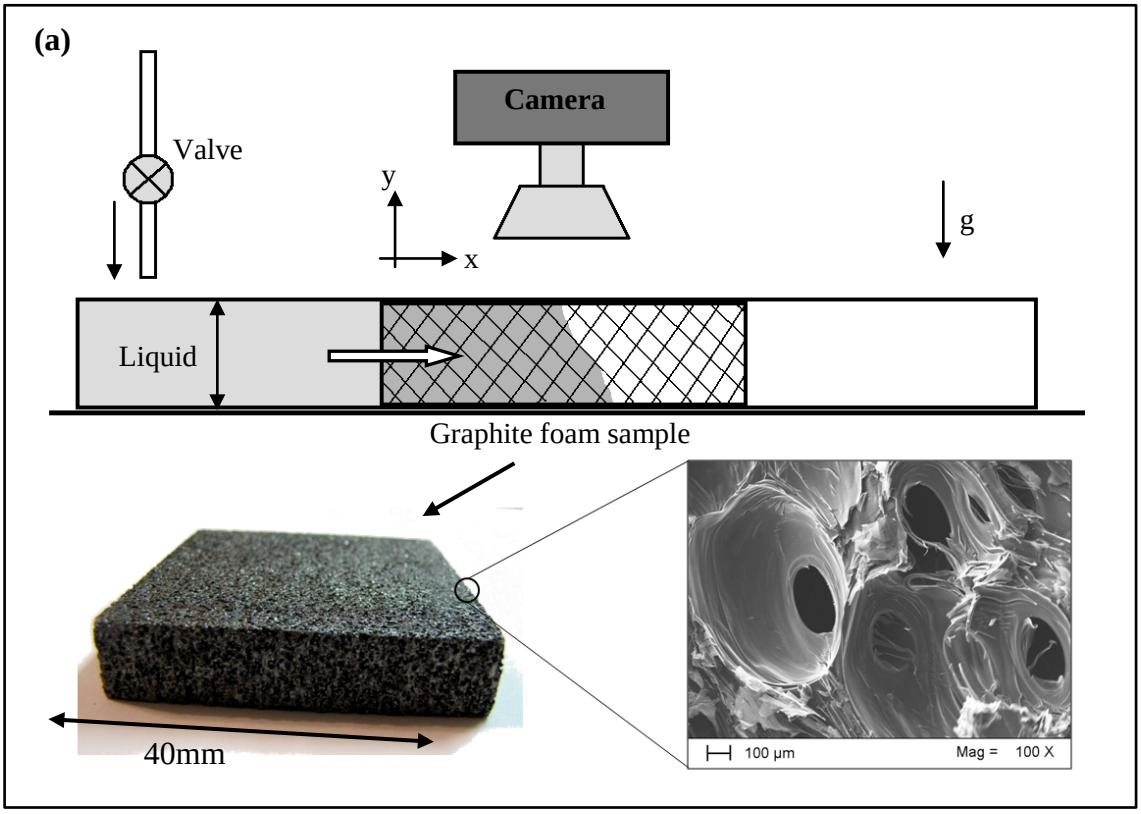

Figure 2.22 (a) Schematic diagram of the experimental setup for wicking flow through the graphite foam, and (b) experimental results of wicking flow (left to right) through a sample of graphite foam at different time instants.

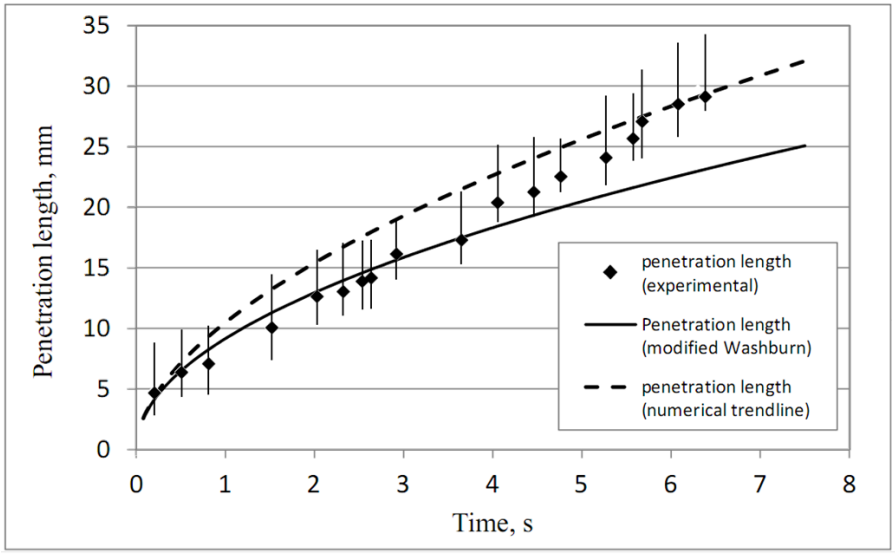

Figure 2.23 Comparison of the liquid penetration length vs. elapsed time among the numerical, experimental and theoretical models (filled symbols represent the experimental measurements of the average position of the liquid front at each time instant. Since the observed liquid front is not flat, the maximum and minimum penetration lengths were also shown using the bars for each experimental measurement).

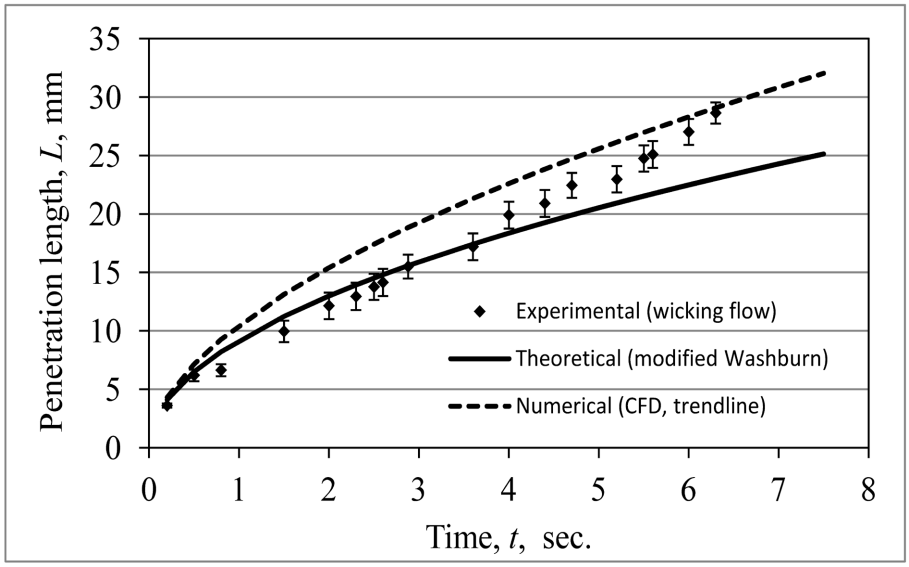

Figure 2.24 Experimental results of the average penetration length (filled symbols) versus time and corresponding uncertainties with a confidence level of 95% (vertical bars), in comparison with theoretical (modified Washburn equation) and numerical results (Moeini Sedeh and Khodadadi, 2013D).

Chapter 3 Phase Change in Thermal Energy Storage Systems

Infiltration was investigated in chapter 2 as a fundamental process in the development of thermal energy storage (TES) composites. It was shown that during infiltration, voids within the composite might be formed. Utilization of such composites involves freeze/thaw cycles during which solidification and melting of the infiltrated phase change materials (PCM) occur. Presence of voids, volume expansion and contraction due to phase change and thermocapillary effects were addressed in literature to have noticeable effects on phase change processes during utilization of TES systems. Such issues were investigated and are presented in this chapter as a continuation of investigation of infiltration process and void formation presented in chapter 2.

3.1 Introduction

Infiltration of phase change materials into a highly-conductive porous structure is a fundamental process in development of thermal energy storage composites with improved effective thermal conductivity. However, during this process, formation of voids in the form of micron-size gas bubbles within the TES composites might also be encountered. As presented in chapter 2, such voids are formed within the pores of graphite foam. The presence of voids within graphite pores (i.e. the presence of air next to the conductive walls of the graphite foam) significantly affects the thermal and phase change behavior of the composite. Therefore, it is important to investigate the effect of voids on phase change behavior during utilization of latent heat TES composites. A numerical approach was employed to study the solidification of PCM infiltrated into a graphite pore in presence of a void. For this purpose, the adopted method should

take into account presence of different phases (including PCM as a liquid, solid or a combination of liquid and solid and void as a gas) as well as the phase change (solidification and melting) of the PCM. Thus, a combination of the Volume-of-Fluid (VOF) and the enthalpy-porosity methods was employed using a two-dimensional model of the graphite pore structure. The proposed method is capable of tracking the evolution of the freezing/melting front within the PCM during solidification and melting. Furthermore, this method is capable of simulating the volume change during solidification and melting (i.e. formation of the shrinkage void). In addition to thermal effects, the interfacial effects have to be considered in this problem due to their important role in the scale of the pore (average pore diameter of 400 microns). This problem is time-dependent and continues until the entire liquid PCM within the pore experiences phase change (solidification or melting). Details of the adopted method, obtained results and verification are presented after the literature review of the relevant research are discussed. The findings of this research were published (Moeini Sedeh and Khodadadi, 2012, 2013E).

3.2 Literature Review (Phase Change in Presence of Voids in TES Composites)

Phase change processes are wide-spread in nature as well as a number of engineering applications such as solar engineering and thermal management systems. Transitions from one state of matter (phase) to another involve energy transfer (absorption / release of latent heat) under nearly constant temperatures. In particular, materials with high values of the latent heat property, known as phase change materials, can be employed for thermal energy storage purposes during the phase change processes. PCM are attractive in a variety of applications due to a large number of PCM that solidify/melt over a wide range of temperatures (Sharma et al., 2009). However, low thermal conductivity of PCM is a major drawback that elongates the solidification/melting time noticeably and limits the achievable heat flux. Therefore, a variety of

thermal conductivity enhancers (metal fins, metal matrices, metal and graphite foams, encapsulation, and dispersed highly conductive micro and nanoparticles) have been proposed and studied in recent years to promote the thermal conductivity of PCM (Fan and Khodadadi, 2011, Khodadadi et al., 2013).

Specifically, highly-conductive graphite foam with high porosity (in the range of 65 to 85%), developed by Klett et al (2000, 2004), is one of the best candidates for thermal conductivity and heat transfer improvement in different applications. Due to high porosity, PCM in liquid state can be infiltrated into the graphite foam to form a composite, suitable for thermal energy storage and thermal management applications. Therefore, among different methods of thermal conductivity improvement, employing highly-conductive porous structures of graphite and metal foams to impregnate with PCM was studied and found to be an effective method resulting in noticeable improvements.

Mehling et al. (2000) presented their experimental data on the thermal conductivity and wall heat transfer coefficient of PCM graphite composite. The experiments show that PCM graphite composite has significantly higher thermal conductivity compared to pure PCM so that the phase front moves 10-30 times faster. Examining the PCM graphite composite, they reported the presence of 10 vol% void (remaining air) in the final composite.

Boomsma and Poulikakos (2001) developed a numerical model to study the effective thermal conductivity of a three-dimensional representative elementary volume of metal foam, fully-saturated with a liquid. They used a simplified model of cylindrical ligaments to represent metal foam geometry. The results show that despite the high porosity of the foam (i.e. 95% porosity for aluminum foam), the overall effective thermal conductivity is strongly influenced by the high thermal conductivity of solid foam structure.

Mesalhy et al. (2005) performed a numerical study for enhancing the thermal conductivity of phase change material using a high thermal conductivity porous matrix. They reported that the presence of the porous matrix increases the heat transfer rate as well as melting rate. They did not consider the effects of voids in this study.

Marin et al. (2005) studied the improvement of a TES system due to the application of paraffin-graphite composite in the form of plates. Using paraffin embedded in porous matrix of graphite, their numerical and experimental results show considerable decrease in charge/discharge (i.e. solidification/melting) time of the TES system, as well as power consumption of fans. However, the effects of voids were not included in their study.

Nayak et al. (2006) considered the effectiveness of plate-type fins, rod-type fins and porous matrices as thermal conductivity enhancers in improving the overall thermal conductance of phase change materials in a heat sink application. Using a numerical model, they investigated the variation of heat source temperature, melt fraction and dimensionless temperature difference versus time within the PCM. They found that although fins improved the overall thermal conductivity of PCM composite, inserting an aluminum matrix into PCM (eicosane) can offer an order of magnitude increase in thermal conductivity and melting rate.

Numerical investigations of simplified three-dimensional models of metal foams were carried out by Krishnan et al. (2006, 2008). They found that the overall thermal conductivity has a noticeable increase compared to pure PCM. In fact, the overall thermal conductivity is controlled by the high thermal conductivity of solid phase. Another advantage of porous solid structures is that due to the high porosity of these structures (especially metal and graphite foams), they occupy a small volumetric portion, while they give a significant rise to heat transfer surface and are highly conductive. In effect, a sharp improvement in the overall thermal

conductivity is observed. These features have made metal and graphite foams very suitable for thermal energy storage applications so that a great deal of research has been conducted on this topic during the recent years.

Sari and Karaipekli (2007) reported thermal conductivity and latent heat TES characteristics of different paraffin/expanded graphite composites. They found that a composite of paraffin with 10 wt% expanded graphite is form-stable which allows no leakage of molten paraffin during the phase change due to interfacial effects. Additionally, a noticeable reduction of paraffin melting time was reported. However, the amount of void (remaining air) was not reported for different samples.

Lafdi et al. (2008) performed a numerical study to predict the thermal performance of graphite foams infiltrated with PCM. The results show that thermal performance of PCM graphite composite was improved significantly due to the high thermal conductivity of graphite. In other words, the output power (proportional to maximum achievable heat flux) was improved 5-8 times and PCM graphite composite response time is faster than pure PCM. They developed a volume-averaged numerical model of the saturated PCM/graphite foam (i.e. no voids).

Generally, there are different phenomena that can lead to the formation of voids such as infiltration, chemical reactions, vaporization, solidification and melting. In the case of TES composites, infiltration of PCM into the porous structures contributes to void formation that was studied and reported in chapter 2. The results show the presence of voids in graphite pores after infiltration. In other words, there is a trapped portion of gas that is poised stably within the pores of graphite foam, and it is possible to estimate the volume of this void space using the VOF method. Thus, such portion of void is present within the composite during the utilization of TES systems as they undergo solidification and melting processes.

The other contribution to void formation during solidification and melting is the volume change (expansion and contraction due to density changes). Considering a certain mass of PCM experiencing phase change, the volume changes due to the difference between densities of different phases. Such volume change also contributes to formation of void, known as shrinkage void. Sulfredge et al. (1999) studied the thermodynamics and heat transfer of shrinkage voids, void nucleation and growth, and some modification techniques for void pattern for a constant volume environment.

Investigation of the effect of voids on phase change processes is vital in TES systems due to the significant effects of void presence on thermal behavior and freezing/thaw cycles. Voids (usually in the form of micron-size air bubbles) in graphite pores will demonstrate a different thermal behavior than other components of the composite, i.e. PCM and graphite structure, and can limit the incoming/outgoing heat flux from the adjacent walls. Depending on the volume and distribution of voids, the process of solidification or melting will be altered at the pore level as well as system level. As a result, prediction of void formation, the volume of voids and their location/ distribution are crucially important in considering the thermal behavior of TES composites. In this chapter, the phase change processes of solidification and melting in presence of a void (from infiltration process) are investigated. Furthermore, formation of shrinkage voids in the presence of an infiltration void will be studied numerically at the pore level for PCM infiltrated in a graphite foam porous structure.

3.3 Modeling and Grid Generation

A simplified two-dimensional model similar to the model used for investigation of the infiltration process in chapter two was developed based on the geometrical features of graphite foam as shown in figure 2.1. Based on the grid independence study presented in chapter 2, the

same unstructured quadrilateral grid system was selected for investigation of phase change within the pore in presence of a void. Based on the spatial and temporal grid independence studies, a final grid system with 35000 cells was selected with a time step size of 1 μs for phase change simulations. The grid is fine near the walls (compared to the interior of the pore, as shown in figure 2.2c) to provide better accuracy in movement of void (i.e. contact points on the walls of the pore) as a result of interfacial or buoyancy forces within the pore during the phase change process.

3.4 Governing Equations and Dimensionless Parameters

In the previous chapter, the infiltration process was considered as a two-phase problem involving a liquid PCM penetrating into the pores of graphite foam, initially occupied by air. The governing equations (continuity, momentum and volume fraction) were solved numerically using the volume-of-fluid (VOF) method (Hirt and Nichols, 1981) for each phase during the transient infiltration process and the final state of the pore was determined. The two contributing phases in the infiltration process were the liquid PCM and gas (air as void) that were differentiated using the VOF volume fraction.

In this chapter, solidification and melting of PCM is investigated in presence of a void within the pore. Thus, both phases of liquid (PCM) and gas (air) are initially present within the pore and only one phase (PCM) experiences the phase change process (solidification or melting). The phase change process can be solved numerically using the enthalpy-porosity method (Beckermann and Viskanta, 1988; Brent et al., 1988) during which a liquid fraction (ε) discriminates between the liquid and solid (frozen) phases. Upon start of the phase change process, part of the PCM (which is initially liquid) solidifies and three phases of solid, liquid and gas are present within the pore. As a result, a combination of both methods is needed to solve

this problem and differentiate between the three available phases. In other words, the enthalpy porosity method with only one liquid fraction cannot distinguish between three phases and another fraction (i.e. VOF volume fraction) is also needed.

In order to illustrate the adopted model of multiphase flow and heat transfer, relevant dimensionless parameters were identified. These dimensionless variables were introduced into the adopted model of multi-phase flow (the pore contains liquid PCM and a gas bubble as void) and phase change (solidification and melting of the liquid PCM within the pore) as:

$$x_i = \frac{X_i}{d}\ ,\ \tau = \frac{t\alpha}{d^2}\ ,\ p = \frac{Pd^2}{\rho\alpha^2}\ ,\ \theta = \frac{T - T_c}{T_h - T_c}, \tag{3.1}$$

where x_i, τ, p and θ stand for the dimensionless space coordinate, time, pressure and temperature, respectively. Selection of the above dimensionless variables will lead to the dimensionless governing equations (equations 3.2-3.4) for the solidification/melting of PCM within the pore. These equations govern the phase change of the PCM, which is initially in liquid state and quiescent within the pore (upon completion of infiltration).

$$\nabla \bullet \boldsymbol{u} = 0\ , \tag{3.2}$$

$$\frac{\partial \boldsymbol{u}}{\partial \tau} + (\boldsymbol{u} \bullet \nabla)\boldsymbol{u} = -\nabla p + \mathrm{Pr}\nabla^2 \boldsymbol{u} + Ra\,\mathrm{Pr}\,\theta\,\boldsymbol{n_g} \underbrace{- \frac{(1-\varepsilon)^2}{\varepsilon^3}\left(\frac{A_{mz}\, d^2}{\rho\alpha}\right)\boldsymbol{u}}_{I} + \underbrace{\frac{\sigma d^2 K_i}{\rho_{avg}\,\alpha^2}\nabla\lambda_i}_{II} \tag{3.3}$$

It should be noticed that there are initially two phases of liquid (PCM) and gas within the pore resulting from the simulation of infiltration process using the VOF model. Therefore, these two phases are distinguished by the VOF liquid fraction (λ_i). During the solidification or melting, phase change occurs only for one phase (i.e. PCM). As a result, there are three phases

of solid (frozen PCM), liquid (PCM) and gas (the void) within the pore simultaneously. Thus, the liquid and solid phases are differentiated using the phase change liquid fraction (ε).

For simulation of the solidification process, the enthalpy-porosity method was utilized in which the mushy zone is treated as a porous zone and its porosity is equal to the liquid fraction. In fact, within the mushy zone, the presence of the solid (frozen) phase affects the diffusion of the liquid phase. As a result, a sink term appears in the momentum equation (term I on the right side of equation 3.3) to represent this effect. The last term on the right side of the momentum equation 3.3 (term II) represents the dimensionless corresponding terms of the surface tension effects (between the liquid and gas phases in the VOF model) and is evaluated based on the continuum surface force (CSF) model (Brackbill et al., 1992).

The dimensionless form of the thermal energy equation has the following form:

$$\frac{\partial \theta}{\partial \tau} + \boldsymbol{u} \bullet \nabla \theta = \nabla \bullet (\nabla \theta) - \frac{1}{Ste} \frac{\partial \varepsilon}{\partial \tau} \tag{3.4}$$

It should be mentioned that the gas phase (void) was considered as a compressible ideal gas in the present model. Therefore, equations 3.1–3.4 describe the other phase (PCM) experiencing a phase change process in the form of solidification or melting. The set of governing equations incorporating the VOF and enthalpy-porosity methods were solved numerically using the finite volume technique (commercial CFD code Fluent 13.0, 2010).

In order to quantify the volume and distribution of shrinkage void, the final volume of the solidified PCM within the pore is compared to the initial volume of the liquid PCM. The volume change occurs during phase change from liquid to solid as a result of the different densities of the two phases. Thus, the density needs to be defined as a function of temperature to account for density changes between the liquid and solid phases. Variation of density can be either confined

to a linear function in the mushy zone temperature range (i.e. between solidus and liquidus temperatures) following with constant densities for liquid and solid states, or it can be defined as a piece-wise polynomial over different ranges of temperature corresponding to the solid, mushy zone and liquid states. The density function used in this study consists of constant densities for each phase (solid and liquid) with a linear variation from the solid density to the liquid density in mushy zone, as shown in figure 3.1.

More details on governing equations, characteristic quantities and dimensionless groupings can be found in Crank (1984), Voller et al. (1987, 1989), Beckermann and Viskanta (1988) and Brent et al. (1988).

3.5 Boundary Conditions and Computational Details

Upon infiltration and availability of the final PCM composite, it will be ready for thermal energy storage as it is subjected to charge/discharge (i.e. freezing/melting) cycles. Therefore, the initial condition for solidification is the final condition of infiltration process. Considering the multiphase flow of PCM penetrating into the porous structure due to pressure gradient, gravity and surface tension, and solving the transient problem of infiltration using the volume-of-fluid (VOF) method, the final condition of infiltration can be determined (Moeini Sedeh and Khodadadi, 2013C). This two-phase simulation is able to predict the formation of void during the infiltration process as it was carried out for the case of a wall contact angle of 90° and the Capillary number of Ca=0.05 corresponding to infiltration of a non-wetting liquid into the graphite foam and formation of a void as shown in figure 3.2. The red and blue colors stand for the liquid and gas phases, respectively. Surface tension forces were treated based on the continuum surface force (CSF) model developed by Brackbill et al. (1992). The final status of

the PCM within the pore at the conclusion of infiltration is shown in figure 3.3, showing a portion of 9.8% infiltration void (by area) within the pore (in red).

The infiltration void forms mainly due to wetting nature of the liquid, interplay of driving forces and geometry of the pore. After infiltration, the PCM composite goes through freezing/melting cycles. Thus, in order to investigate the solidification process and consider the formation of the shrinkage void, the final infiltration state (shown in figure 3.3) was considered as the initial condition of the solidification process. There is also a portion of stable air as a void inside the pore, treated as a compressible fluid that does not undergo phase change. The PCM which is initially a liquid experiences the phase change process and solidifies due to the imposed thermal boundary conditions. The initial temperature was set to 280 K where the PCM is liquid, and the temperatures of different walls (except ports which are adiabatic) were set to 273 K and solidification occurs at 279.3 K. The density of PCM was defined as a function of temperature over the range of solidification as shown in figure 3.1. As the liquid phase goes through the phase change process, density varies (between liquid and solid density) and causes a volume change during phase change. Since density of cyclohexane increases during the solidification, the volume shrinks, which leads to formation of shrinkage void. The volume and distribution of shrinkage void were considered in detail for the studied case. Finally, other numerical values were set based on material properties of cyclohexane except thermal conductivity which was set to 5 W/m K to expedite the solidification process and reduce the required computational time. It needs to be mentioned that changing the value of the thermal conductivity affects the values of the dimensionless variables (*Ra* and *Pr*) that appeared in the momentum equation (equation 3-3) in the terms corresponding to the gravitational and viscous effects. However, the gravitational and viscous terms are negligible in comparison with the surface tension term at the pore level as

also indicated by the scale analysis in chapter 2 (*Ca* and *Bo* numbers in table 2-1). As a result, there is no change in convection patterns within the pore and setting a higher value for the thermal conductivity only expedites the numerical simulation of the phase change. Furthermore, the corresponding Stefan number (*Ste*) in phase change simulations remains constant (0.4). Cyclohexane was selected as a typical PCM and Yaws (2008) and Silva et al. (2009) were used for the relevant thermophysical properties.

3.6 Results and Discussion

The numerical simulation of the phase change processes (solidification and melting) were conducted using the combination of the VOF and the enthalpy-porosity methods. The results of solidification and melting are presented separately in sections 3.6.1 and 3.6.2, respectively.

3.6.1 Solidification in Presence of Void

Based on the described method, numerical simulation of solidification of the PCM was performed by combining the VOF and enthalpy-porosity methods. The time-dependent liquid fraction contours during the solidification process for a case of Ste=0.4 are shown in figure 3.4. One should notice that the infiltration void, which is initially present in the pore, does not undergo phase change and is treated as a region with a liquid fraction of 1.0 in figure 3.4. Therefore, the infiltration void is shown in red color as well as the liquid portion of PCM in figure 3.4. The solidification of the liquid content of the pore is driven by the lower temperature of the walls. Thus, the liquid in contact with the walls solidifies at early time instants. The solidification pattern is observed to be nearly in the radial direction (figure 3.4a to c). The liquid next to the infiltration void also starts to solidify more notably at later time instants (figure 3.4d

to f). The central zone of the pore undergoes solidification at later stages. As liquid experiences solidification, its volume changes and a shrinking is observed at the pore level.

Eventually, after solidifying the whole liquid content of the pore, the pore contains two phases of solid (frozen PCM) and gas (air or void) and the final status of void is clearly realizable, as shown in figure 3.5. The void in figure 3.5 represents the total volume of infiltration and shrinkage voids. Therefore, comparing the volume of the void before and after solidification (figures 3.3 and 3.5, respectively), one should be able to differentiate the shrinkage void from the initial infiltration void. Consequently, the shrinkage void and its distribution were extracted and shown in figure 3.6. For this case, the volume of the shrinkage void is evaluated to be 1.3% for the current model. Additionally, the proposed method also predicts the distribution of the shrinkage void within the pore as it can be observed in figure 3.6. This distribution is in accordance with natural convection patterns within the pore. There is a single clock-wise rotating vortex within the pore (figure 3.7) moving liquid PCM from the lower portion of the pore to the upper portion of the pore while the liquid is cooling down and freezing. As a result, the thickness of the shrinkage void is thin at the upper parts of the PCM/void interface (as natural convection supplied liquid there), while it is thick at the lower parts of the PCM/void interface as shown in figure 3.7.

Since the void is initially present within the pore at the conclusion of infiltration, the effect of the infiltration void on the solidification process is considered in this model. Usually, presence of voids increases the thermal resistance between the walls and the PCM. As a result, the shape and speed of the freezing front as well as the time needed for freezing and melting will deviate from the case of having no void or single phase simulations. For the current model, the solidification time of the PCM within the pore in presence of the infiltration void was evaluated

to be 18.1 ms; whereas, for the case of no voids within the pore, the solidification time of 15.2 ms was obtained. As a result, the presence of void elongates the pore-level solidification process about 16% for the present model. This will also affect the total charge/discharge time of the TES system.

3.6.2 Melting in Presence of Voids

The final state of the solidification process (as shown in figure 3.5) with two phases of solid (frozen PCM) and air (as the total void) was considered as the initial condition for the melting process. Similar to solidification, the enthalpy-porosity method was used in combination with the VOF method to simulate the melting of the PCM within the pore in presence of the void. For simulation of the melting process, the thermal boundary conditions for the walls of the pore were set to be above the melting point of the PCM. In order to impose similar thermal conditions to the solidification and melting processes, the thermal boundary conditions for the cold/hot walls were selected so that the same dimensionless temperature is applied to the PCM within the pore. Considering the dimensionless temperature as $(T - T_c) / (T_h - T_c)$, where T_c and T_h are the cold and hot thermal boundary conditions applied to the walls of the pore, selection of $T_c = T_m - \Delta T$ and $T_h = T_m + \Delta T$ will lead to the same dimensionless temperature of ± 0.5 as the thermal boundary condition of melting and solidification. This will make it easier to compare the duration of solidification and melting processes under the same thermal load at the pore level. In the present model, ΔT was selected as 7 ^{o}C which with the melting temperature of $T_m = 280$ K leads to $T_c = 273$ K and $T_h = 287$ K, as the cold and hot temperatures applied to the walls of the pore during solidification and melting. Moreover, the solidification process initiates when the pore contents are at an initial temperature of 280 K with PCM as a liquid within the pore. The

melting process initiates upon freezing the whole PCM content of the pore and continues until the entire PCM melts within the pore.

The instantaneous contours of the liquid fraction during the melting process, showing the evolution of the melting front within the pore are presented in figure 3.8. Compared to the solidification process discussed above, the melting process is observed to deviate from the case of one-dimensional inward thawing in the radial direction. This is due to the existence of stronger natural convection currents as the melting process proceeds. The natural convection patterns are different in melting and solidification processes due to the difference in thermal boundary conditions, applied during the melting and solidification. The model is capable of predicting the flow currents in the molten portion of PCM within the pore during the melting process. Such currents may initiate due to buoyancy-driven convection and possible sinking of the remaining solid PCM due to its higher density compared to the liquid PCM. It should be noticed that sinking of the remaining solid PCM depends on the scale of the gravitational force with respect to the interfacial force (i.e. happens for high ratios of the gravitational to interfacial forces). Such a ratio is expressed by the dimensionless Bond number which is 0.05 for this problem, meaning that gravitational force are negligible compared to the surface tension force that is due to the small scale of the pore. Returning to the discussion of the buoyancy-driven convection, at early instants of melting, the solid PCM melts radially inward away from the hotter walls. The solid PCM that is next to the upper segment of the void also melts faster when compared to the remainder of the solid PCM since the warmest part of the gas in the void also coincides with the upper region due to natural convection. The PCM in the lower portion of the pore also melts faster since the hot melting liquid will rise and natural convection there is

important. Prominences of buoyancy-driven convection in these two regions clearly contribute to the uneven shape of the solid PCM observed in figures 3.8e to i.

During the melting process, slight changes in the shape of the PCM/void interface were observed. However, the void remains stable within the pore and upon melting the entire PCM content of the pore, the volume of the void was evaluated to be about 9.8%, which is the original void content from the infiltration process, as shown in figure 3.9. In fact, the shrinkage void, formed during the solidification process as a result of different densities between liquid and solid PCM, disappears upon completion of the melting process.

Similar to the solidification process, the effect of the infiltration and shrinkage voids on the melting process is considered in this model. The presence of the voids increases the thermal resistance and lowers the heat transfer rate to the melting PCM. As a result, presence of the voids affects the shape and speed of the melting front as well as the time duration of melting compared to a case when there is no void within the pore. In presence of the infiltration and shrinkage voids, the melting time of the PCM within the pore was evaluated to be 17.2 ms versus 14.8 ms for the case of no voids within the pore. Therefore, the presence of the void elongates the pore-level melting process by about 16.2% in the present study. A comparison of melting and solidification times is presented in table 3.1.

3.7 Thermocapillary (Marangoni) Effects

The discussed simulations of solidification and melting were conducted for the purpose of investigating the effect of voids on phase change processes and formation of shrinkage void. For these purposes, a relatively high thermal conductivity was selected for PCM to reduce the computational time and power. Selection of the high thermal conductivity saves the computational time, however it reduces the temperature gradient within the PCM domain and

suppresses the natural convection due to decreasing the Rayleigh number. Even though the thermal conductivity of PCM within the pore was high, the simulations revealed that there is a temperature gradient along the interface between the PCM and void, as shown in figure 3.10 for the case of solidification of PCM within the pore.

Considering the surface tension as the major driving force at the scale of the pore, this temperature gradient is large enough to give rise to a gradient in surface tension and triggers the thermocapillary (Marangoni) convection at the interface. Thus, as a convection mechanism, it affects the phase change process as well as the interface shape. Therefore, the effects of the Marangoni convection on PCM solidification time and shape of the interface needs to be investigated at the pore level. For including the Marangoni effects in phase change, the same numerical approach was employed (that is based on the combination of the VOF and the enthalpy-porosity methods). However, the surface tension was defined as a function of temperature to account for thermocapillary effects, as given in figure 3.11.

In the next sections, after presenting a literature survey on thermocapillary effects during phase change, the phase change processes will be investigated for PCM within the pore in presence of voids including thermocapillary effects. The solidification/melting durations and shape of the final interface between the PCM and void (representing the amount and distribution of the shrinkage void evolving during the solidification) were extracted and compared between the cases with and without the Marangoni convection. Finally, for verification purposes, the volume of the predicted shrinkage void is compared to the theoretical volume change due to the variation of the density. The final shape of the interface is justified with respect to the prevailing Marangoni convection pattern within the pore.

3.8 Literature review (Thermocapillary Effects)

Prediction of the role of the gas voids on thermal behavior of TES systems is essential in order to investigate the thermal performance and details of freezing/thaw cycles during the life time of such systems. Recent studies (Moeini Sedeh and Khodadadi, 2012) on modeling the solidification and melting of PCM within graphite pores in presence of a void space (formed during the infiltration process) confirmed a temperature gradient along the interface between the void and PCM, as shown for a case of solidification in figure 3.10. Since for most of the liquids, the surface tension is a function of temperature, the temperature gradient along the interface indicates that thermocapillary effects are important. Presence of voids implies the presence of liquid-gas interfaces that can trigger Marangoni convection as a result of the temperature gradient along such interfaces and temperature dependence of the surface tension.

An early study was conducted by Antar et al. (1980) to consider the influence of solidification on the onset of surface tension-driven convection in a reduced-gravity environment for cases of stationary and constant-rate solidification. They found that due to solidification process, the critical Marangoni number is shifted to lower values indicating that convection can be realized in the liquid phase at lower Marangoni numbers when solidification is present.

Liu et al. (1993) studied solidification and melting of pure materials, considering liquid convection driven by buoyancy, or a combination of buoyancy and surface tension forces. Their numerical model showed that thermocapillary effects can be of significant influence upon melting and solidification. Additionally, in low Pr number materials, solidification rates are affected by thermocapillary convection more than melting rates.

Khodadadi and Zhang (2000) conducted a numerical study on the effects of thermocapillary convection on melting of spherical droplets under uniform heat flux and zero-gravity conditions. They reported that conduction is the dominant mode of heat transfer during

the early periods of melting, while the thermocapillary convection strengthens later and causes faster melting on the side of the droplet.

Kassemi et al. (2001) conducted a numerical study to investigate the effects of thermocapillary convection generated by a void or bubble on a typical microgravity solidification process. Solving the quasi-steady Navier-Stokes equations coupled with the conservation of energy and species, they included the effects of thermocapillary convection generated by the void and solute rejection at the freezing front. They found that void-generated thermocapillary convection can affect segregation patterns drastically, especially when the thermocapillary vortex penetrates the solutal boundary layer.

The interaction between non-isothermal drops and freezing front in presence of the Marangoni effect was investigated experimentally and numerically by Nota et al. (2006). They found that in presence of a temperature gradient, the surface tension-driven flows at the liquid interface cause shape deformations and affect the interaction of the drop with the freezing front. Based on the experimental evidence, they concluded that a pushing force is induced by the Marangoni effect when the droplets approach the freezing front.

Matsunaga and Kawamura (2006) performed an experimental study on the influence of thermocapillary convection on the solid-liquid interface in the directional solidification of a liquid layer with a free upper surface. They found that the effects of molten material convective flows, i.e. natural and thermocapillary convection strongly affect the resulting quality of the solidified materials through influencing the dendrite structures during the solidification. As a result, the solid-liquid interface is inclined against the wall-normal direction and is curved in the growth direction due to thermocapillary convection.

The reviewed articles indicate that thermocapillary effects can have a significant contribution on phase change in presence of voids or bubbles. Therefore, in order to have a better understanding of thermal behavior and phase change characteristics of TES systems, it is necessary to consider the Marangoni convection in such studies. Thus, as a continuation of previous phase change simulations, the solidification and melting of PCM within the graphite pore will be investigated in presence of a void and including thermocapillary effects.

3.9 Boundary Conditions and the Marangoni Number

Upon including thermocapillary effects, a new term appears in the boundary conditions of the current phase change problem. In fact, the governing equations (equations 3.2–3.4) and the no-slip boundary condition applied to the walls of the pore remain unchanged. However, a boundary condition is applied to the liquid-gas interface as the continuity of the tangential shear stress in the form of:

$$\tau_{ij} = \mu\left(\frac{\partial U_i}{\partial X_j} + \frac{\partial U_j}{\partial X_i}\right) = \frac{\partial \sigma}{\partial \boldsymbol{N_t}} = \left(\frac{\partial \sigma}{\partial T}\right)\frac{\partial T}{\partial \boldsymbol{N_t}} \ , \tag{3.5}$$

which using the assigned dimensionless variables can be written in non-dimensional form as:

$$\left(\frac{\partial u_i}{\partial x_j} + \frac{\partial u_j}{\partial x_i}\right) = \underbrace{\left(\frac{d\,(\frac{\partial \sigma}{\partial T})(T_h - T_c)}{\mu\,\alpha}\right)}_{Ma}\frac{\partial \theta}{\partial \boldsymbol{n_t}} \ , \tag{3.6}$$

in which the non-dimensional group appearing on the right side of equation 3.6 is the Marangoni (Ma) number, representing the ratio of thermocapillary to viscous forces. The Marangoni number is proportional to the gradient of the surface tension with respect to temperature, $\frac{\partial \sigma}{\partial T}$. Since surface tension is a function of temperature (as shown in figure 3.11), upon observing a

temperature gradient along the interface, the Marangoni convection is present and should be included.

Applying the described boundary conditions, the whole set of equations were solved numerically using the combination of the VOF and enthalpy-porosity methods to extract the transient process of phase change within the pore in presence of void. In order to investigate the effect of the Marangoni convection, the phase change processes were simulated with and without considering thermocapillary effects (i.e. the variation of the surface tension with temperature). Thus, comparing the final states of solidification in these cases elucidates the effect and importance of the Marangoni convection.

3.10 Results of Phase Change Including Thermocapillary Effects

The results of the solidification and melting of PCM at the pore level in presence of a void within the pore including the thermocapillary effects will be discussed in this section. The simulation was carried out using Fluent 13.0 (2010). Parallel processing was used employing 4 CPU-cores for the numerical solution of the governing equations (combination of the VOF and enthalpy-porosity methods) over the domain with about 35,000 grids. However, due to the large number of equations (for both the VOF and solidification models), the stability of the numerical solution is relatively low and it is necessary to use a small time step size of 1 μs to enhance the tracking of both VOF and phase change interfaces. Therefore, a great number of time steps are necessary to simulate the entire solidification process, which makes this simulation prolonged even though parallel processing is utilized. The low thermal conductivity of the PCM, especially in the liquid phase, intensifies this problem and makes the simulation extremely time-consuming. In order to overcome this issue, thermophysical properties of PCM were set (Yaws, 2008 and Silva et al., 2009), except for the thermal conductivity that was set to 1 W/m K (instead of actual

thermal conductivity of about 0.13 W/m K) to expedite the simulation and reduce the required computational time. Unlike the previous simulations, the thermal conductivity of 5 W/m K was not used in order not to suppress the natural convection (due to drastic change in Rayleigh number) and observe the role of natural and Marangoni convections during the phase change. The corresponding Marangoni (Ma), Rayleigh (Ra) and Stefan (Ste) numbers associated with the present model are 500, 10 and 0.4, respectively.

Simulation of the solidification process was performed according to the described method to obtain the details for two cases with and without considering the thermocapillary effects. Comparison of these cases might highlight the effect of the Marangoni convection on the interface shape and position, as well as the amount and distribution of the shrinkage void. The time-dependent liquid fraction contours during the solidification process (described as Ma=500, Ra=10 and Ste=0.4) are given in figure 3.12. The black line identifies the void portion (air bubble), which is initially present in the pore at the conclusion of the infiltration process and remains as a gas experiencing no phase change (corresponding to solidification liquid fraction, ε, of 1.0).

Applying the lower temperature, T_c, as the boundary condition on the walls, the liquid next to the walls freezes at early time instants, and solidification continues toward the center of the pore. The final status of solidification after freezing the PCM content of the pore is given in figure 3.13 for two cases of solidification with and without considering the thermocapillary effects. As it is observed from figure 3.13, the final position of the void content of the pore after freezing is slightly different between the two cases. This difference, in fact, originates from the convection patterns within the pore during the solidification.

In the absence of the thermocapillary effects, convection within the pore is buoyancy-driven (natural convection). However, in presence of thermocapillary effects, convection is driven by thermally-induced surface tension forces (i.e. the Marangoni effect) that play a significant role in the pore scale. The convection patterns within the pore are presented in figure 3.14 for the two cases corresponding to excluding and including the thermocapillary effects during solidification. As observed in figure 3.14a, there is a single clockwise-rotating buoyancy-driven vortex within the pore when the thermocapillary effects are ignored. However, including the thermocapillary effects will change this pattern to a vortex pair as shown in figure 3.14b.

In fact, the importance of the gravitational effects can be contrasted against the surface tension effects using the Bond number (Bo) as the dimensionless ratio of the gravitational to surface tension forces. For this problem, Bo= 0.05 indicates that the surface tension is the dominant force as it thoroughly affects/controls the convection pattern within the pore. To highlight more details, the convection patterns near the liquid-gas interface in the pore are compared in figure 3.15 at a selected time instant between two cases of solidification with and without Marangoni effects. The difference in the convection patterns is responsible for the final shape of the voids and can be easily observed by comparing figure 3.15a and b.

The described phase change model is capable of predicting the shrinkage void due to the PCM contraction during freezing. This was also studied and verified for the case of water (with expansion during the freezing process), as presented in Appendix B. In both cases of solidification (with and without Marangoni effect), the void content after freezing turned out to be around 11.1% by area, which in comparison with 9.8% initial void from infiltration process, yields a 1.3% shrinkage void due to solidification. Moreover, the time duration for solidification (as shown in figure 3.13) is longer when thermocapillary effects are ignored. The reason for such

behavior is linked to the convection patterns within the pore. When thermocapillary effects are neglected, there is a single clockwise buoyancy-driven vortex in the pore. Whereas, when the Marangoni convection is included, there is a pair of surface tension-driven vortices supplying the hot liquid within the pore to the middle region of the liquid-gas interface as presented in figure 3.14. The void (air) with different thermophysical properties and a very low thermal conductivity is not able to absorb heat from the supplied liquid and acts more as a thermal barrier. As a result, the simultaneous presence of the void and Marangoni convection within the pore affects the solidification rate as well as the position and distribution of the infiltration and shrinkage voids. For the case considered in this work, the duration of freezing process is shortened from 85.8 ms in the absence of thermocapillary effects to 79.4 ms (about 8%) in presence of thermocapillary effects as shown in figure 3.13.

Using the same method and applying the melting boundary conditions on the walls of the pore, the simulation of melting was conducted for two cases of excluding and including thermocapillary effects. The melting process initiates from the end of the solidification process (when the whole PCM within the pore is frozen) and continues until the entire PCM within the pore melts. A comparison of the solidification and melting times among different cases is presented in table 3.1 to elucidate the effect of the void and Marangoni convection on phase change processes at the pore level.

3.11 Verification of the Results

The verification and validation of the infiltration process and infiltration void (9.8% in this study) was investigated and reported in chapter 2. For verification purposes, the volume of predicted shrinkage void can be compared to the theoretical volume change during the solidification. Based on the numerical values of density (779 kg/m^3 for liquid phase and 790

kg/m^3 for solid phase, as shown in figure 3.1), the theoretical amount of volume shrinkage can be obtained based on the amount of density increase during the phase change from liquid to solid. For the present model, the theoretical amount of shrinkage void was obtained to be 1.39%. Based on the numerical simulations of the solidification process, the volume of the shrinkage void turned out to be 1.3% which is in good agreement with the theoretical volume change of 1.39% (6.9% discrepancy). The discrepancy is mainly related to the estimation of the position of the interface within the VOF model. In fact, the volume fraction in the VOF method is a step-function changing from 1 to 0 at the interface, which brings a level of estimation in tracking the exact position of the interface and estimation of the volume of the voids. Furthermore, the prediction of volume change during the phase change was verified for a classical problem of freezing of water in a square cavity in the absence of interfacial forces and with expansion of water during the freezing. The obtained results of volume change of water during freezing was found to be in good agreement with the theoretical volume change and presented in Appendix B.

Since the main purpose of this chapter was studying the effect of void on phase change of PCM at the pore level, the convection patterns within the pore and phase change details such as duration of phase change were studied for solidification and melting of PCM within the pore. One factor that might affect the numerical results is the movement (sinking or floating) of the solid phase during the melting process when the solid is not connected to any wall or interface. In general, by setting the mushy zone constant (A_{mz}) as a big number in simulation of phase change, the velocity components for the cells containing the solid phase diminish to zero. Although this can be partially controlled with changing the value of the mushy zone constant, it can cause deviations in phase change duration due to the possibility of sinking/floating of the solid phase because of a higher/lower density compared to the liquid phase. To address this

effect, the time scale of the motion of the solid phase should be compared against the time scale of melting. If the motion of the solid phase during the melting occurs faster than the melting process, the solid phase will sink/float before melting. This causes the solid phase to be closer to the boundaries and affects the melting rate of the solid. Therefore, it affects the duration of melting process and causes a deviation between the actual melting time and the predicted melting time. As a result, such time scales were compared for the case of the pore-level melting of cyclohexane in this study. The time needed for a piece of solid cyclohexane to sink in the liquid phase can be obtained from:

$$t = \left(\frac{2l}{(1-\rho_{liquid}/\rho_{solid})g} \right)^{1/2}, \qquad (3.7)$$

in which l is the distance to sink or float. For the case of melting of cyclohexane within the pore, considering the sinking distance of $d/2=200\mu m$, and using the density values according to figure 3.1, the sinking time of 54.1 ms will be obtained, which is greater than the melting times of 8 and 38 ms for the cases of K=5 W/m.K and K=1 W/m.K, respectively (from the moment that solid is not connected to walls or interface to the end of melting process). As a result, sinking of the solid phase for the studied cases cannot produce significant deviations in the predictions of phase change duration.

3.12 Summary

Numerical simulation of the phase change processes was performed using a multiphase approach and based on the combination of the VOF and the enthalpy-porosity methods. For the studied case, both infiltration and solidification processes contribute to the formation of voids, distinguished as the ‘infiltration void’ and ‘shrinkage void’. The infiltration process was

simulated first (chapter 2), and its final state was used as the initial state of the solidification process. Therefore, the effect of the infiltration void on the solidification process was included by utilizing the described numerical approach. Moreover, the proposed model is capable of predicting the volume changes (contraction or expansion) during the phase change processes by taking into account the variation of density between liquid and solid phases.

The simulations were conducted for a two-dimensional model of the graphite pore and the details of the phase change process were extracted along with the volume of the shrinkage void, which is in agreement with the theoretical results of volume change. Since the simulation is time-dependent, the temporal evolution of shrinkage void was studied which led to prediction of the distribution of the shrinkage void within the pore. Furthermore, a temperature gradient was observed along the PCM/void interface during the phase change processes within the pore.

Upon observing a temperature gradient in the liquid/gas interface within the pore, the effect of the Marangoni convection on the solidification process in presence of the void was investigated at the pore level. The presence of the void (from infiltration) within the pores can affect the phase change processes through triggering thermocapillary effects along the liquid-gas interface and Marangoni convection. The effect of the Marangoni convection on phase change processes were studied numerically using the combination of the VOF and enthalpy-porosity methods. The variations of the liquid density and surface tension with temperature were included to enable volume change as well as thermocapillary effects during the phase change. The time-dependent simulations were performed for solidification with and without thermocapillary effects. The final status of phase change processes, position and shape of voids, shrinkage void formation and amount, convection patterns within the pore and phase change time (duration) were extracted and compared between cases with and without thermocapillary convection.

It was found that thermocapillary forces are strong enough to overcome gravitational forces and influence the convection pattern within the pore. This led to a significant change in the convection pattern as well as phase change time (about 8% reduction due to thermocapillary convection in the present work, see table 3.1). Furthermore, verification of the results was conducted by comparing the volume of the shrinkage void with the theoretical volume change during the freezing.

Table 3.1 Comparison of the phase change duration among different cases of solidification and melting of PCM within the pore

Phase change model	No void	Presence of void excluding Marangoni effects	Presence of void including Marangoni effects
Solidification† K=5 W/m.K	15.2	18.1	16.8
Melting *† K=5 W/m.K	14.8	17.2	15.9
Solidification† K=1 W/m.K	76.0	85.8	79.4
Melting *† K=1 W/m.K	72.0	81.0	75.1

† Time durations in ms.

* For each case, the melting process initiates upon the completion of the solidification process.

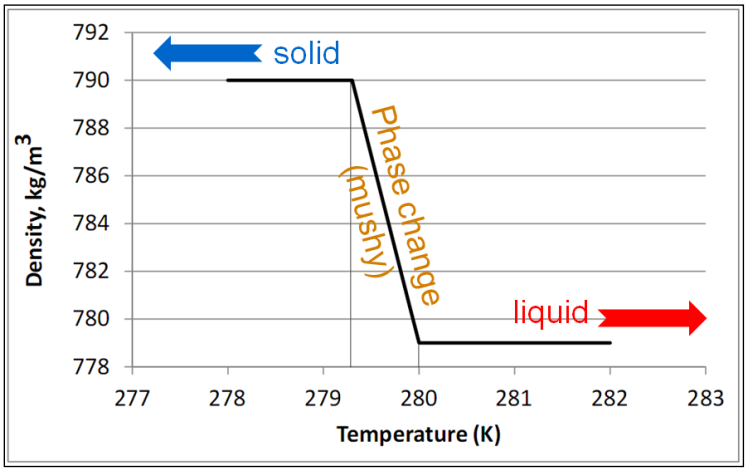

Figure 3.1 Density of PCM (cyclohexane) as a function of temperature for solid (T < 279.3 K), liquid (T > 280 K) and mushy zone (279.3 K < T < 280 K), corresponding to the liquidus and solidus temperatures of 280 K and 279.3 K, respectively.

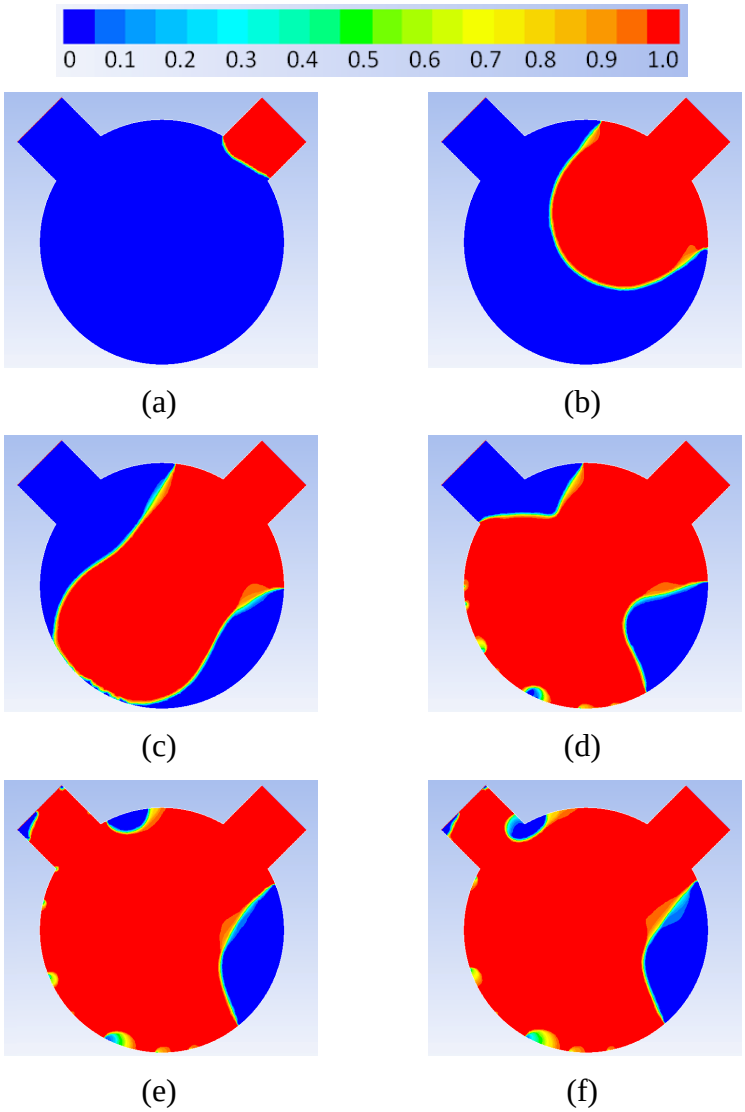

Figure 3.2 Evolving VOF volume fraction distribution (λ) during the infiltration of PCM into the pore at time instants of (a) 0.5, (b) 1.2, (c) 1.56, (d) 1.75, (e) 2.1, and (f) 2.5 ms.

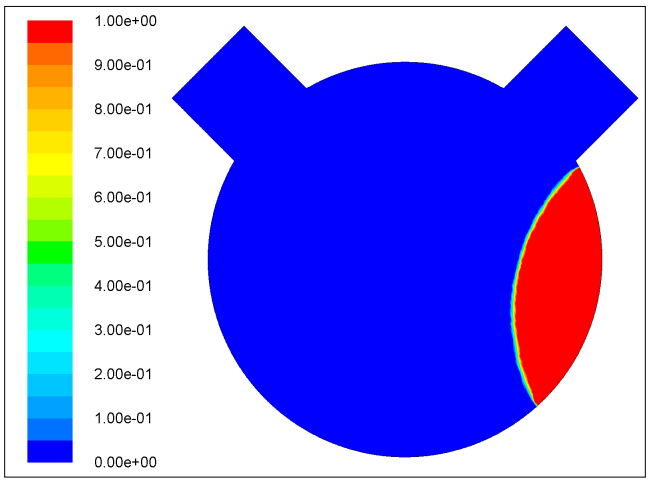

Figure 3.3 Final state of infiltration and position of the infiltration void (red region).

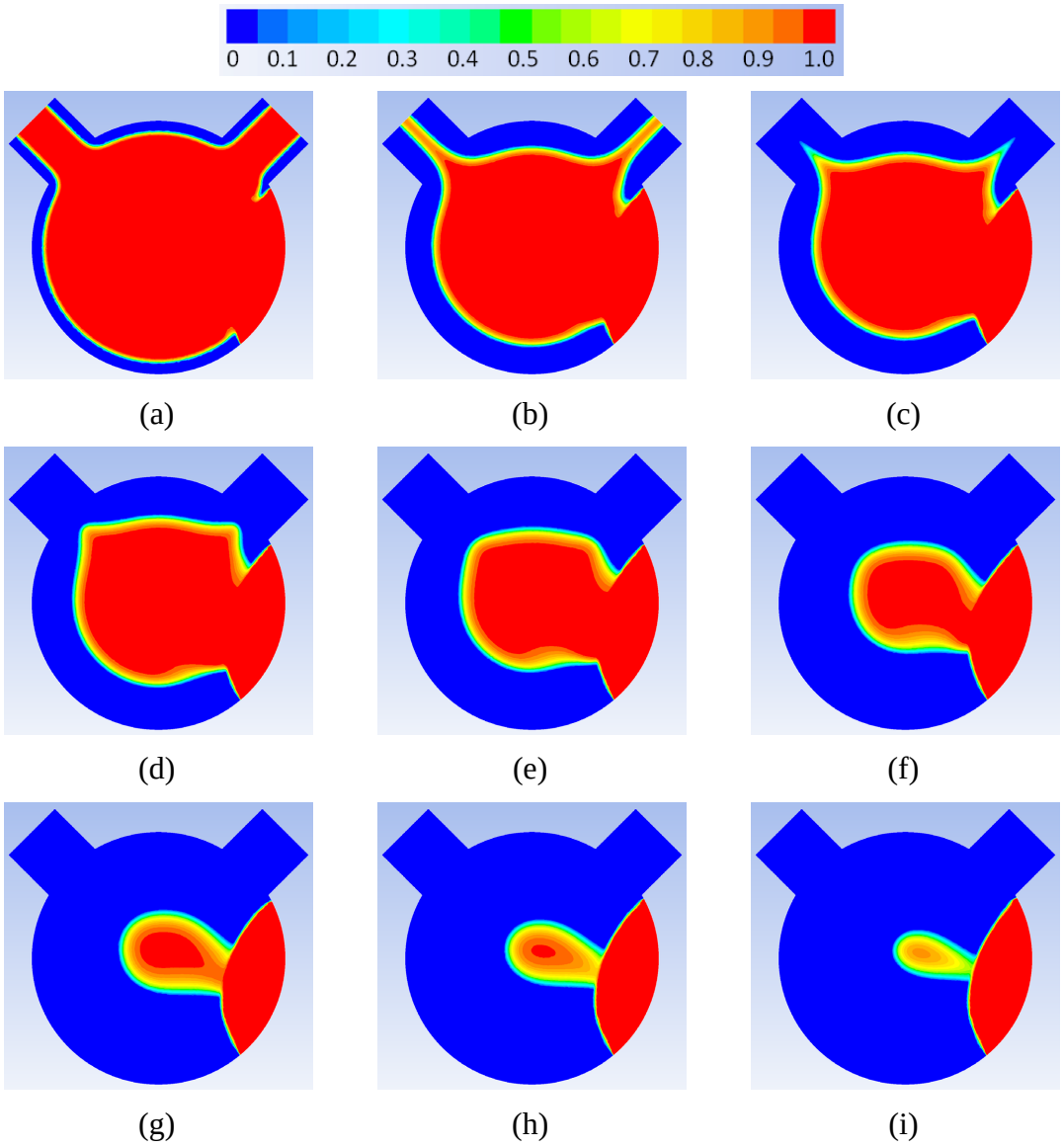

Figure 3.4 Evolving liquid fraction distribution (ε) during the solidification of PCM within the pore at time instants of (a) 0.25, (b) 1.35, (c) 2, (d) 3, (e) 5, (f) 8, (g) 11, (h) 13 and (i) 15 ms (solid is in blue while liquid PCM and air both are in red).

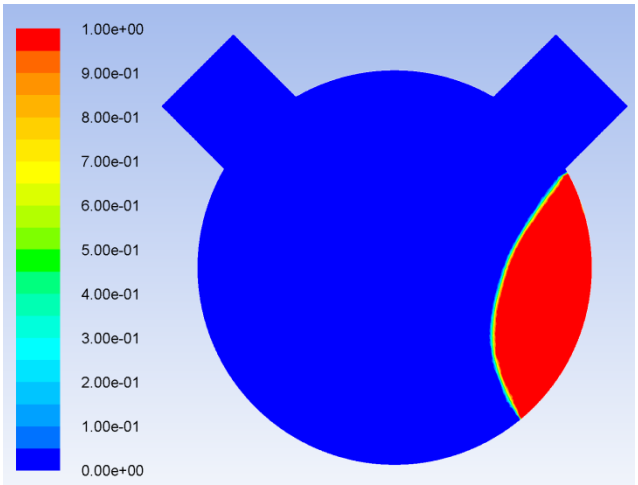

Figure 3.5 Final state of solidification and position of the void within the pore after t=18.1 ms (liquid PCM is entirely frozen into solid which is in blue while air/void is in red).

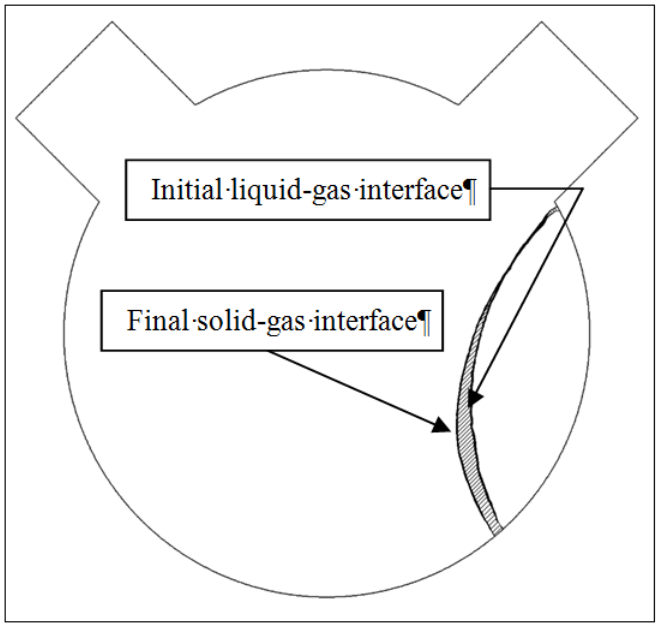

Figure 3.6 Initial liquid-gas interface (before solidification) versus final solid-gas interface (after solidification) and shrinkage void distribution within the pore (shaded area).

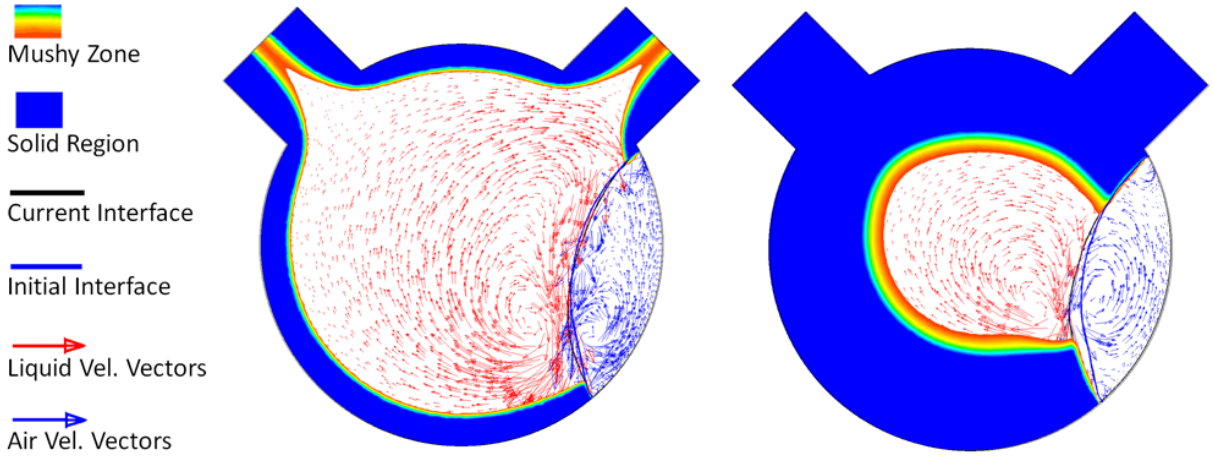

(a)
t = 2 ms
V_{max} = 0.36 m/s

(b)
t = 8 ms
V_{max} = 0.25 m/s

Figure 3.7 Natural convection patterns during the solidification of PCM within the pore in presence of void and its role in the emergence of the shrinkage void.

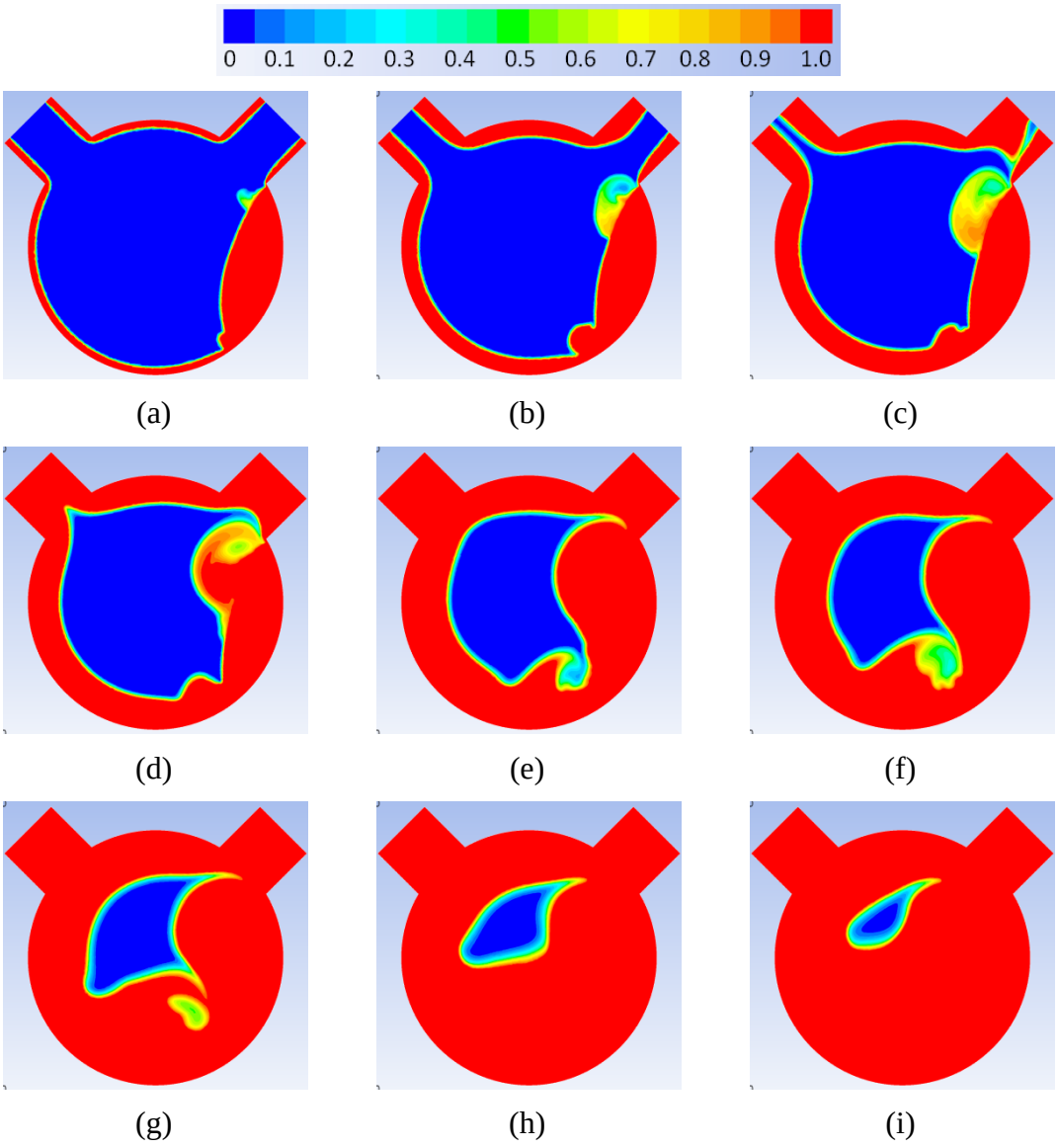

Figure 3.8 Evolving liquid fraction distribution (ε) during melting of PCM within the pore at time instants of (a) 0.25, (b) 1.2, (c) 2.4, (d) 3.8, (e) 7, (f) 8.5, (g) 10.5, (h) 13 and (i) 16 ms (solid is in blue while liquid PCM and air both are in red).

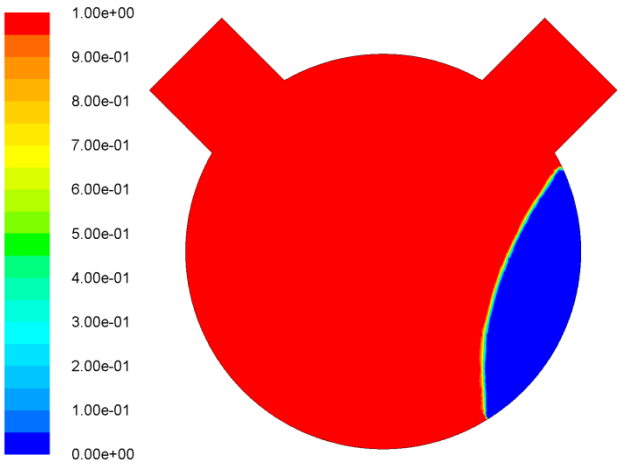

Figure 3.9 Final status of the melting process and the position and shape of the void within the pore (9.8% by area indicating disappearance of the shrinkage void).

(a)

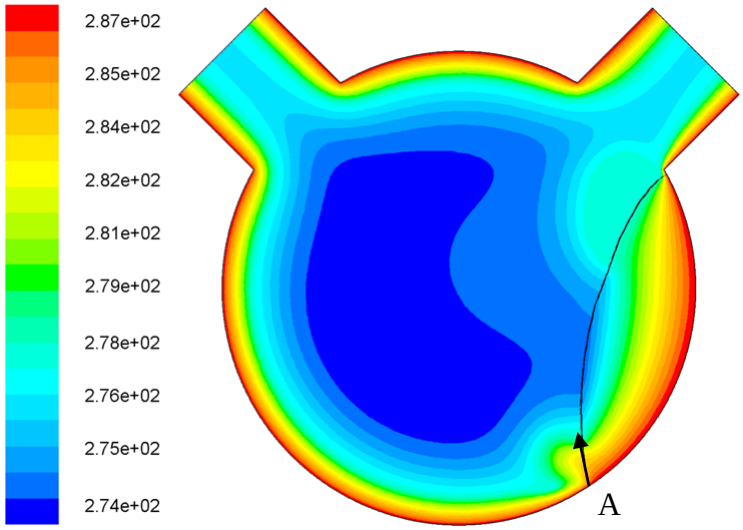

(b)

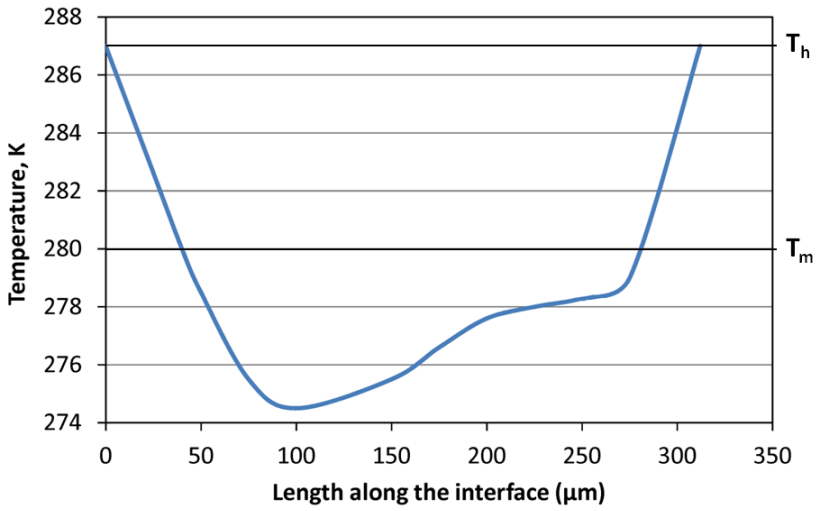

Figure 3.10 (a) Observed temperature gradient along the PCM/void interface during the melting of PCM within the pore at time instant of 1.25 ms, and (b) Instantaneous temperature variation along the PCM/void interface at t=1.25 ms (the length along the interface was measured from point A, shown in figure 3.10a).

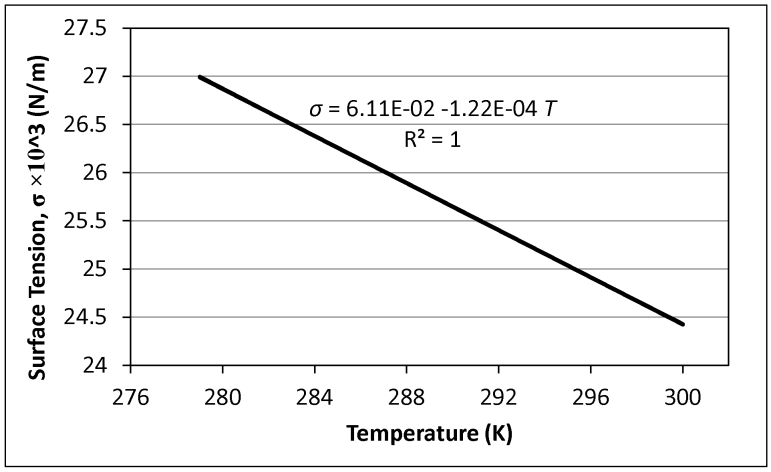

Figure 3.11 Variation of the surface tension of PCM (cyclohexane) with the temperature based on data of Yaws (2008).

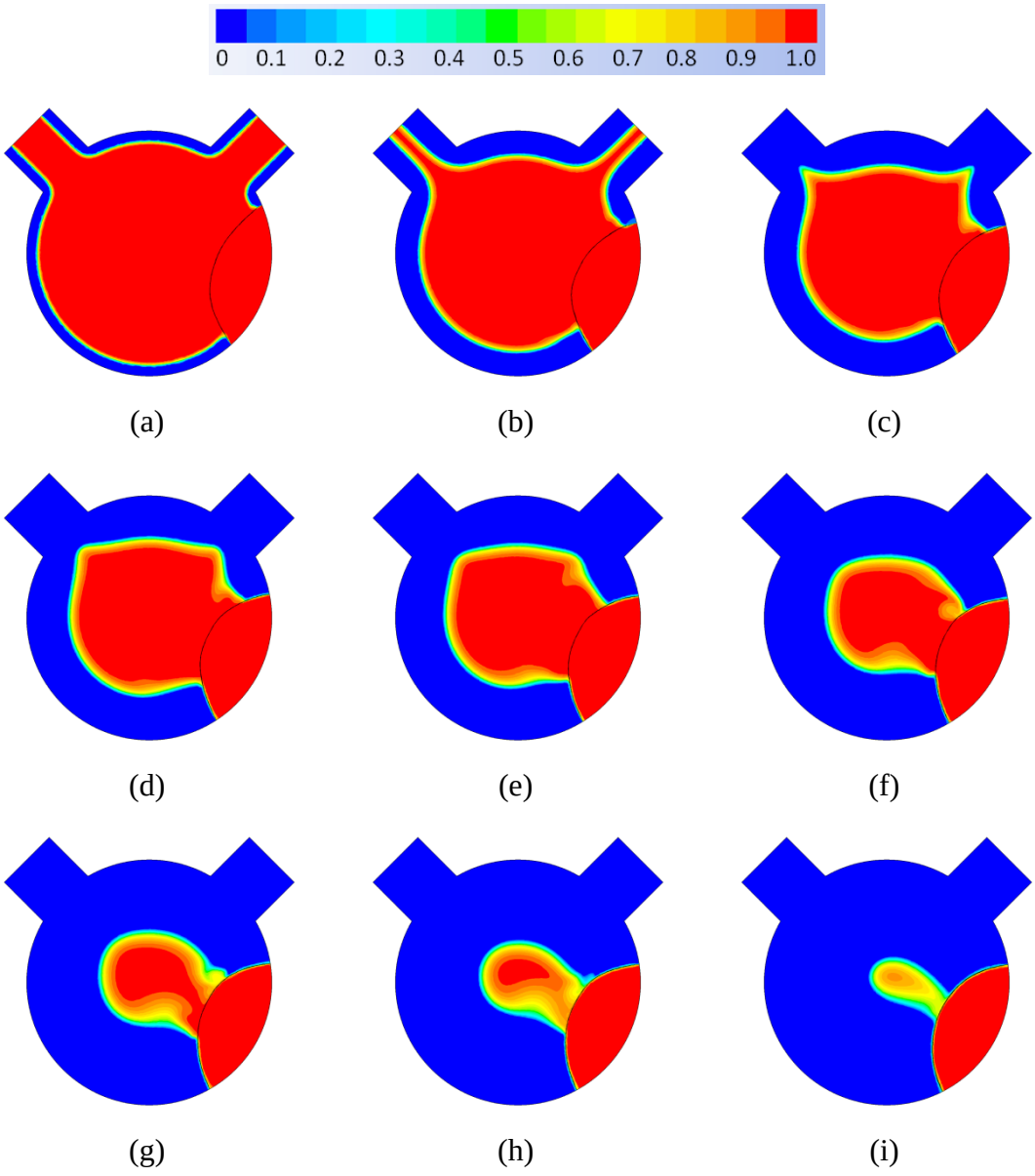

Figure 3.12 Contours of the solidification liquid fraction (ε) at time instants of (a) 1, (b) 5, (c) 10, (d) 15, (e) 20, (f) 30, (g) 40, (h) 50 and (i) 65 ms (solid is in blue while liquid and air are in red and the black line shows the PCM-void interface).

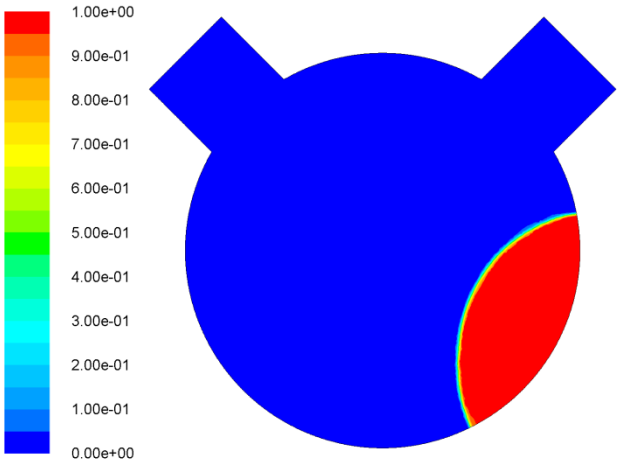

(a) t = 85.8 ms, Void content (by area) ≈ 11.1%
(including 9.8% infiltration void and 1.3% shrinkage void)

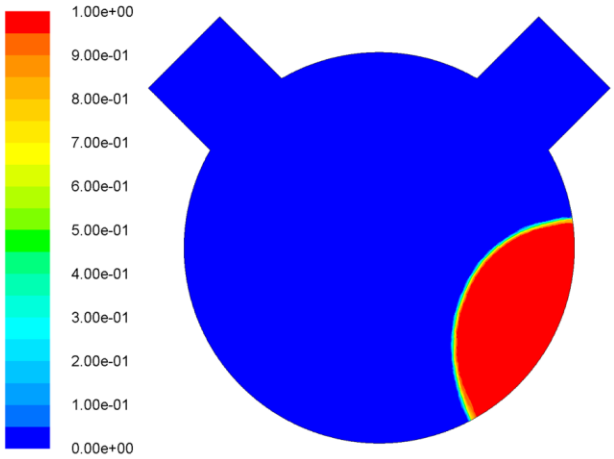

(b) t = 79.4 ms, Void content (by area) ≈ 11.1%
(including 9.8% infiltration void and 1.3% shrinkage void)

Figure 3.13 Final status of solidification and position of the void corresponding to (a) exclusion, and (b) inclusion of the thermocapillary effects (frozen PCM is in blue while void is in red).

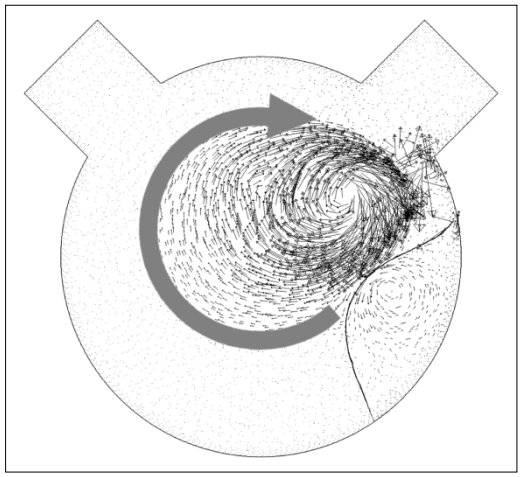

(a) Single buoyancy-driven clockwise vortex within the pore (no Marangoni effect), V_{max}=0.092 m/s

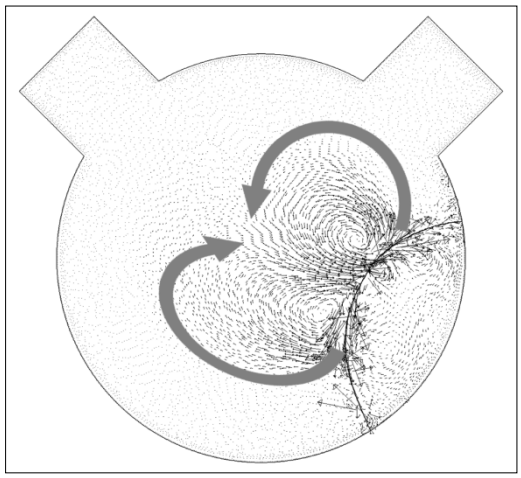

(b) Pair of surface tension-driven vortices within the pore (including Marangoni effects), V_{max}=0.137 m/s

Figure 3.14 Velocity vectors showing the convection patterns within the pore at a selected time instant of t = 18 ms for two cases of (a) excluding, and (b) including thermocapillary effects in solidification (black line shows the liquid-gas interface). Different scales were used in presenting the velocity vectors for better visualization.

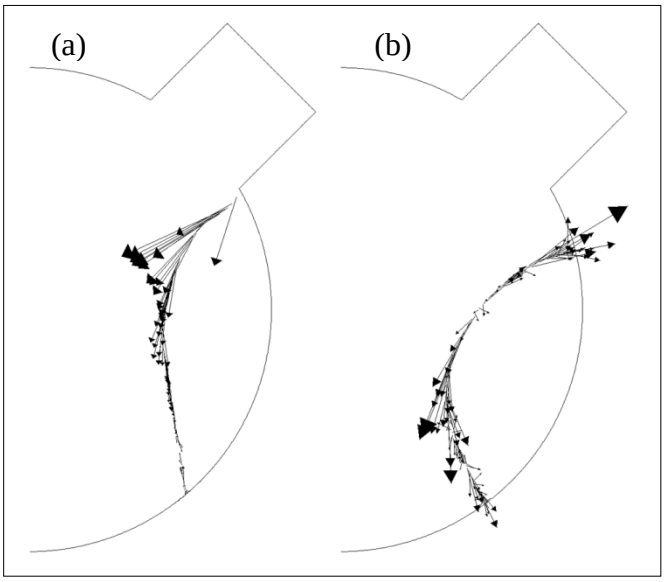

Figure 3.15 Velocity vectors depicting the convection pattern near the liquid-gas interface at t=6 ms for two cases of (a) excluding, and (b) including the Marangoni effects in solidification.

Chapter 4 Thermal Conductivity Improvement of Thermal Energy Storage Composites

Development and utilization of thermal energy storage (TES) systems were studied by investigating infiltration and phase change processes in chapters 2 and 3 and pertinent phenomena including void formation, volume change during phase change and thermocapillary effects were addressed. The main purpose of developing TES composites is to infiltrate phase change materials (PCM) into highly conductive porous structures and achieve a relatively high effective thermal conductivity. Thus, in this chapter, thermal conductivity improvement will be investigated numerically and experimentally for TES composites.

4.1 Introduction

Phase change materials are widely utilized in latent heat TES systems due to their considerable heat of fusion (Farid et al., 2004 and Oro et al., 2012). Although sizeable amounts of energy per unit mass can be stored in PCM for later use, low thermal conductivity of PCM deteriorates their thermal performance by limiting the achievable heat flux and elongating the phase change processes corresponding to charge and discharge of energy, i.e. melting and solidification processes (Jegadheeswaran and Pohekar, 2009). Several methods have been used to improve the thermal conductivity of PCM. These methods mainly involve introducing a highly-conductive solid phase into PCM in order to enhance the overall thermal conductivity of the resulting system.

Among different proposed methods, utilization of highly-conductive porous structures has been studied and found to cause noticeable improvement in thermal behavior of the resulting

TES system. Different studies reported a sharp increase in the rates of energy exchange (equivalent to heat flux) during the solidification and melting of PCM in TES composites. Other studies also reported a considerable decrease in duration of solidification and melting of PCM in TES composites compared to pure PCM case. Such enhancements in thermal behavior of PCM in TES systems is attributed to the high thermal conductivity of the porous structure and the high ratio of heat transfer surface to volume in TES composites (Coussy, 2010). These factors are among the most important factors in heat transfer engineering and make highly-conductive porous structures such as graphite and metal foams extremely desirable for TES applications. For instance, graphite foam, with a highly-conductive and highly-porous structure, is an excellent candidate for infiltrating PCM into its pores and forming TES composites with improved effective thermal conductivity. Therefore, thermal conductivity improvement of TES composites (consisting of PCM infiltrated in graphite foam) is studied in this chapter due to its importance in design and application of TES systems.

For this purpose, the effective thermal conductivity of composites of graphite foam impregnated with PCM is investigated numerically and experimentally. For numerical simulation, the graphite structure was modeled as a three-dimensional body-centered cube arrangement of uniform spherical pores, saturated with PCM (based on the outcomes of chapter 2) and forming a cubic representative elementary volume (REV). Thermal analysis of unidirectional heat transfer through the REV was conducted and the total heat flux was determined. This leads to evaluation of the effective thermal conductivity based on the Fourier's law.

For experimental verification, a sample of graphite foam was infiltrated with PCM. The effective thermal conductivity was evaluated using the direct (or absolute) method of measuring

temperature within the sample under fixed heat flux in unidirectional heat transfer. Upon measuring the temperature, the temperature gradient within the composite sample is extracted based on dimensions of the sample and positions of the thermocouples. Knowing the applied heat flux and the temperature gradient within the sample, the Fourier's law can be applied to extract the effective thermal conductivity of the composite sample.

The numerical and experimental results indicate a noticeable improvement in the effective thermal conductivity of composites compared to the PCM. The numerical and experimental results are in good agreement and are also consistent with the reported experimental results on graphite foam using other methods (laser flash technique). Moreover, the role of natural convection within the pores is studied and found to be negligible. The results of the present study were published in Moeini Sedeh and Khodadadi (2013B).

4.2 Literature Review

In order to improve the low thermal conductivity of PCM in TES and thermal management applications (i.e. increasing the achievable heat flux and decreasing the duration of phase change processes corresponding to charge and discharge of energy), different methods have been proposed. These methods introduce highly-conductive inserts in different forms, shapes and materials including fixed/stationary structures as well as suspended additives (Jegadheeswaran and Pohekar, 2009; Fan and Khodadadi, 2011, Oro et al., 2012).

For instance, Zhang and Faghri (1996) studied heat transfer enhancement in the latent heat TES systems using an internally-finned tube for PCM in an annular shell space around the finned tube and heat transfer fluid flowing within the finned tube. They considered a transient two-dimensional heat transfer model featuring heat conduction in the internal fins and melting of PCM due to heat transfer from the transfer fluid. They solved the governing equations

numerically using the finite difference method. Their results indicated that for fluids with low thermal conductivity, adding internal fins is an efficient way to enhance heat transfer in thermal energy storage systems.

Melting of paraffin wax was explored numerically by Shatikian et al. (2005) using transient three- and two-dimensional models of a cubic heat storage unit with internal fins under heating from below conditions. They performed a parametric study on the fin thickness with a constant ratio of the PCM layer to fin thickness. Their results show that the liquid fraction during melting of PCM depends on the temperature difference between the base and the mean melting temperature and also on the thickness of the fins. They reported an increase in heat flux and liquid fraction with decreasing the thickness of the PCM layer that means decreasing the thickness of the fin (down to 0.3 mm in this study) and increasing the number of fins per unit length of the heat storage unit.

Tong et al (1996) demonstrated the enhancement of the heat transfer rate during melting and freezing of PCM due to insertion of a high-porosity metal matrix. The model was selected as a vertical annulus homogeneously filled with water and an aluminum matrix. The Navier-Stokes equations were modified to account for Darcy's effect and the density inversion phenomenon of water is considered for phase change processes. Their numerical results indicated that the heat transfer rates for enhanced cases show an order-of-magnitude increase over the base case, where no metal matrix is inserted.

Mesalhy et al. (2006) performed numerical and experimental studies to investigate the thermal characteristics of composites of carbon foam saturated with PCM. For experimental studies, they inserted the composite into a cylindrical enclosure under heating from above conditions. For numerical simulation, they used the finite volume technique to discretize the

volume-averaged heat diffusion equation and employed the enthalpy-porosity method for modeling the phase change process. Their numerical and experimental results showed that the porosity and thermal conductivity of carbon foam play important roles in thermal performance and heat absorption rate of the resulting composite.

Different studies (Zhong et al., 2010; Wang et al., 2011) on application of porous structures of graphite impregnated with PCM for thermal energy storage (TES) revealed that highly-porous and highly-conductive structures have a significant potential to improve the effective thermal conductivity and increase the solidification and melting rates of PCM. In fact, high porosity leads to high ratios of area to volume which is desirable in heat transfer applications and TES composites. Consequently, different carbon and graphite structures were investigated for heat transfer and TES applications. For instance, thermal storage composites of paraffin and expanded graphite were studied by Py et al. (2001), Mills et al. (2006), Sari and Karaipekli (2007) and Xia et al. (2010). They reported noticeable improvements in thermal conductivity of the resulting composites, as well as a decrease in the overall solidification/melting time of paraffin.

The effect of carbon fiber brushes on improving the thermal conductivity of PCM (n-octadecane) packed around heat transfer tubes was studied by Fukai et al. (2002). They found an improvement in the measured transient thermal responses in composites as the volume fraction of the fibers and brush diameter increased. However, due to thermal resistance between the fibers and tube surfaces, there is a critical diameter above which no further improvement is expected.

Thermal behavior of PCM composites with carbon nanofibers and carbon nanotubes were explored experimentally by Cui et al. (2011). They found that the thermal conductivity of PCM composites increases with the loading of carbon nanotubes or carbon nanofibers. Moreover,

carbon nanofibers were found to be more effective in improving the thermal conductivity of the PCM.

Mesalhy et al. (2005) investigated heat transfer and melting rate of the PCM in combination with a porous matrix utilized for thermal conductivity improvement. They reported that using a high porosity and high thermal conductivity porous solid is the best technique for thermal conductivity and heat transfer improvement.

Development of high thermal conductivity, mesophase-pitch-derived carbon/graphite foams by Klett et al. (2000) and recent advancements (Yadav et al., 2011) opened a new horizon to TES and thermal management applications. After foaming and graphitization techniques, the resulting graphite foams have densities ranging from 200 to 600 kg/m^3, and the bulk thermal conductivities varied correspondingly with density from 40 to 150 W/m.K which makes them desirable for TES applications. Having a porous structure with a high porosity provides a high ratio of surface area to volume and is another advantage of graphite foams, making them suitable for TES applications.

Cabeza et al. (2002) compared three methods of heat transfer improvement (i.e. adding stainless steel pieces, adding copper pieces and using porous graphite impregnated with PCM) in a TES system containing deionized water as the PCM. Conducting similar freezing and melting experiments, they found that adding stainless steel pieces to the PCM does not increase the heat flux noticeably and consequently does not change the freezing/melting front. On the other hand, adding copper pieces increased the heat flux significantly and influenced the freezing/melting time favorably. Hence, using porous graphite leads to an even more increase in heat flux and decrease in freezing/melting time when compared to the case of using copper pieces.

In relation to experimental measurements, Gaies and Faber (2002) measured thermal diffusivity of graphite foam samples for different relative densities and at different temperatures using the laser flash technique. They evaluated thermal conductivity of graphite foams using the heat capacity values of bulk polycrystalline graphite and observed that thermal conductivity of graphite samples, including as-processed and chemical vapor infiltrated (CVI) foams, decreases with increasing temperature or decreasing density.

Moreover, Zhong et al. (2010) characterized the thermal performance of paraffin wax (as the PCM)/graphite foam composites using experimental measurements of thermal diffusivity and latent heat. Using the laser flash technique for measuring thermal diffusivity, their experimental results indicated noticeable improvements in thermal diffusivity of the composite compared to that of pure PCM, especially with lower porosity of the foam. Using the differential scanning calorimeter technique for measuring the latent heat, they found that higher porosities of graphite foam leads to a lower decrease in latent heat.

Considering numerical simulations of the pertinent materials, Lafdi et al. (2008) investigated the thermal performance of graphite foam infiltrated with PCM computationally. They treated the graphite foam/PCM composite as a porous medium and solved the volume-averaged equations of mass, momentum and energy conservation numerically for melting of the PCM. In effect, the geometrical details of the graphite foam were not resolved. They compared the energy absorption rate for graphite/PCM composite with that of pure PCM and found a significant improvement in the energy absorption rate (e.g. output power).

Furthermore, Yu et al. (2006) considered a unit cube model for graphite foam based on interconnected sphere-centered cubes. Simplifying this pore-level geometry into a solid square bar structure with the same porosity, neglecting convection of the fluid within the pores,

neglecting radiation and assuming local thermal equilibrium between solid and fluid phases at the pore level, they derived an expression for the effective thermal conductivity based on the geometric features of the unit cell. The results of this model exhibited good agreement with the thermal conductivity data of Klett et al. (2004).

In a recent study, DeGroot and Straatman (2012) conducted a direct simulation on this model by defining permeability (using the Darcy's law as well as a non-Darcy term) in the volume-averaged momentum equation and thermal dispersion conductivity tensor in the volume-averaged energy equation to improve the model predictions and extracting relevant effective properties of graphite foams (i.e. effective permeability, thermal dispersion conductivity, convective velocity and interfacial Nusselt number).

Considering engineering applications of TES composites, several studies were performed on utilization of graphite foams for performance improvement of evaporators (Coursey et al., 2005; Jin et al., 2011A), heat exchangers (Yu et al., 2006; Tuzovskaya et al., 2012; Lin et al., 2013), and thermal management of electronics (Williams and Roux, 2006; Gandikota and Fleischer, 2009). These studies highlighted major improvements in the thermal performance of the aforementioned thermal components. Further studies were conducted on the effect of graphite foams on convective heat transfer improvement (Sultan et al., 2009; Leong et al., 2010) and promotion of pool boiling (Jin et al., 2011B), confirming heat transfer increase due to utilization of graphite foams. In a theoretical study of the effective thermal conductivity of graphite foam, a unit cell model was developed to represent the microstructure of graphite foam with the same surface area to volume ratio of the foam (Leong et al., 2011). The obtained results are in agreement with previous findings of Klett et al. (2004).

Considering the above-reviewed papers, it can be concluded that utilizing highly-porous, highly-conductive graphite and carbon foams is one of the most effective methods of improving thermal conductivity and heat transfer. Advantages of having high thermal conductivity (higher than conductive metals), enabling high ratios of heat transfer surface to volume (due to high porosity), and having low densities make graphite/carbon foams ideal candidates for enhancing thermal conductivity of PCM and thermal performance of phase change processes. Previous papers generally focused on thermal performance improvement (mainly melting time, achievable heat flux, or rate of energy absorption). However, this chapter covers the thermal conductivity investigation of a TES composite consisting of graphite foam saturated with PCM in pores since most of PCM are wetting liquids with almost no void due to the infiltration, as investigated in chapter 2.

In this chapter, thermal conductivity of PCM/graphite foam composite is investigated numerically and experimentally. The numerical model was based on a representative elementary volume of the composite utilizing the three-dimensional (3D) body-centered cube (BCC) arrangement of spherical pores. This was followed by the thermal analysis for unidirectional heat transfer through the REV. The experiments were performed using the direct (or absolute) method of temperature measurement within a foam sample saturated with cyclohexane as a typical PCM, under fixed heat fluxes. The numerical and experimental results of this part are found to be in good agreement.

Prior to this effort, the bulk thermal conductivity of graphite foam was investigated by considering air as the working fluid within the pores of the graphite foam in the numerical model and also measured experimentally. The numerical and experimental results of this part were also in good agreement. Additionally, a good agreement with previous experimental work, using the

laser flash technique (Gaies and Faber, 2002), was realized. Having verified the effective thermal conductivity of the foam/PCM composite, the findings of this chapter provide new insight for design and development of TES systems and further numerical and experimental investigations of solidification and melting within TES composites.

4.3 Numerical Investigation of the Effective Thermal Conductivity

Numerical investigation of the effective thermal conductivity of graphite foam/PCM composite includes development of a 3D model, grid generation and grid independence study, governing equations, boundary conditions and numerical method of thermal analysis. The pertinent details are discussed in this section.

4.3.1 Modeling of the Graphite Foam/PCM Composite

A three-dimensional model of the graphite foam/PCM composite was developed based on the structure of the graphite foam, as shown in figure 4.1. The scanning electron microscopy (SEM) image of the pores reveals their nearly spherical geometry (figure 4.1a). Therefore, in the numerical model, the pore geometry was deemed to be spherical. According to figure 4.1 and based on in-house pore diameter measurements on the samples of graphite foam, the pores are not uniform in size. However, the average pore size and porosity was identified by the foam manufacturer (PocoFoam®, Poco Graphite Inc., Decatur, Texas) to be 400 microns and 75%, respectively (www.poco.com/Portals/0/Literature/Semiconductor/78962v2PocoFoamFlyer.pdf). Thus, a uniform pore diameter of 400 microns was considered in the numerical model. Furthermore, the BCC packing was considered for the arrangement of pores in graphite foam. According to previous work on modeling thermal transport in graphite foam (Alam et al., 2004; Leong et al., 2011; Moeini Sedeh and Khodadadi, 2012), porosity has an important effect on the

effective thermal conductivity of composites. Therefore, the porosity of the graphite foam in modeling was considered to be equal to the actual porosity of the foam, i.e. 75%. The porosity of the BCC arrangement of spheres, tangent to each other, is $\frac{\pi\sqrt{3}}{8} = 68.0175\%$.

Consequently, in modeling it is necessary to consider interference among neighboring spherical pores to increase the porosity to 75%, in order to match the porosity of graphite foam. The interference of the pores (spheres) generates lens-shape volumes as it can be observed in the structure of graphite foam in figure 4.1b. The pore volume in this case is calculated as the volume of two spheres (corresponding to the BCC structure) minus the volume of interferences (eight lens-shape volumes in the REV). Accordingly, the porosity is obtained by dividing the pore volume by the volume of the REV. Using the geometric relation between the REV length and the distance of spheres (as a function of sphere diameter and the interference), the corresponding REV length and the interference of the pores were calculated analytically to obtain the porosity of 75%. As a result, by setting the interference, a 3D arrangement of the BCC-based spheres with the porosity of 75% was developed as the REV for thermal analysis of the composite, and is shown in figure 4.2.

4.3.2 Grid Generation and Grid Independence Study

Modeling of the graphite foam/PCM composite was followed by grid generation and grid independence studies. Using unstructured tetrahedral grid systems, several grids were generated with different grid resolutions and number of cells (0.26 to 1.2 million). The material properties were set for graphite as the foam structure and cyclohexane as a typical hydrocarbon-based PCM (Yaws, 2008; Silva et al., 2009) and are given in table 4.1. Thermal analyses (including natural convection within the pores) were conducted for different grids under the same thermal boundary

condition of 300 K on the cold side and 301 K on the hot side, while the remaining four sides of the REV cell are insulated. The temperature at the center of the model (which is also the center of the middle-pore) and the heat flux on the hot side (which is equal to that of cold side after solution convergence) were monitored. The results were found to be grid-independent over grid systems having more than 750,000 tetrahedral cells as shown in Figure 4.3. However, the final grid selected for the numerical analyses had about 1.11 million cells. This is due to the extremely fine grid needed over conjugate heat transfer surfaces in order to couple them and enable heat transfer from one surface on solid foam to its pair in the fluid zone. The final grid is shown in Figure 4.4.

4.3.3 Governing Equations

Transport of momentum and heat is driven by applying a unidirectional temperature difference over the REV due to conduction in graphite foam and conduction/natural convection in the PCM within the pores. Natural convection is expected to be very weak within the pores due to the small pore diameter and temperature difference (the Grashof and Rayleigh numbers based on the pore diameter are of the order of 1 and 10, respectively for cyclohexane as the working liquid). However, in order to examine the role of natural convection within the pores, the continuity and momentum equations were discretized and solved numerically over the fluid domain. After inspecting the role of natural convection within the pores (which turned out to be negligible), only the thermal energy equation was solved numerically over the fluid and solid domains. The governing equations for the laminar flow in the fluid domain (liquid PCM within pores) in general Cartesian tensor form are (Anderson, 1995):

$$\frac{\partial \rho}{\partial t} + \frac{\partial}{\partial x_i}(\rho u_i) = 0 , \tag{4.1}$$

$$\frac{\partial}{\partial t}(\rho u_i) + \frac{\partial}{\partial x_j}(\rho u_i u_j) = -\frac{\partial p}{\partial x_i} + \frac{\partial}{\partial x_j}\left[\mu\left(\frac{\partial u_i}{\partial x_j} + \frac{\partial u_j}{\partial x_i}\right)\right] + \rho f_i , \tag{4.2}$$

$$\frac{\partial}{\partial t}(\rho E) + \frac{\partial}{\partial x_i}\left[u_i(\rho E + p)\right] = \frac{\partial}{\partial x_j}\left[K \frac{\partial T}{\partial x_j} + u_i(\tau_{ij})\right] + S_h , \tag{4.3}$$

Equations 4.1 to 4.3 represent continuity, momentum and thermal energy equations, respectively. In equation 4.2, f_i stands for body forces including gravity. In equation 4.3, E is the total energy and the first two terms on the right side represent the energy transfer due to conduction and viscous dissipation, respectively. In addition, S_h represents the volumetric heat source term in general, which is zero here. Also, the stress tensor ($\boldsymbol{\tau_{ij}}$) is calculated from the following relation:

$$\tau_{ij} = \mu\left[\left(\frac{\partial u_i}{\partial x_j} + \frac{\partial u_j}{\partial x_i}\right) - \frac{2}{3}\frac{\partial u_k}{\partial x_k}\delta_{ij}\right], \tag{4.4}$$

The equation of energy in the solid domain (i.e. graphite foam) simplifies to the heat conduction equation in which subscript s represents solid properties (equation 4.5):

$$\frac{\partial T}{\partial t} = \frac{\partial}{\partial x_j}\left(\left(\frac{k_s}{\rho_s . C_{p,s}}\right)\frac{\partial T}{\partial x_j}\right). \tag{4.5}$$

The corresponding governing equations were solved numerically for the PCM and graphite foam domains using the finite volume approach (Anderson, 1995; Ansys Fluent 12.0, 2009). These equations were subjected to the appropriate boundary conditions that are discussed in the following section.

4.3.4 Boundary Conditions

The boundary conditions were set for a unidirectional thermal analysis of the developed model subjected to a constant temperature gradient, as the following:

- Hot side: one side of the cubic REV was selected as the hot side and the temperatures of graphite and PCM on this side were set constant, T_h.
- Cold side: the opposite side of the hot side was selected as the cold side with the temperatures of graphite and PCM on this side set constant, T_c.
- The other four side walls were subjected to insulated (zero heat flux) boundary conditions.

It should be mentioned that the thermal conductivity of graphite foam was defined as a function of temperature (according to Klett et al., 2004) and used in different thermal analyses to extract the effective thermal conductivity of the graphite foam/PCM composite over a temperature range. Furthermore, the pores were assumed to be saturated with the PCM in liquid state (i.e. no voids within the pores), and natural convection flow pattern within the pores was assumed laminar since the Rayleigh number based on the pore diameter is approximately 10. This assumption was later justified upon examination of the numerical results. The no-slip boundary condition was used on the walls in contact with the fluid and there is no heat generation within the solid and fluid domains.

4.3.5 Numerical Method and Computational Details

The governing equations for energy transport in the solid graphite foam and the momentum/energy transport in PCM within pores were discretized using second order schemes and then solved numerically using the finite volume approach. The CFD package Fluent (Ansys Fluent 12.0, 2009) was used with a pressure-based formulation for numerical simulation of the governing equations. Upon convergence of the numerical solution for steady-state thermal analysis of the developed model, the total heat flux under a constant temperature gradient over

the REV was determined by integrating the heat flux over the hot and cold surfaces (the values are the same after solution convergence). Knowing the heat flux and temperature gradient over the REV leads to evaluation of the effective thermal conductivity of the composite based on the Fourier's law. The results of numerical simulation will be presented in section 4 and compared to experimental results as well as other work (Gaies and Faber, 2002; Leong and Li 2011). Considering the relatively large number of 3D grids in this model, numerical simulations were performed using a high-performance computing cluster (HPCC) for parallel processing. Using 16 processors in parallel, it took approximately 10-16 hours for different cases of steady-state thermal analyses to converge (i.e. normalized residuals of the continuity, velocity and energy become less than 10^{-12}, 10^{-5} and 10^{-10}, respectively).

4.4 Experimental Investigation of the Effective Thermal Conductivity

Experimental investigation of the effective thermal conductivity of graphite foam/PCM composite includes selection of the experimental method, preparation of composite sample and experimental setup, experimental measurements and associated uncertainties that are discussed in this section.

4.4.1 Experimental Method

Several experimental techniques have been developed for the purpose of thermal conductivity measurement. These techniques include steady-state methods such as absolute or direct, comparative and radial flow methods as well as transient methods such as the hot wire, plane source, 3ω, pulse-power and laser flash (Tritt, 2004). Each technique has its own limitations and some techniques are preferred over specific ranges of thermal conductivity or temperature. Some techniques are more appropriate to specific geometries of the sample. Some

techniques were developed for thermal conductivity measurement of pure materials, while there are other techniques that are appropriate for composite, multiphase or inhomogeneous materials (Tritt, 2004).

In general, the steady-state techniques are simpler because of using the Fourier's law. Whereas, the transient techniques have the advantage of being faster in measuring thermal conductivity, but their theory is more complicated. In addition, some of the transient methods were developed for single-phase materials, such as the transient hot wire (THW) for fluids and transient plane source (TPS) for solids, and some techniques have limitations on the sample geometry such as the 3ω technique for thin films (Tritt, 2004). Therefore, for the purpose of measuring the thermal conductivity of a composite material, consisting of more than a single phase (such as the graphite foam/PCM composite as a solid-liquid composite in the present work), the direct (i.e. absolute) steady-state method is simpler, less sensitive and preferred, even though a dedicated experimental setup is required for experimental measurement of temperature within the sample.

Consequently, the experimental investigation of thermal conductivity was conducted using temperature measurements within the composite sample, usually referred to as absolute or direct method. Furthermore, the experimental results of the bulk thermal conductivity of graphite foam, measured using the transient laser flash technique, are available in the literature (Gaies and Faber, 2002). Thus, selection of a steady-state method makes it possible to compare the experimental results of two different techniques for further validation purposes.

4.4.2 Sample Preparation and Experimental Setup

Several graphite foam samples (PocoFoam®) were prepared for experiments. The dimensions and mass of each sample were measured accurately. The samples are cubic in shape

with approximate side length of 25 mm. Four K-type thermocouples were calibrated and installed within the sample (along the vertical axis of rotational symmetry) at different heights for measuring the temperature distribution in the sample. The thermocouples were particularly calibrated using high-accuracy thermistors (Omega®, Stamford, CT) with maximum standard deviation and uncertainty of temperature readings being 0.021 and ±0.1 °C, respectively. The vertical positions of the thermocouples within the sample were measured carefully using a digital caliper (General®, No. 147, General Tools & Instruments™, New York, NY) with an accuracy of ±0.02 mm. The schematic diagram and a photo of the experimental set up are shown in figure 4.5a and b.

Upon installation of the thermocouples, the graphite foam sample was fitted into a test cell. The test cell is cubic in shape and consists of a 2mm thick aluminum plate at the bottom and low thermal conductivity glass on the sides, while the top side is open to the ambient. In order to realize unidirectional heat transfer, insulation of side walls is of great importance. Thus, in addition to the low-conductivity glass, three additional layers of insulation (including two layers of felt and a 2-cm-thick layer of Styrofoam®) were used to minimize heat loss from the sides.

Same insulation was applied to the bottom side after fixing an adjustable thermoelectric heater (TEH, Omegalux® model KHLV-101-10, Stamford, CT) under the aluminum plate using a thin (~0.5mm) layer of thermal grease. In effect, a constant heat flux is established on the bottom surface of the sample and heat transfers only in the vertical direction toward the top surface, where heat dissipates to the ambient maintained at a constant controlled temperature. Additional thermocouples were mounted on the inner and outer sides of the insulated walls to ensure minimum heat loss from side walls, as well as the ambient around the experimental setup

to check ambient temperature variation/uniformity. As a result, a total of 15 calibrated K-type thermocouples were used in this experimental setup.

4.4.3 Experimental Measurements and Associated Uncertainties

A compact real-time data acquisition (DAQ) system (NI cRIO-9014, National Instruments, Austin, TX) was used for recording the temperature readings during the tests. Temperature recording started before applying the heat flux while the entire setup is at the ambient temperature. For applying a constant heat flux, the input voltage of the TEH was provided by a variable transformer (Powerstat® type 3PN116C, Farmington, CT). In order to obtain improved accuracy, TEH input voltage (V) and electric current (I) were carefully set/measured using a digital multi-meter (Hewlett-Packard 3468A, Palo Alto, CA) with an accuracy of ±1.14% for AC voltage and current, respectively. Considering the heat flux generated by the TEH as $q"=V.I/A$ (with A standing for the constant area of the TEH), the uncertainties of the input voltage and current cause a variation of ±2.28% in the resulting heat flux.

Upon applying the heat flux, the composite sample starts heating up and its temperature increases with time until it reaches the steady-state condition while thermocouple readings are recorded. After observing a constant temperature distribution within the sample for at least 10 minutes, the condition is considered as steady, and the experiment is complete. Due to very small variations in thermocouple readings (of the order of 10^{-2} °C with maximum standard deviation of 0.02 °C over the last 200 temperature readings), the average of the last 200 readings (corresponding to the last 200 seconds of the test collected at a frequency of 1 Hz) was used as the final steady-state temperature distribution within the sample. Knowing the heat flux and temperature distribution, one can evaluate the effective thermal conductivity of the composite using the Fourier's law. Furthermore, having the uncertainties of the heat flux and measured

temperatures and based on the Fourier's law, the resulting uncertainty of the experimental effective thermal conductivity turned out to be ±0.88 W/m.K in the range of K_{eff} <25 W/m.K, ±1.49 W/m.K in the range of 25<K_{eff} <29, and ±2.92 W/m.K in the range of K_{eff} >29 W/m.K.

Two sets of experiments were performed for measuring the effective (bulk) thermal conductivity of the graphite foam (before infiltration with PCM) and graphite foam/PCM composite. For each set of experiments, different heat fluxes were applied. For each heat flux, the experiment was conducted four times in order to ensure repeatability and extract the uncertainty of the experimental data. The experimental results are presented in the next section and also compared to the numerical predictions as well as the reported experimental results of Gaies and Faber (2002). The obtained results is discussed and compared to the numerical results in the next section.

4.5 Results and Discussion

The obtained numerical and experimental results are presented in sections 4.5.1 and 4.5.2, respectively. For validation purposes, a comparison of the numerical and experimental results is given in section 4.5.3 for the graphite foam/PCM composite. Furthermore, the numerical and experimental results of the effective (bulk) thermal conductivity of the graphite foam are compared against the experimental results of Gaies and Faber (2002) using the laser flash technique.

4.5.1 Numerical Results

Based on the numerical method explained in section 4.3, several thermal analyses were performed at different temperatures for the graphite foam (when pores are filled with air) and graphite foam/PCM composite (when pores are saturated with PCM). The thermal conductivity

of the solid phase (graphite foam) was defined as a function of temperature (Klett et al., 2004) as shown in figure 4.6.

Different thermal boundary conditions were set and thermal analyses were conducted to obtain the temperature distribution within the composite REV, as presented in figure 4.7 for a temperature difference of 1 °C (T_h=301 K and T_c=300 K) for a graphite foam fully saturated with cyclohexane. Based on the obtained temperature field, the heat fluxes can be integrated over the hot and cold sides. Knowing the heat flux through the composite REV and the temperature difference, one can extract the effective thermal conductivity of the composite using the Fourier's law. The extracted effective thermal conductivity will be assigned to the corresponding average temperature of $(T_h+T_c)/2$. The thermal analysis was repeated with selection of different thermal boundary conditions to extract the effective thermal conductivity at different temperatures. The variation of the predicted effective thermal conductivity with temperature is shown in figure 4.8 for the graphite foam (pores are occupied by air) and graphite foam/PCM composite (pores are saturated with PCM).

It should be noted that the effective thermal diffusivity varies proportionally with the effective thermal conductivity since $(\rho C_p)_{eff} = \varepsilon(\rho C_p)_{liquid\ PCM} + (1-\varepsilon)(\rho C_p)_{graphite}$ is constant in this study. However, in case of evaluating graphite foam/solid PCM composite, the term $(\rho C_p)_{liquid\ PCM}$ will be replaced with $(\rho C_p)_{solid\ PCM}$ which has a different value and will affect the effective thermal diffusivity. The evaluated effective thermal conductivity in this study covers the range of temperature corresponding to graphite foam/liquid PCM composite.

In order to study the role of natural convection within the pores on the effective thermal conductivity, two sets of thermal analyses (on graphite foam and graphite foam/PCM composite) were conducted with and without solving the continuity and momentum equations within the

liquid PCM. A small difference was observed between the obtained effective thermal conductivities. In fact, considering the pore size, thermophysical properties (table 4.1) and thermal conditions, the Rayleigh (*Ra*) number is approximately 6.7×10^{-3} and 10 for air and cyclohexane, respectively, indicating the negligible role of natural convection as the onset of natural convection within spheres was reported to be around 10^5 (Hutchins and Marschall, 1989). The difference is negligible due to size of the pore, very weak velocities and natural convection within the pore, and low thermal conductivity of the air (in case of graphite foam) or PCM (in case of graphite foam/PCM composite) compared to high thermal conductivity of solid graphite. The role of natural convection in pores was also reported to be negligible by (Leong and Li, 2011). Natural convection can potentially affect the thermal conductivity predictions for larger pore sizes (Alam and Maruyama, 2004).

4.5.2 Experimental Results

According to the experimental method explained in section 4.4, the temperature variation was measured within samples of graphite foam and graphite foam/PCM composite. A representative set of the measured temperatures of the composite sample during an experiment is given in figure 4.9. As it is observed, upon applying the heat flux on the bottom side of the sample, the uniform temperature of the sample (initially equal to the ambient temperature) varied with time until it reached the steady-state distribution during which thermocouple readings do not change with time.

The steady-state temperature distribution in the sample was obtained using the average of thermocouple readings for the last 200 seconds of test. One should note that during each test, the steady-state condition was continued for at least 10 min. Furthermore, each test was conducted 4 times to ensure repeatability and obtain the associated uncertainties. Based on the averaged (of

the 4 tests) steady-state temperature distribution and position of the thermocouples within the sample, the temperature gradient (dT/dy) was extracted, as presented in figure 4.10 for three different values of the applied heat flux. Having the applied heat flux and temperature gradient within the sample, one can obtain the effective thermal conductivity of the sample for different heat fluxes corresponding to different average temperatures of the sample. The experimental results of the effective thermal conductivity and associated uncertainties are shown in figure 4.11 for graphite foam (bulk) and graphite foam/PCM composite. It should be noted that the uncertainty of thermal conductivity is a function of heat flux, temperature difference, sample size and their corresponding uncertainties. The uncertainty of heat flux depends on the uncertainties of TEH input voltage and current and turned out to be 2.28% of applied heat flux. Since the applied heat flux, its uncertainty and temperature difference in the sample vary among different experiments, the resulting uncertainty of thermal conductivity varies with temperature, as presented in figure 4.11.

4.5.3 Comparison of the Results and Validation

For validation purposes, the numerical results of the effective thermal conductivity are also presented in figure 4.11 for graphite foam and graphite foam/cyclohexane composite. A good agreement is observed with a maximum deviation of 3.5% between the numerical and experimental effective thermal conductivities of graphite foam/cyclohexane composite. Additionally, the effective thermal conductivity of graphite foam based on our numerical and experimental results is presented in figure 4.12 along with the experimental results of Gaies and Faber (2002) that were obtained using the laser flash technique. Results obtained using various approaches are in good agreement with the maximum deviations of 2.6% between our

experimental results and experimental results of Gaies and Faber (2002) and 9.15% between the numerical and experimental results of this study.

It is also observed that the numerical predictions of the effective thermal conductivity are slightly lower than the experimental values. One possible reason is the small amount of heat loss from the insulated side walls during the experiments compared to an ideal zero heat flux boundary condition used in thermal analyses. Such heat losses can also be the reason why the averages of the steady-state thermocouple readings within the sample do not exactly fit to a linear temperature distribution (see figure 4.10b and c). Thermal contact resistance between the thermo-electric heater and the sample is another deviation between the numerical model and experimental setup. Although a thin layer of thermal grease was applied in experimental setup to the space between the TEH and the bottom plate, the thermal contact is still not ideal as assumed in the numerical model. Furthermore, in the numerical model the pores were idealized as uniform spheres, whereas in actual foam there is always a pore size distribution and the pores are not perfectly spherical in shape. Also, a slight approximation in defining the thermal conductivity of graphite as a function of temperature (using curve-fit to data of Klett et al., 2004) can be a reason for slight deviation in numerical results. Another reason could be the presence of non-homogeneities including small impurities or non-uniformities in the size and structure of pores in real foams such as dead-end pores that are not accounted for in the numerical model of the composite.

4.6 Conclusions

Numerical and experimental investigation of the effective thermal conductivity of graphite foam/ PCM composites was conducted. In the numerical approach, the structure of graphite foam was modeled as a 3D body-centered cube arrangement of uniform spherical pores, having the

same porosity as the actual foam. The pores were fully saturated with cyclohexane as a typical PCM to construct the representative elementary volume of the composite. Thermal analysis of the developed REV was conducted for the case of unidirectional heat transfer using isothermal boundary conditions on walls in one direction, and insulated walls in other two directions. Upon converging the numerical solution, the total heat flux was determined by integrating the heat fluxes over the hot and cold surfaces. Having the heat flux, temperature difference and size of the 3D REV, the effective thermal conductivity was evaluated.

In the experimental phase of the investigation, a sample of graphite foam was prepared and infiltrated with cyclohexane. The effective thermal conductivity was evaluated using the direct method of measuring temperature within the sample under a fixed heat flux in unidirectional heat transfer. The heat flux was applied on the bottom wall, and the temperature distribution was measured using four thermocouples within the sample until reaching the steady-state condition. Having the heat flux and temperature gradient, one can evaluate the effective thermal conductivity of the sample.

The numerical and experimental results were found to be in good agreement. Furthermore, our results of graphite foam's effective thermal conductivity are in good agreement with the experimental results of Gaies and Faber (2002) obtained using the laser flash technique. It is concluded that the graphite foam with its highly-conductive and highly-porous structure, is an excellent candidate for improving the thermal conductivity of PCM. In this study, high values of the effective thermal conductivity varying from 30 W/m.K (at 20 °C) to 25 (at 90 °C) were obtained in comparison with the thermal conductivity of cyclohexane (0.13 W/m.K). Furthermore, the role of natural convection within the graphite foam pores was found to be negligible.

Table 4.1 Thermophysical properties of graphite foam, cyclohexane (PCM) and air (based on Yaws, 2008; Silva et al., 2009 and Klett et al., 2004)

Property	Unit	Graphite foam	Cyclohexane	Air
Density, ρ	$kg\ m^{-3}$	500	778.9	1.205
Specific Heat, *Cp*	$J.kg^{-1}.K^{-1}$	700	1857	1005
Thermal Conductivity, *K*	$W.m^{-1}.K^{-1}$	*f(T)* (figure 4.6)	0.13	0.0257
Dynamic Viscosity, μ	$kg.m^{-1}.s^{-1}$	N/A	9.8467×10^{-4}	1.82×10^{-5}
Thermal Expansion Coefficient, β *	K^{-1}	N/A	1.76×10^{-3}	3.43×10^{-3}
Prandtl Number, *Pr* *		N/A	14	0.71

*: The value was used in estimation of the Grashof (*Gr*) and Rayleigh (*Ra*) numbers.

(a)

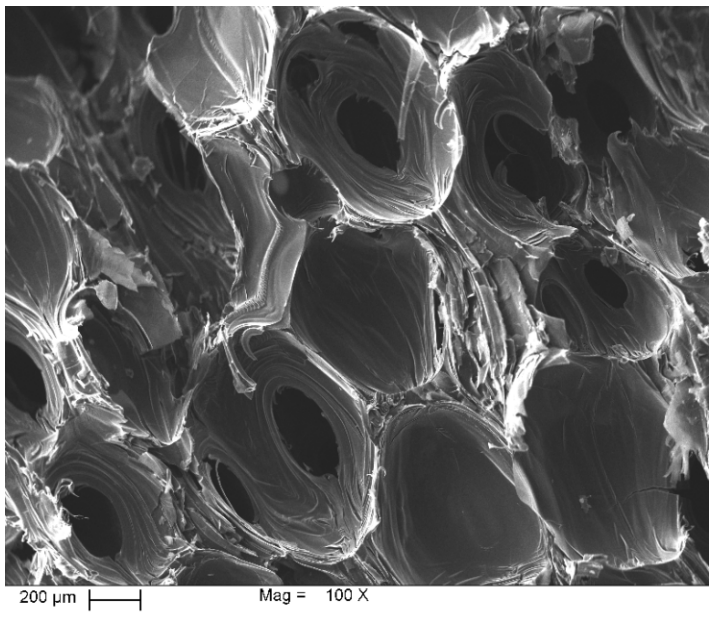

(b)

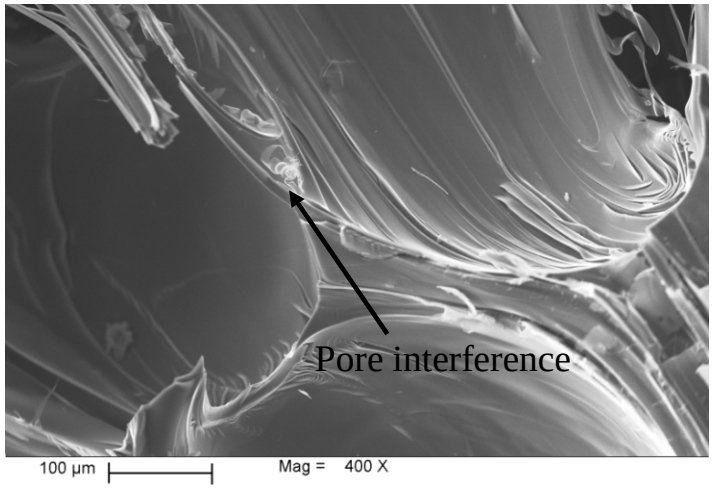

Figure 4.1 SEM images of the structure of graphite foam (PocoFoam®, Poco Graphite Inc.) showing the interconnected nearly-spherical pores of micro-structure in (a) 100X, and (b) 400X magnifications.

(a)

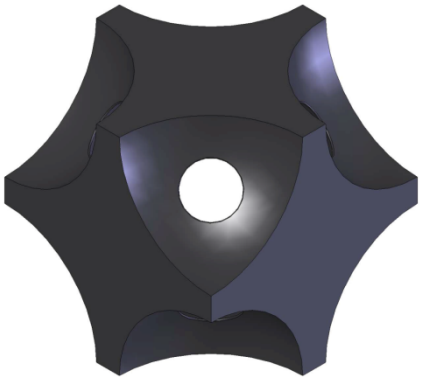

(b)

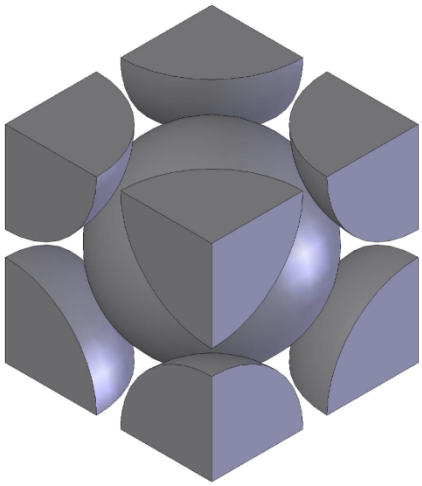

(c)

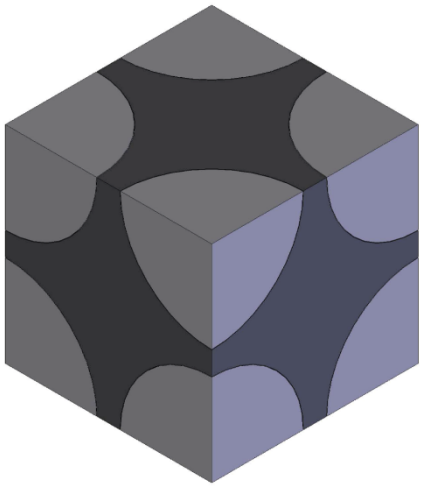

Figure 4.2 Three-dimensional model of (a) solid foam, (b) interconnecting pores and (c) assembled model of graphite foam/PCM composite (graphite foam in dark gray and PCM in light gray).

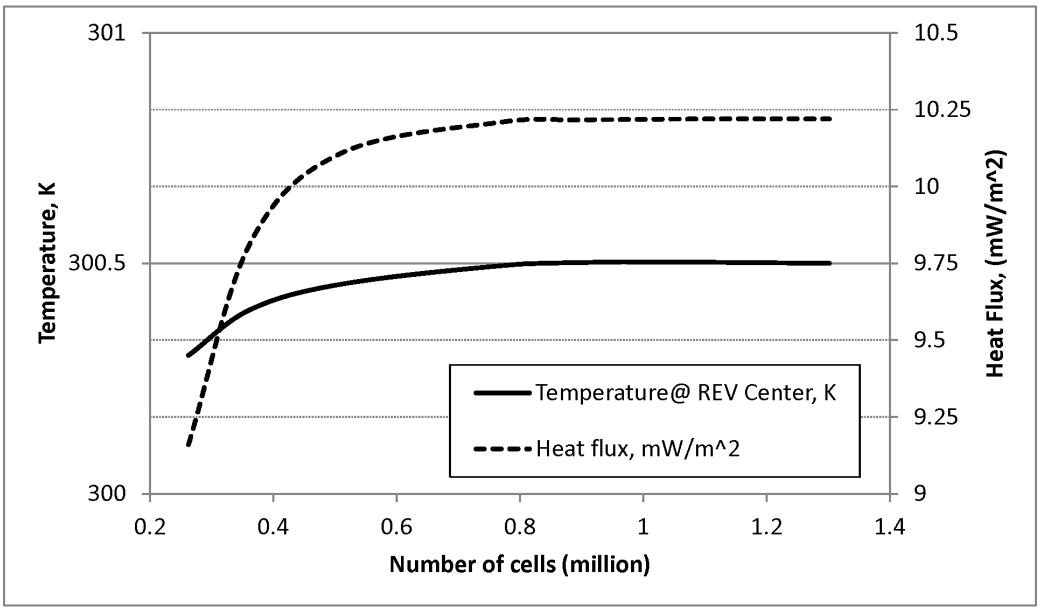

Figure 4.3 Grid-independence study considering the temperature at the center of the REV (as a point-wise quantity), as well as the heat flux on the active sides (hot or cold) of the REV (as an integral derivative quantity).

(a)

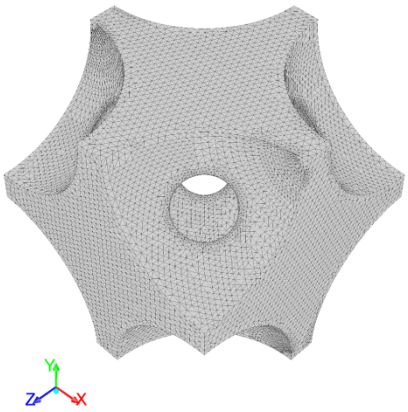

(b)

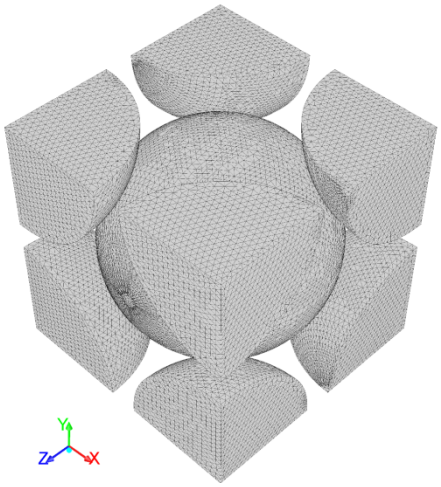

(c)

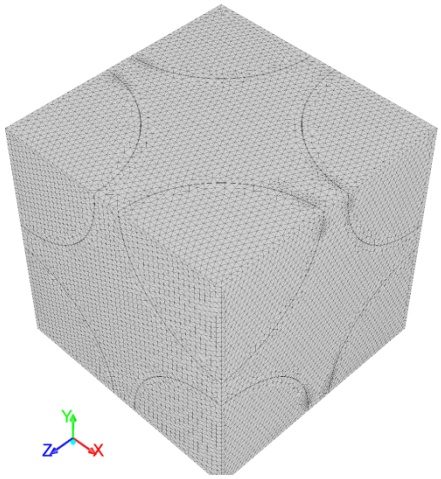

Figure 4.4 Selected unstructured tetrahedral grid in (a) graphite foam, (b) fluid within pores (PCM) and (c) the graphite foam/PCM composite (total of 1,110,512 tetrahedral cells).

(a)

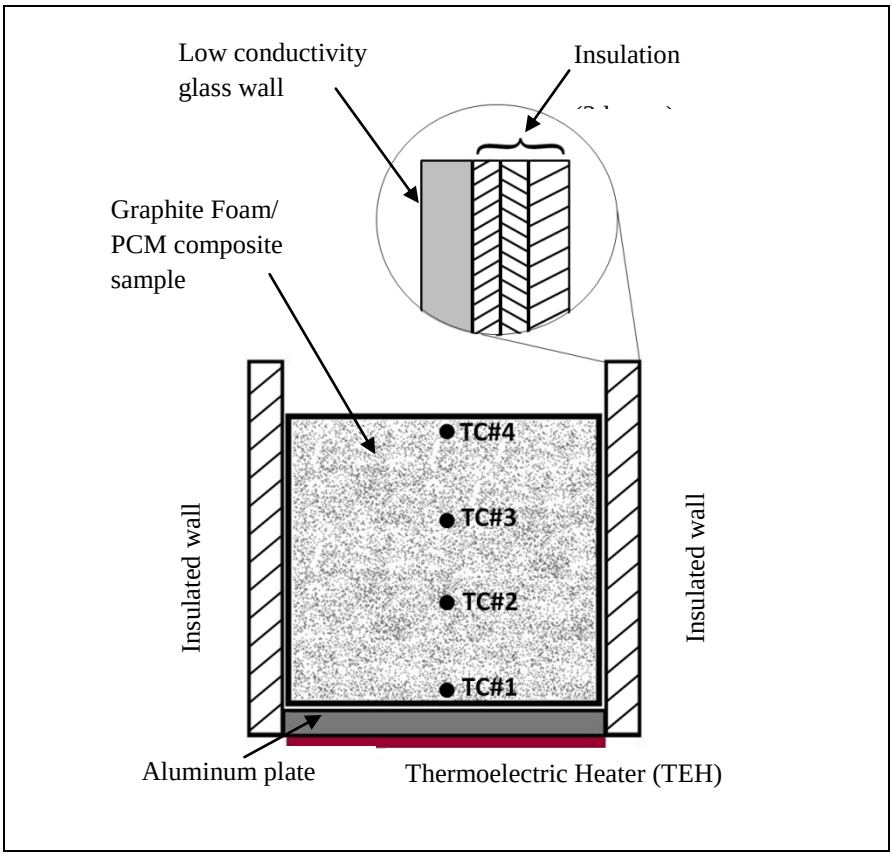

(b)

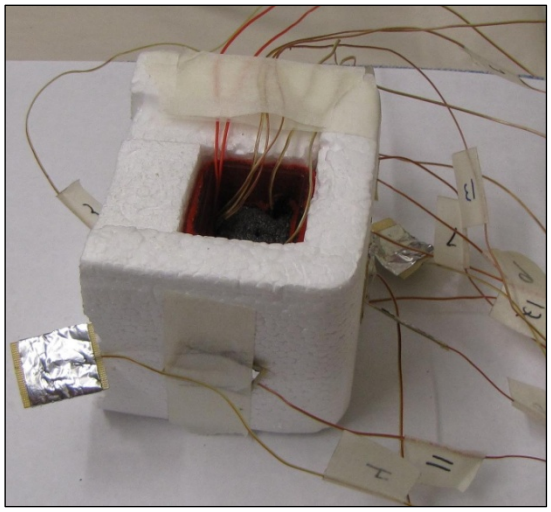

Figure 4.5 (a) Schematic diagram of the experimental set up for thermal conductivity measurement and (b) Photo of the experimental setup and installed thermocouples.

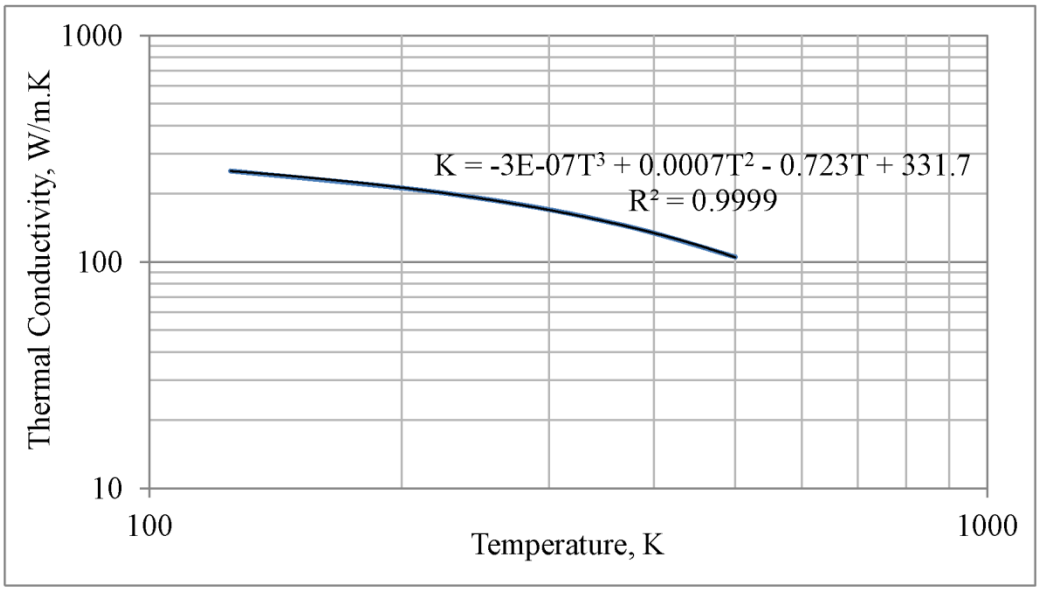

Figure 4.6 Thermal conductivity of solid graphite as a function of temperature (reproduced from data of Klett et al., 2004).

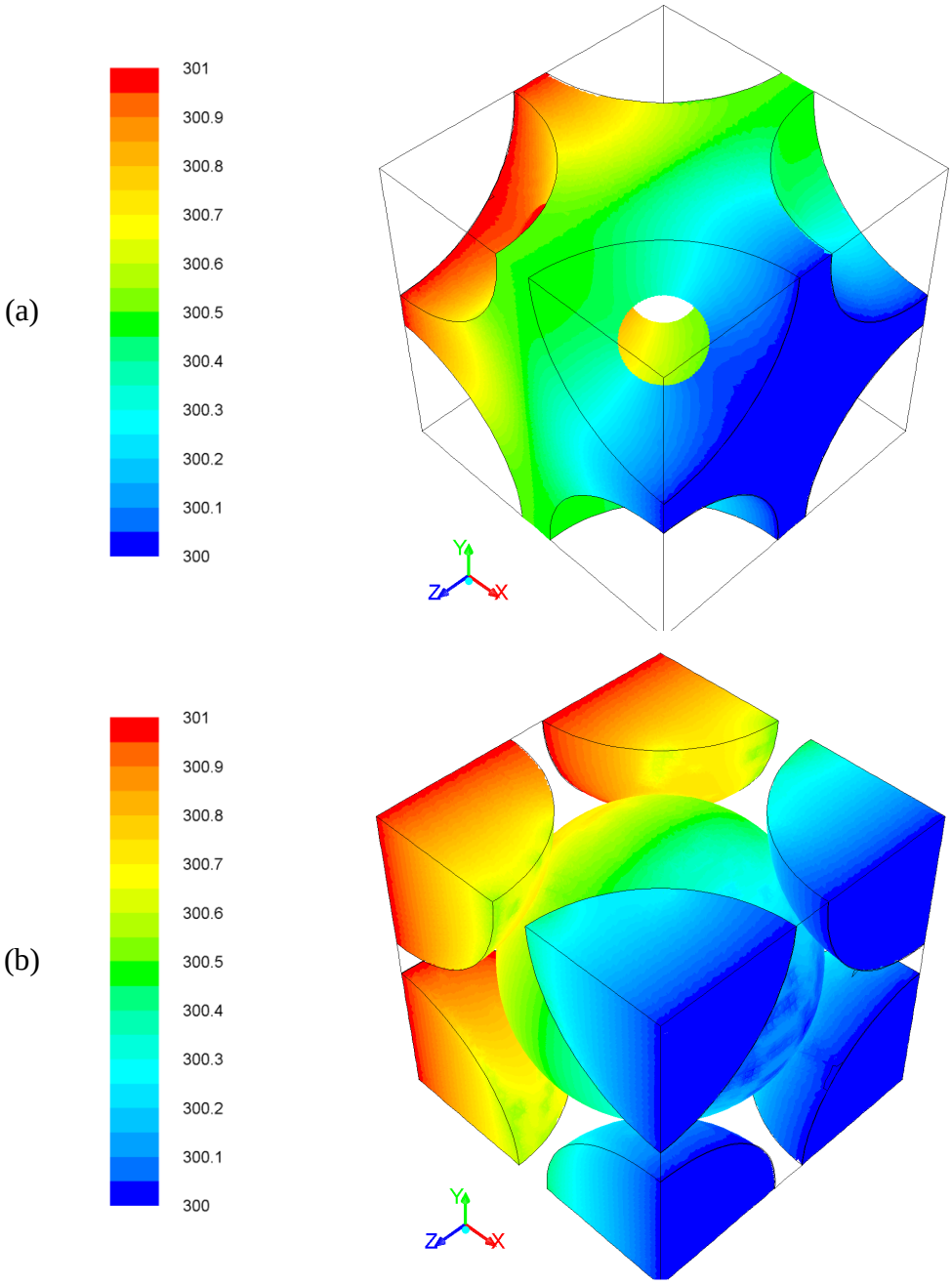

Figure 4.7 Temperature distribution for a difference of 1 °C in the x-direction (T_h=301 K and T_c=300 K as a periodic boundary condition resembling/corresponding to a temperature difference of 22 °C over a composite slab of 1 cm thickness) within (a) the graphite foam structure, and (b) the liquid PCM (cyclohexane).

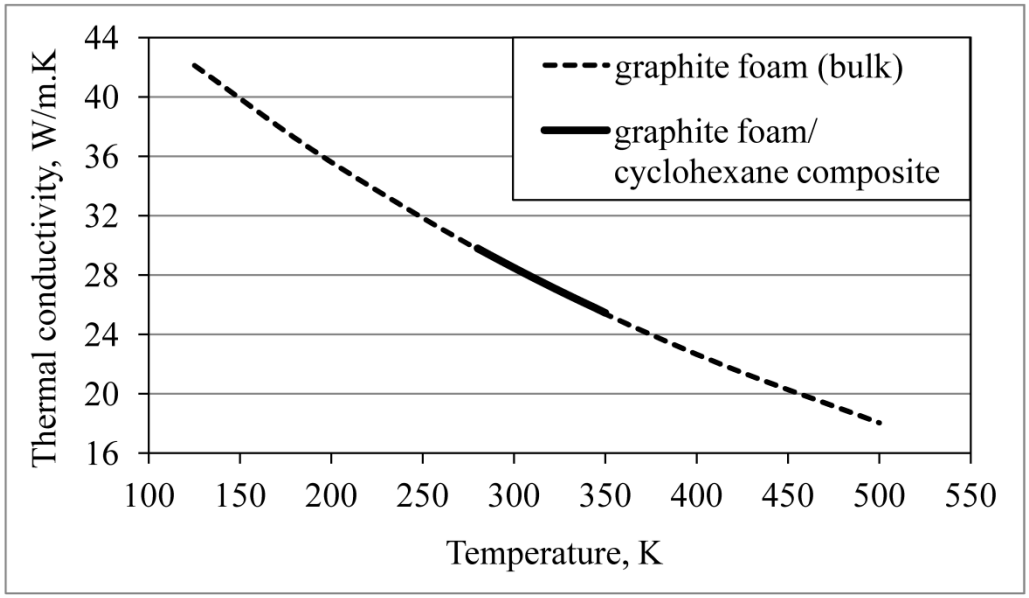

Figure 4.8 Numerical predictions of the effective thermal conductivity versus temperature for graphite foam as well as graphite foam/cyclohexane composite.

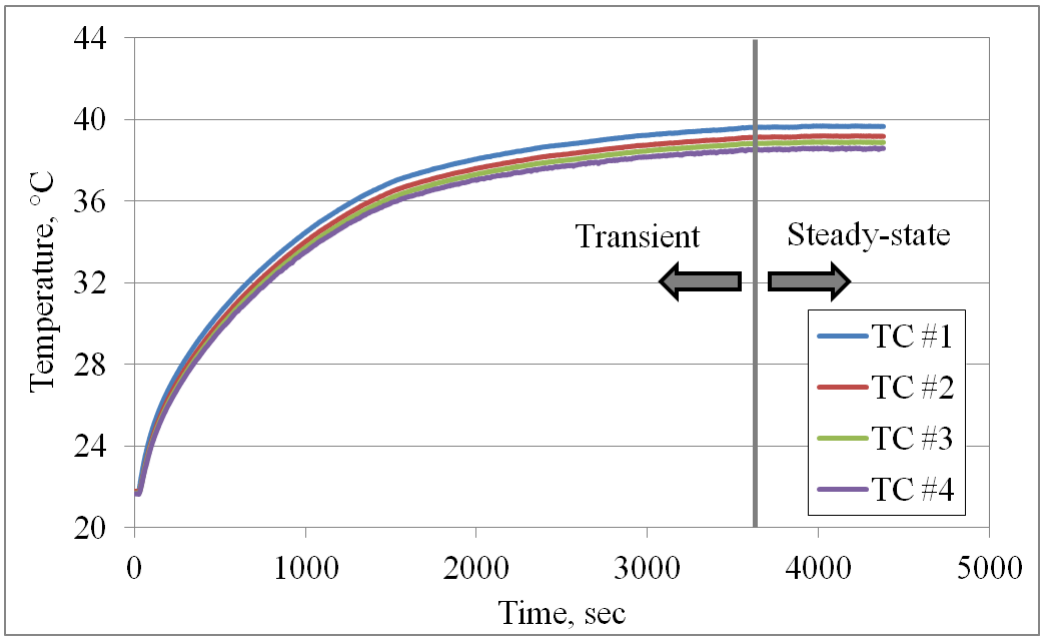

Figure 4.9 Measured transient and steady-state temperature distributions within the graphite foam/cyclohexane composite sample upon applying a heat flux of 1380 W/m^2.

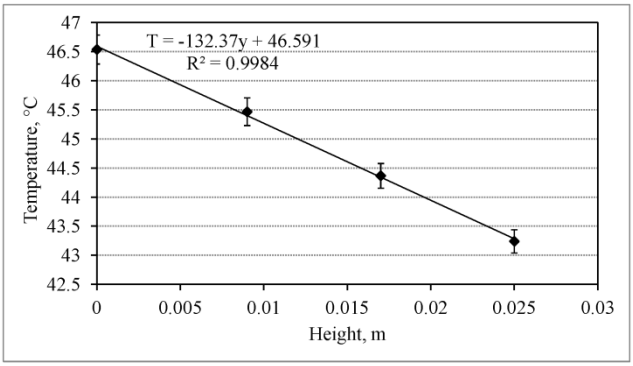

(a) q” = 3875 W/m^2

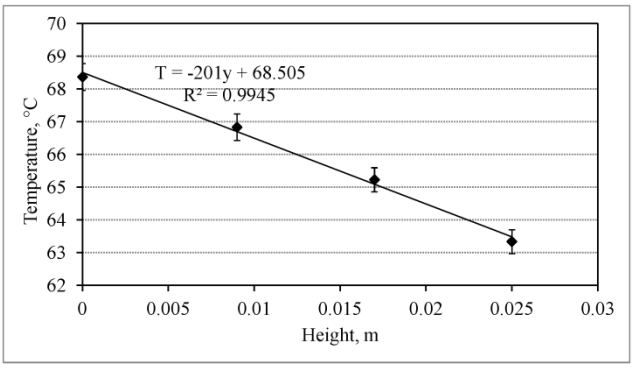

(b) q” = 5535 W/m^2

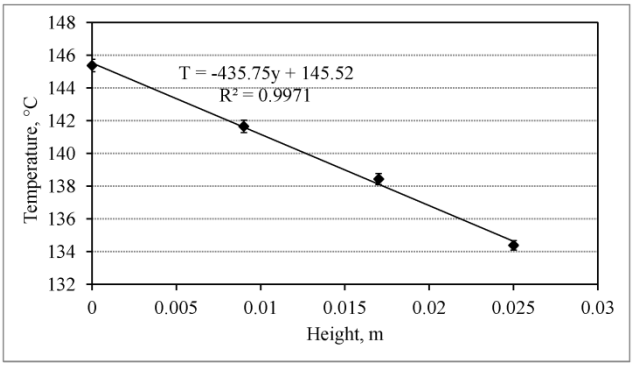

(c) q” = 10050 W/m^2

Figure 4.10 Steady-state temperature distribution within the graphite foam sample for 3 different values of applied heat flux (filled symbols and bars represent the average measured temperature and standard deviation, respectively).

(a)

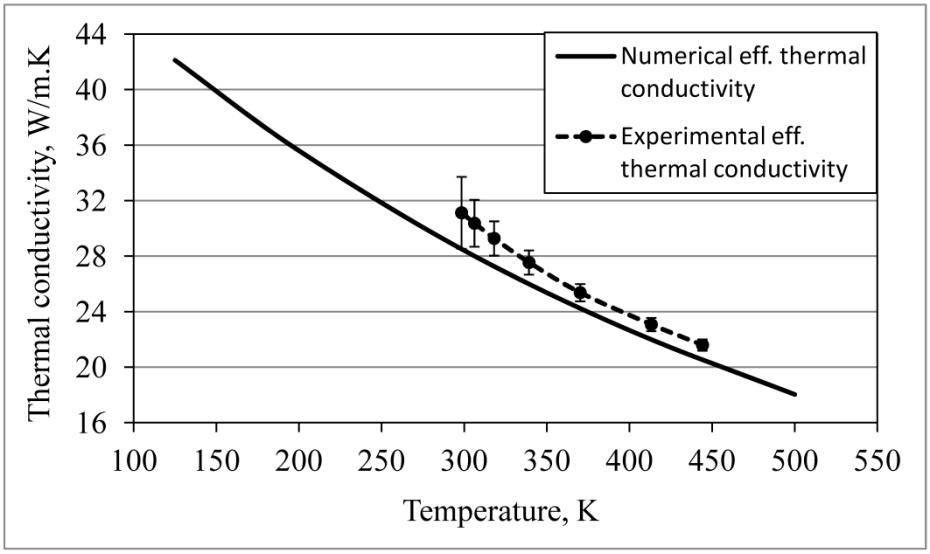

(b)

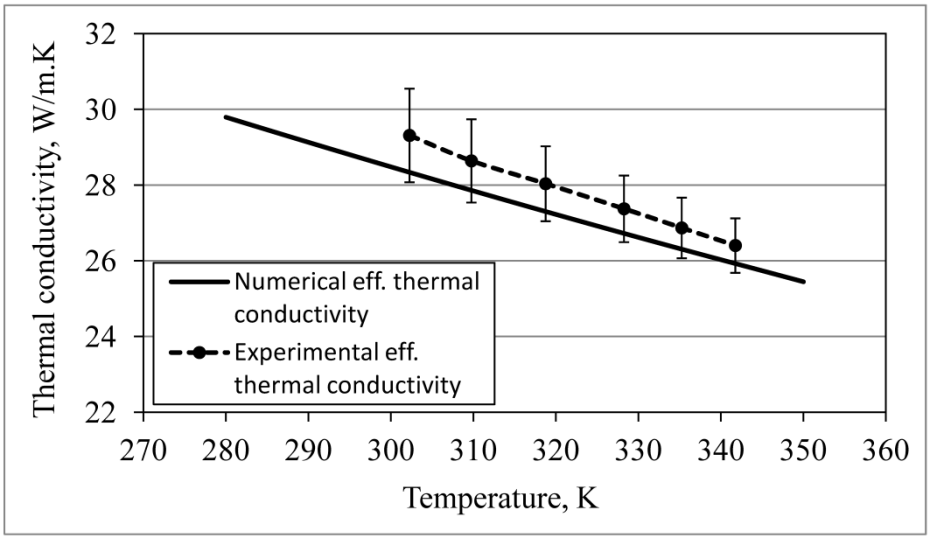

Figure 4.11 Experimental effective thermal conductivity compared to numerical predictions for (a) graphite foam and (b) graphite foam / cyclohexane composite (bars represent the corresponding uncertainties).

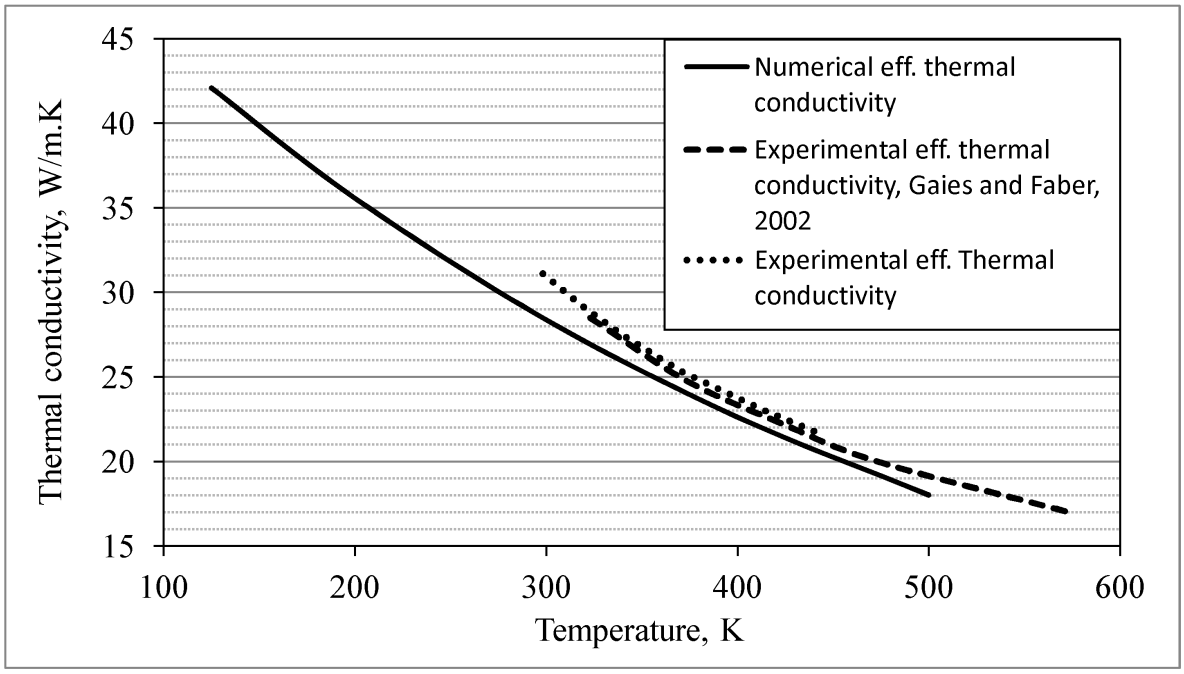

Figure 4.12 Effective thermal conductivity of the graphite foam – comparison among the numerical and experimental results of this study as well as the experimental results of Gaies and Faber (2002).

Chapter 5 Conclusions

Development, utilization and thermal conductivity improvement of thermal energy storage composites, consisting of graphite foam impregnated with phase change materials, were investigated in this dissertation. The development of such TES composites mainly depends on the characteristics of the infiltration process (chapter 2), whereas utilization of TES composites involves phase change processes during freezing/thaw cycles for energy discharge/charge (chapter 3). In addition, the resulting composite has an improved thermal conductivity that enhances the thermal performance of PCM (chapter 4). The concluding remarks are presented in this chapter along with proposed future work regarding the emerging aspects in further development and achieving higher effective thermal conductivity in TES systems.

5.1 Concluding Remarks

Regarding the development of TES composites, the infiltration process was investigated at the pore level numerically and experimentally, with the purpose of elucidating the interface behavior and details related to undesirable formation of voids. Existence of these voids as reported in the literature by several experimental studies of liquid composite molding is known to adversely affect the thermo-physical properties and energy storage capacity of the resulting composite. In order to study the evolution of the liquid interface, a multiphase approach was selected in the numerical investigation based on the VOF method. The infiltration of PCM (as a liquid) into a porous structure (graphite foam) was studied at the pore level and the evolution of the interface (liquid front) was investigated for both wetting and non-wetting liquids. The effect

of different driving forces and interfacial effects (especially wettability or wall contact angle) on infiltration process and liquid interface behavior was studied and reported (chapter 2).

It was observed that for wetting liquids the shape of the interface is concave and temporary and permanent interface pinning occur depending on the combination of pressure difference and interfacial effects (surface tension and more importantly the wall contact angle) as the major driving forces during the infiltration of wetting liquids. Infiltration criterion for wetting liquids was studied and the global infiltration time versus pressure was obtained using dimensionless quantities. Infiltration under zero pressure gradient and no gravity, also known as wicking flow, occurs in wetting liquids with interfacial effects as the only driving forces. The case of wicking flow was investigated numerically and experimentally for validation purposes. Due to the concave shape of the interface in wetting liquids, void formation was not observed since the liquid wets the walls of the pore prior to filling the interior space (bulk) of the pore. However, it should be mentioned that void formation might occur due to other reasons such as presence of dead-end pores or vaporization during infiltration.

Using the same approach, the infiltration process was investigated for non-wetting liquids and the interface evolution was elucidated. Unlike wetting liquids, it was observed that the interface shape is convex (due to the contact angle greater than 90°) and no interface pinning occurs for non-wetting liquids. Instead, a fingering phenomenon was observed during the infiltration of the pore followed by the impingement of the liquid finger on the walls of the pore that is responsible for entrapment of air and void formation within the pore. The proposed numerical method was capable of tracking the interface and predicting the formation of void within the pore. The volume and distribution (shape) of the void, also known as infiltration void, in the pore was predicted for non-wetting liquids and correlated to the modified capillary

number. The void content of the pore (versus modified capillary number) was compared and found to be in agreement with the experimental results, available in literature.

The numerical results were verified against those obtained from the coupled VOF-Level Set method, known to have higher accuracy in capturing the interface. The predicted time-evolving liquid interfaces based on these methods were compared against each other for wetting and non-wetting liquids in several selected time instants during the infiltration. The shape and position of the liquid interface were found to be in good agreement between the VOF and CVOFLS methods. Furthermore, the infiltration time was extracted for wetting and non-wetting liquids using both methods and found to be in good agreement.

Moreover, the numerical results of horizontal wicking flow through the network of pores in series (no pressure gradient and no gravity) were validated against the experimental results of unidirectional horizontal wicking and theoretical results based on the modified Washburn equation. For this purpose, an experimental setup was designed for horizontal (i.e. no gravity), unidirectional wicking of cyclohexane (as a typical hydrocarbon PCM with wetting properties) into graphite foam samples. To provide wicking flow conditions, the experimental setup was designed so that the pressure gradient in the direction of liquid penetration into the porous structure was eliminated. The liquid penetration length versus time was extracted from the conducted experiments, for which good agreement was found between the numerical, experimental and theoretical results based on the modified Washburn equation.

Regarding the utilization of TES composites, the numerical simulation of the phase change processes was performed using a multiphase approach and based on the combination of the VOF and the enthalpy-porosity methods. Phase change processes occur when a TES system experiences freezing/thaw cycles. Since void formation happens during infiltration of TES

composites, the effect of voids were investigated on the solidification and melting processes. Additionally, the volume change of PCM during the phase change contributes in formation of ‘shrinkage voids’ in contrast to the ‘infiltration void’. For this purpose, the final state of the infiltration process, as pore contains a void portion, was used as the initial state of the solidification process. Therefore, the infiltration void is present within the pore during the phase change processes and its effect was included by utilizing the coupled phase change and multiphase methods. Moreover, the proposed coupled method takes into account the variation of density between liquid and solid phases and is capable of predicting the volume changes (contraction or expansion) during the phase change processes.

Solidification and melting simulations were conducted for a two-dimensional model of the pore and the evolution of the freezing/melting fronts in the PCM within the pore were extracted along with the volume change of PCM and the final volume of the shrinkage void. With regard to verification of results, it was found that the volume of the shrinkage void is in good agreement with the theoretical volume change due to density change. Since the simulation is transient, the temporal evolution of shrinkage void was extracted during the solidification of PCM which led to prediction of the distribution (shape) of the shrinkage void within the pore. Such distribution was found rational with respect to the observed convection patterns during the solidification of PCM within the pore. Upon freezing the entire PCM content of the pore, the melting process was investigated using the same method. The time-dependent evolution of melting front was obtained for PCM within the pore. It was found that the shrinkage void vanishes upon melting the entire PCM content of the pore. Additionally, a temperature gradient was observed along the PCM/void interface within the pore during the phase change processes.

Upon observing a temperature gradient on the PCM/void interface (resulting from the presence of voids) within the pore, the effect of the Marangoni convection (thermocapillary) on the phase change processes was investigated at the pore level. In fact, the presence of the infiltration void within the pore can affect the phase change processes by triggering thermocapillary effects along the PCM/void interface. The effect of the Marangoni convection on phase change processes were studied numerically using the same method. The variations of liquid density and surface tension with temperature were included to enable evaluation of the volume change as well as thermocapillary effects during the phase change. The time-dependent simulations were performed for solidification and melting with and without thermocapillary effects. The final status of phase change processes, position and shape of voids, shrinkage void formation and its volume, convection patterns within the pore and phase change time (duration) were extracted and compared between cases with and without thermocapillary convection.

It was found that thermocapillary forces are strong enough to overcome the gravitational forces and influence the convection pattern within the pore. This led to a significant change in the convection pattern as well as phase change time (about 8% reduction in duration of phase change due to thermocapillary convection in the pore). Furthermore, verification of the results was conducted by comparing the volume of the shrinkage void with the theoretical volume change during the phase change.

Upon considering the infiltration and phase change in TES composites, thermal characterization of such composites was investigated. The duration of phase change processes and the rate of charge/discharge of energy have been already reported in the literature for TES composites. However, evaluation of the effective thermal conductivity of TES composites is a novel contribution in thermal characterization of the composites that was investigated in this

dissertation. Therefore, the effective thermal conductivity of TES composites was also investigated for composites of graphite foam/PCM numerically and experimentally. In the numerical approach, the structure of the graphite foam was modeled as a three-dimensional body-centered cube arrangement of uniform spherical pores with the same porosity as the actual foam. The pores were fully saturated with cyclohexane as a typical PCM (wetting liquid) to construct a representative elementary volume of the composite. Thermal analysis of the developed REV was conducted for the case of unidirectional heat transfer using isothermal boundary conditions on walls in one direction, and insulated walls in other directions. Upon convergence of the numerical solution, the total heat flux was determined by integrating the heat fluxes over the hot and cold surfaces. Having the heat flux, applied temperature difference through boundary conditions and size of the three-dimensional REV, the effective thermal conductivity of the composite was evaluated based on the Fourier's law. Furthermore, the effect of natural convection within the pore on the effective thermal conductivity was studied. For the case of the graphite foam with an average pore size of 400 microns, the role of natural convection was found to be negligible.

For experimental investigation, a sample of graphite foam was prepared and infiltrated with cyclohexane to form a TES composite. An experimental setup was designed to hold the TES sample in a test cell for performing thermal conductivity measurement using the direct (absolute) method. The test cell was insulated on the side walls with three layers of insulation to minimize heat loss during the experiments. A fixed heat flux was applied on the bottom wall of the test cell using a thermo-electric heater. Heat was dissipated to the ambient (with constant temperature) from the top wall, thus establishing unidirectional heat transfer within the composite sample. The effective thermal conductivity was evaluated using the direct (absolute)

method of measuring temperature using four thermocouples within the sample under fixed heat flux in unidirectional heat transfer. The temperature distribution was extracted from the measurements until reaching the steady-state condition. Knowing the heat flux and temperature gradient, one can evaluate the effective thermal conductivity based on the Fourier's law.

The numerical and experimental results were found to be in good agreement. Furthermore, the effective thermal conductivity of graphite foam (when the foam is filled with air) was measured using the same experimental method and found to be in good agreement with the experimental results of the laser flash technique, available in the literature. It is concluded that highly-conductive and highly-porous structures, such as graphite foam, are excellent candidates for thermal conductivity improvement of PCM. In this study, high values of the effective thermal conductivity varying from 30 W/m.K (at 20 °C) to 25 W/m.K (at 90 °C) were obtained in comparison with the thermal conductivity of cyclohexane (0.13 W/m.K).

5.2 Proposed Future Work

In this dissertation, the infiltration process was investigated at the pore level using a multiphase approach for direct numerical solution of the governing equations. With recent advancements in modeling and computations, same approach might be conducted at the level of TES composite. For such cases, modeling the porous structure can be conducted for a random packing of pores including the pore size distribution. Such modeling techniques have been recently developed (for instance by James et al., 2010), however direct numerical solution of the governing equations in three dimensions at the system level requires an extensive computational resources, power and time. Such simulations can be used to predict details such as fingering phenomenon during liquid penetration into the porous structure as the source of air entrapment and formation of macro-voids. It should be noted that accuracy of the three-dimensional liquid

interface capturing and tracking schemes and extremely fine spatial and temporal grid requirements are challenges of such simulations at the system level.

Vaporization of liquid (PCM) during the infiltration is another source of void formation. During the fabrication of TES composites, usually the infiltration process occurs under low pressure for the purpose of minimization of voids. Under such conditions, evaporation of the penetrating liquid might be a contributing factor to formation of voids. In the present investigation of the infiltration process, the evaporation of liquid was not included and is thus suggested as a future work. However, including evaporation models adds a new gas phase (vapor) to the multiphase method and introduces more governing equations, coupled to the existing ones. This adds instability to the numerical solution of the entire set of equations and can be challenging, especially due to different time scales and dependence of such phenomena on multiple variables/factors.

The current studies and reported experimental values indicate that formation of the infiltration void is inevitable. Removal of the infiltration void is not usually considered in different applications due to the prevailing challenges in volume change of PCM during phase change, occurring during the life time of TES systems, and possible damaging effects. However, optimization of the infiltration void is of great interest in maximizing the energy storage capacity of TES composites. Such study is proposed as a future work here and requires an extensive investigation of the effects of different parameters (such as ambient pressure and wall contact angle) on the infiltration process and correlation of the void content with respect to these factors for further optimization.

Regarding the thermal conductivity improvement in PCM applications, the effective thermal conductivity of PCM infiltrated in graphite foam was investigated in this dissertation.

The obtained results were promising and exhibited ‘order-of-magnitude’ levels of improvement. However, further improvements can be obtained using the notion of ‘dual-scale’ thermal conductivity improvement. This consists of thermal conductivity improvement in micro-scale (infiltration of the PCM into micron size pores of a conductive porous structure) as well as nano-scale enhancement by employing nanostructure-enhanced phase change materials (NePCM) with an expedited freezing/melting rate. There are currently several challenges regarding development and thermal conductivity enhancement of NePCM such as the stability of colloidal suspensions, variation of thermophysical properties, especially viscosity and thermal conductivity, in nanofluids and formation of dendritic structures during the freezing and melting of colloidal suspensions. However, it was shown (Gao et al., 2009; Gharagozloo and Goodson, 2010 and Zheng et al., 2011) that in nanofluids, clustering of nanoparticles can lead to formation of fractal percolation paths within the nanofluids and thus cause thermal conductivity improvement. Thus infiltration of nanofluids, especially with high aspect-ratio nano-structures (Babaei et al., 2013), into conductive porous structures (such as graphite foam) might lead to even greater enhancements in thermal conductivity due to presence of foam structure in micro-scale as well as percolation within the NePCM in nano-scale, which is proposed here as a future study.

Bibliography

Abdolmaleki, K., Thiagarajan, K. P., and Morris-Thomas, M. T., 2004, "Simulation of the dam break problem and impact flows using a Navier-Stokes solver," *15th Australasian Fluid Mechanics Conference*, December 13-17, Sydney, Australia.

Alam, M. K., Druma, A. M., and Druma, C., 2004, "Thermal transport in graphitic carbon foams," *Journal of Composite Materials*, **38**(22), pp. 1993-2006.

Alam, M. K., and Maruyama, B., 2004, "Thermal conductivity of graphitic carbon foams," *Journal of Experimental Heat Transfer*, **17**(3), pp. 227-241.

Anderson, J. D., 1995, *Computational fluid dynamics: the basics with applications*, McGraw Hill series in aeronautical and aerospace engineering, McGraw-Hill, Inc., New York, NY.

ANSYS Inc., 2009, "ANSYS FLUENT 12.0 theory guide," ANSYS Inc., PA, USA.

ANSYS Inc., 2010, "ANSYS FLUENT 13.0 theory guide," ANSYS, Inc, PA, USA.

Antar, B. N., Collins, F. G., and Fichtl, G. H., 1980, "Influence of solidification on surface tension driven convection," *International Journal of Heat and Mass Transfer*, **23**(2), pp. 191-201.

Babaei, H., Keblinski, P., and Khodadadi, J. M., 2013, "Improvement in thermal conductivity of paraffin by adding high aspect-ratio carbon-base nano-fillers," *Physics Letters A*, **337**(19-20), pp. 1358-1361.

Beckermann, C., and Viskanta, R., 1988, "Double-diffusive convection during dendritic solidification of a binary mixture," *Journal of PhysicoChemical Hydrodynamics,* **10**(2), pp. 195-213.

Berthier, J., Loe-Mie, F., Tran, V. M., Schoumacher, S., Mittler, F., Marchand, G., and Sarrut, N., 2009, "On the pinning of interfaces on micropillar edges," *Journal of Colloid and Interface Science,* **338**, pp. 296-303.

Bickerton, S., and Advani, S. G., 1997, "Experimental investigation and flow visualization of the resin-transfer mold-filling process in a non-planar geometry," *Composites Science and Technology*, **57**, pp. 23-33.

Binetruy, C., Hilaire, B., and Pabiot, J., 1998, "Tow impregnation model and void formation mechanisms during RTM," *Journal of Composite Materials*, **32**(3), pp. 223-245.

Boomsma, K., and Poulikakos, D., 2001, "On the effective thermal conductivity of a three-dimensionally structured fluid-saturated metal foam," *International Journal of Heat and Mass Transfer*, **44**(4), pp. 827-836.

Brackbill, J. U., Kothe, D. B., and Zemach, C., 1992, "A continuum method for modeling surface tension," *Journal of Computational Physics,* **100**, pp. 335-354.

Breard, J., Saouab, A., and Bouquet, G., 2003, "Numerical simulation of void formation in LCM," *Composites Part A*, **34**, pp. 517-523.

Brent, A. D., Voller, V. R., and Reid, K. J., 1988, "Enthalpy-porosity technique for modelling convection-diffusion phase change: application to the melting of a pure metal," *Numerical Heat Transfer Part A*, **13**(3), pp. 297-318.

Broesch, D. J., and Frechette, J., 2012, "From concave to convex: capillary bridges in slit pore geometry," *Langmuir,* **28**, pp. 15548-15554.

Cabeza, L. F., Mehling, H., Hiebler, S., and Ziegler, F., 2002, "Heat transfer enhancement in water when used as PCM in thermal energy storage," *Applied Thermal Engineering*, **22**(10), pp. 1141-1151.

Chan, A. W., and Morgan, R. J., 1992, "Modeling perform impregnation and void formation in resin transfer molding of unidirectional composites," *SAMPE Quarterly*, **23**(3), pp. 48-52.

Chebbi, R., 2007, "Dynamic of liquid penetration into capillary tubes," *Journal of Colloid and Interface Science*, **315**, pp. 255-260.

Crank, J., 1984, *Free and Moving Boundary Problems*, Oxford University Press, Oxford, UK.

Coursey, J. S., Kim, J. and Boudreaux, P. J., 2005, "Performance of graphite foam evaporator for use in thermal management," *Journal of Electronic Packaging*, **127**(2), pp. 127-134.

Coussy, O., 2010, *Mechanics and Physics of Porous Solids*, Wiley, UK.

Cui, Y., Liu, C., Hu. S. and Yu, X., 2011, "The experimental exploration of carbon nanofiber and carbon nanotube additives on thermal behavior of phase change materials," *Solar Energy Materials and Solar Cells*. **95**(4), pp. 1208-1212.

DeGroot, C. T. and Straatman, A. G., 2012, "Numerical results for the effective flow and thermal properties of idealized graphite foam," *Journal of Heat Transfer*, **134**(4), pp. 042603-1–12.

Delker, T., Pengra, D. B., and Wong P., 1996, "Interface pinning and the dynamics of capillary rise in porous media," *Physical Review Letters*, **76**(16), pp. 2902-2905.

Dendy, E. D., Padial-Collins, N. T., and Vander Heyden, W. B., 2002, "A general-purpose finite-volume advection scheme for continuous and discontinuous fields on unstructured grids," *Journal of Computational Physics*, **180**, pp. 559-583.

Diakaki, C., Grigoroudis, E., and Kolokotsa, D., 2008, “Towards a multi-objective optimization approach for improving energy efficiency in buildings,” *Energy and Buildings*, **40**(9), pp. 1747-1754.

Dimitrovova, Z., and Advani, S. G., 2004, “Mesolevel analysis of the transition region formation and evolution during the liquid composite molding process,” *Computers and Structures*, **82**(17), pp. 1333-1347.

Dube, M., Majaniemi, S., Rost, M., Alava, M. J., Elder, K. R., and Ala-Nissila, T., 2001, “Interface pinning in spontaneous imbibition,” *Physical Review E*, **64**(5), pp. 051605-1–6.

Fan, L., and Khodadadi, J. M., 2011, “Thermal conductivity enhancement of phase change materials for thermal energy storage: A review” *Renewable Sustainable Energy Reviews*, **15**(1), pp. 24-46.

Farid, M. M., Khudhair, A. M., Razack, S. A. K., and Al-Hallaj, S., 2004, “A review on phase change energy storage: materials and applications,” *Energy Conversion and Management*, 45(9), pp. 1597–1615.

Fukai, J., Hamada, Y., Morozumi, Y. and Miyatake, O., 2002, “Effect of carbon-fiber brushes on conductive heat transfer in phase change materials,” *International Journal of Heat and Mass Transfer*, **45**(24), pp. 4781-4792.

Gaies, D. and Faber, K. T., 2002, “Thermal properties of pitch-derived graphite foam,” *Carbon*, **40**(7), pp. 1131-1150.

Gandikota, V. and Fleischer, A. S., 2009, “Experimental investigation of the thermal performance of graphite foam for evaporator enhancement in both pool boiling and an FC-72 thermosyphon,” *Heat Transfer Engineering*, **30**(8), pp. 643–648.

Gao, J. W., Zheng, R. T., Ohtani, H., Zhu, D. S., and Chen, G., 2009, "Experimental investigation of heat conduction mechanisms in nanofluids. Clue on clustering," *Nano letters*, **9**(12), pp. 4128-4132.

Gerlach, D., Tomar, G., Biswas, G., and Durst, F., 2006, "Comparison of volume-of-fluid methods for surface tension-dominant two-phase flows," *International Journal of Heat and Mass Transfer*, **49**(3), pp. 740-754.

Gharagozloo, P. E., and Goodson, K. E., 2010, "Aggregate fractal dimensions and thermal conduction in nanofluids," *Journal of Applied Physics*, **108**(7), pp. 074309-074309.

Gourichon, B., Binetruy, C., and Krawczak, P., 2006, "A new numerical procedure to predict dynamic void content in liquid composite molding," *Composites Part A*, **37**(11), pp. 1961-1969.

Gourichon, B., Deleglise, M., Binetruy, C., and Krawczak, P., 2008, "Dynamic void content prediction during radial injection in liquid composite molding," *Composites Part A*, **39**(1), pp. 46-55.

Harlow, F. H., and Welch, J. E., 1965, "Numerical Calculation of Time-Dependent Viscous Incompressible Flow of Fluid with Free Surface," *Physics of Fluids*, **8**, pp. 2182-2189.

Haynes, W. M., and Lide, D. R., 2010, *Handbook of chemistry and physics*, National Institute for Standards and Technology, CRC Press, New York, NY.

Hernandez-Ortega, J. J., Zamora, R., Palacios, J., Lopez, J., and Faura F., 2010, "An experimental and numerical study of flow patterns and air entrapment phenomena during the filling of a vertical die cavity," *Journal of Manufacturing Science and Engineering*, **132**(5), pp. 051011-1–9.

Hilpert, M., 2009, “Effects of dynamic contact angle on liquid infiltration into inclined capillary tubes: (Semi)-analytical solutions,” *Journal of Colloid and Interface Science*, **337**(1), pp. 138-144.

Hilpert M., 2010, “Explicit analytical solutions for liquid infiltration into capillary tubes: dynamic and constant contact angle,” *Journal of Colloid and Interface Science*, **344**(1), pp. 198-208.

Hilpert, M., and Ben-David, A., 2009, “Infiltration of liquid droplets into porous media: Effects of dynamic contact angle and contact angle hysteresis,” *International Journal of Multiphase Flow*, **35**(3), pp. 205-218.

Hirt, C. W., and Nichols, B. D., 1981, “Volume of fluid (VOF) method for the dynamics of free boundaries,” *Journal of Computational Physics*, **39** (1), pp. 201-225.

Hsu, C. T., and Yeh, K. C., 2002, “Iterative explicit simulation of 1D surges and dam-break flows,” *International Journal for Numerical Methods in Fluids*, **38**(7), pp. 647-675.

Hutchins, J. and Marschall, E., 1989, “Pseudosteady-state natural convection heat transfer inside spheres,” *International Journal of Heat and Mass Transfer*, **32**(11), pp. 2047-2053.

James, L., Austin, S., Moore, C. A., Stephens, D., Walsh, K. K. and Dale Wesson, G., 2010, “Modeling the principle physical parameters of graphite carbon foam,” *Carbon*, **48**(9), pp. 2418-2424.

Jegadheeswaran, S., and Pohekar, S. D., 2009, “Performance enhancement in latent heat thermal storage system: A review,” *Renewable and Sustainable Energy Reviews*, **13**(9), pp. 2225-2244.

Jennings, S. G., 1988, “The mean free path in air,” *Journal of Aerosol Science*, **19**(2), pp. 159-166.

Jin, L. W., Leong, K. C. and Pranoto, I., 2011, "Saturated pool boiling heat transfer from highly conductive graphite foams," *Applied Thermal Engineering*, **31**(14), pp. 2685-2693.

Jin, L. W., Leong, K. C., Pranoto, I., Li, H.Y. and Chai, J.C., 2011, "Experimental study of a two-phase thermosyphon with porous graphite foam insert," *Thermal Science and Engineering Applications*, **3**(2), pp. 024502-1–6.

Kang, M. K., Lee, W. I., and Hahn, H. T., 2000, "Formation of microvoids during resin-transfer molding process," *Composites Science and Technology*, **60**(12), pp. 2427-2434.

Kassemi, M., Barsi, S., Kaforey, M., and Matthiesen, D., 2001, "Effect of void location on segregation patterns in microgravity solidification," *Journal of Crystal Growth*, **225**(2), pp. 516-521.

Khodadadi, J. M., Fan, L., and Babaei, H., 2013, "Thermal conductivity enhancement of nanostructure-based colloidal suspensions utilized as phase change materials for thermal energy storage: A review," *Renewable and Sustainable Energy Reviews*, **24**, pp. 418-444.

Khodadadi, J. M., and Hosseinizadeh, S. F., 2007, "Nanoparticle-enhanced phase change materials (NEPCM) with great potential for improved thermal energy storage", *International Communications in Heat and Mass Transfer*, **34**(5), pp. 534-543.

Khodadadi, J. M., and Zhang, Y., 2000, "Effects of thermocapillary convection on melting within droplets," *Numerical Heat Transfer Part A*, **37**(2), pp. 133-153.

Klett, J. W., 2000, "Process for making carbon foam," United States Patent No. 6,033,506.

Klett, J. W., Hardy, R., Romine, E., Walls, C., and Burchella, T., 2000, "High-thermal-conductivity, mesophase-pitch-derived carbon foams: effect of precursor on structure and properties," *Carbon*, **38**(7), pp. 953-973.

Klett, J. W., McMillan, A. D., Gallego, N. C., and Walls, C., 2004, "The role of structure on the thermal properties of graphitic foams," *Journal of Materials Science*, **39**(11), pp. 3659-3676.

Koplik, J., and Levine, H., 1985, "Interface moving through a random background," *Physical Review B*. **32**(1), pp. 280-292.

Krishnan, S., Garimella, S. V., and Murthy, J. Y., 2008, "Simulation of thermal transport in open-cell metal foams: effect of periodic unit-cell structure," *Journal of Heat Transfer*, **130**(2), pp. 24503-1-5.

Krishnan, S., Murthy, J. Y., and Garimella, S. V., 2006, "Direct simulation of transport in open-cell metal foam," *Journal of Heat Transfer*, **128**(8), pp. 793-799.

Lafdi, K., Mesalhy, O., and Elgafy, A., 2008, "Graphite foam infiltrated with phase change materials as alternative materials for space and terrestrial thermal energy storage applications," *Carbon*, **46**(1), pp. 159-168.

Landeryou, M., Eames, I., and Cottenden, A., 2005, "Infiltration into inclined fibrous sheets," *Journal of Fluid Mechanics*, **529**, pp. 173-193.

Lee, D. H., Lee, W. I., and Kang, M. K., 2006, "Analysis and minimization of void formation during resin transfer molding process," *Composites Science and Technology*, **66**(16), pp. 3281-3289.

Leong, K. C. and Li, H. Y., 2011, "Theoretical study of the effective thermal conductivity of graphite foam based on a unit cell model," *International Journal of Heat and Mass Transfer*, **54**(25), pp. 5491-5496.

Leong, K. C., Li, H. Y., Jin, L. W. and Chai, J. C., 2010, "Numerical and experimental study of forced convection in graphite foams of different configurations," *Applied Thermal Engineering*, **30**(5), pp. 520-532.

Lin, W., Sunden, B. and Yuan, J., 2013, “A performance analysis of porous graphite foam heat exchangers in vehicles,” *Applied Thermal Engineering*, **50**(1), pp. 1201-1210.

Liu, M., Saman, W., and Bruno, F., 2012, “Review on storage materials and thermal performance enhancement techniques for high temperature phase change thermal storage systems,” *Renewable and Sustainable Energy Reviews*, **16**(4), 2118-2132.

Liu, A., Voth, T. E., and Bergman, T. L., 1993, “Pure material melting and solidification with liquid phase buoyancy and surface tension forces,” *International Journal of Heat and Mass Transfer*, **36**(2), pp. 411-422.

Lopez, J., and Hernandez, J., 2008, “Analytical and geometrical tools for 3D volume of fluid methods in general grids,” *Journal Computational Physics*, **227**(12), pp. 5939-5948.

Lund, H., 2007, “Renewable energy strategies for sustainable development,” *Energy*, **32**(6), pp. 912-919.

Maggi, F., and Alonso-Marroquin, F., 2012, “Multiphase capillary flows,” *International Journal of Multiphase Flow*, **42**, pp. 62-73.

Mahale, A. D., Prud’homme, R. K., and Rebenfeld, L., 1992, “Quantitative measurement of voids formed during liquid impregnation of nonwoven multifilament glass networks using an optical visualization technique,” *Polymer Engineering and Science*, **32**(5), pp. 319-326.

Marin, J. M., Zalba, B., Cabeza, L. F., and Mehling, H., 2005, “Improvement of a thermal energy storage using plates with paraffin-graphite composite,” *International Journal of Heat and Mass Transfer*, **48**(12), pp. 2561-2570.

Markicevic, B., Hoff, K., Li, H., Zand, A. R., and Navaz, H. K., 2012, “Capillary force driven primary and secondary unidirectional flow of wetting liquid into porous medium,” *International Journal of Multiphase Flow*, **39**, pp. 193-204.

Matsunaga, K., and Kawamura, H., 2006, "Influence of thermocapillary convection on solid-liquid interface," *Fluid Dynamics and Materials Processing*, **2**(1), pp. 59-64.

Mehling, H., Hiebler, S., and Ziegler, F., 2000, "Latent heat storage using a PCM-graphite composite material," *Proceedings of Terrastock 2000*, August 28-September 1, Stuttgart, Germany, pp. 375-380.

Mehrabian, H., Gao, P., and Feng, J. J., 2011, "Wicking flow through microchannels," *Physics of Fluids*, **23**(12), pp. 122108-1–14.

Mesalhy, O., Lafdi, K., Elgafy, A., and Bowman, K., 2005, "Numerical study for enhancing the thermal conductivity of phase change material (PCM) storage using high thermal conductivity porous matrix," *Energy Conversion and Management*, **46**(6), pp. 847-867.

Mesalhy, O., Lafdi, K. and Elgafy, A., 2006, "Carbon foam matrices saturated with PCM for thermal protection purposes," *Carbon*, **44**(10), pp. 2080-2088.

Mills, A., Farid, M., Selman, J. R., and Al-Hallaj, S., 2006, "Thermal conductivity enhancement of phase change materials using a graphite matrix," *Applied Thermal Engineering*, **26**(14), pp. 1652-1661.

Moeini Sedeh, M., and Khodadadi, J. M., 2012, "Effect of voids on solidification of phase change materials infiltrated in graphite foams," Paper No. HT2012-58405, *Proceedings of the ASME 2012 Summer Heat Transfer Conference*, July 8-12, Rio Grande, Puerto Rico.

Moeini Sedeh, M., and Khodadadi, J. M., 2013A, "Energy efficiency improvement and fuel savings in water heaters using baffles," *Applied Energy*, **102**, pp. 520-533.

Moeini Sedeh, M., and Khodadadi, J. M., 2013B, "Thermal conductivity improvement of phase change materials/graphite foam composites," *Carbon*, http://dx.doi.org/10.1016/j.carbon.2013.04 .004.

Moeini Sedeh, M., and Khodadadi, J. M., 2013C, "Interface behavior and void formation during infiltration of liquids into porous structures," *International Journal of Multiphase Flow*, under review.

Moeini Sedeh, M., and Khodadadi, J. M., 2013D, "Experimental investigation of wicking flow through a porous medium as a validation approach for numerical simulations," Paper No. FEDSM2013-16466, *Proceedings of the ASME 2013 Fluids Engineering Summer Meeting (FEDSM2013)*, July 7-11, 2013, Incline Village, Nevada, USA.

Narayan, O., and Fisher, D. S., 1993, "Threshold critical dynamics of driven interfaces in random media," *Physical Review B*. **48**(10), pp. 7030-7042.

Nayak, K. C., Saha, S. K., Srinivasan, K., and Dutta, P., 2006, "A numerical model for heat sinks with phase change materials and thermal conductivity enhancers," *International Journal of Heat and Mass Transfer*, **49**(11), pp. 1833-1844.

Nota, F., Savino, R., and Fico, S., 2006, "The interaction between droplets and solidification front in presence of Marangoni effect," *Acta Astronautica*, **59**(1), pp. 20-31.

Oro, E., de Gracia, A., Castell, A., Farid, M. M. and Cabeza L. F., 2012, "Review on phase change materials (PCMs) for cold thermal energy storage applications," *Applied Energy*, **99**, pp. 513-533.

Osher, S., and Sethian, J. A., 1988, "Fronts propagating with curvature-dependent speed: Algorithms based on Hamilton-Jacobi formulations," *Journal of Computational Physics*, **79**(1), pp. 12-49.

Ozmen-Cagatay, H., and Kocaman, S., 2011, "Dam-Break Flow in the Presence of Obstacle: Experiment and CFD Simulation," *Engineering Applications of Computational Fluid Mechanics*, **5**(4), pp. 541-552.

Panwar, N. L., Kaushik, S. C., and Kothari, S., 2011, "Role of renewable energy sources in environmental protection: A review," *Renewable and Sustainable Energy Reviews*, **15**(3), pp. 1513-1524.

Park, C. H., Lebel, A., Saouab, A., Breard, J., and Lee, W.I., 2011, "Modeling and simulation of voids and saturation in liquid composite molding processes," *Composites Part A*, **42**(6), pp. 658-668.

Patel, N., Rohatgi, V., and James Lee, L., 1995, "Micro scale flow behavior and void formation mechanism during impregnation through a unidirectional stitched fiberglass mat," *Polymer Engineering and Science*, **35**(10), pp. 837-851.

Peterson, R. C., and Robertson, R. E., 1991, "Flow characteristics of polymer resin through glass fiber preforms in resin transfer molding," *Advanced composite materials: new developments and applications: proceedings of the Seventh Annual ASM/ESD Advanced Composites Conference*, September 30-October 3, Detroit, Michigan, USA, pp. 203-208.

Pilliod Jr., J. E., and Puckett, E. G., 2004, "Second-order accurate volume-of-fluid algorithms for tracking material interfaces," *Journal of Computational Physics*, **199**(2), pp. 465-502.

Poco Graphite Inc., 2012, "PocoFoam typical material properties," Decatur, TX, http://www.poco.com/Portals/0/Literature/Semiconductor/78962v2PocoFoamFlyer.pdf (accessed May 2013).

Popli, S., Rodgers, P., and Eveloy, V., 2012, "Trigeneration scheme for energy efficiency enhancement in a natural gas processing plant through turbine exhaust gas waste heat utilization," *Applied Energy*, **93**, pp. 624-636.

Py, X., Olives, R. and Mauran, S., 2001, “Paraffin/porous-graphite-matrix composite as a high and constant power thermal storage material,” *International Journal of Heat and Mass Transfer*, **44**(14), pp. 2727-2737.

Rohatgi, V., Patel, N., and James Lee, L., “1993, Macro and Microvoid formation in liquid composite molding,” Advanced composites technologies: proceedings of the 9th Annual ASM/ESD Advanced Composites Conference, November 8-11, Dearborn, Michigan, USA, pp. 81-98.

Saha, A. A., and Mitra S. K., 2009, “Effect of dynamic contact angle in a volume of fluid (VOF) model for a microfluidic capillary flow,” *Journal of Colloid and Interface Science*, **339**(2), pp. 461-480.

Sari, A., and Karaipekli, A. 2007, “Thermal conductivity and latent heat thermal storage characteristics of paraffin/expanded graphite composite as phase change material,” *Applied Thermal Engineering*, **27**(8), pp. 1271-1277.

Schell, J. S. U., Deleglise, M., Binetruy, C., Krawczak, P., and Ermanni, P., 2007, “Numerical prediction and experimental characterisation of meso-scale-voids in liquid composite moulding,” *Composites Part A*. **38**(12), pp. 2460-2470.

Sengers, J., V., and Watson, J. T. R., 1986, “Improved international formulations for the viscosity and thermal conductivity of water substance,” *Journal of Physical Chemistry Reference Data*, **15**(4), pp. 1291-1314.

Shatikian, V., Ziskind, G., and Letan, R., 2005, “Numerical investigation of a PCM-based heat sink with internal fins,” *International Journal of Heat and Mass Transfer*, **48**(17), pp. 3689-3706.

Shen, Y. C., Lin, G. T., Li, K. P., and Yuan, B. J., 2010, "An assessment of exploiting renewable energy sources with concerns of policy and technology," *Energy Policy*, **38**(8), pp. 4604-4616.

Silva, A. A., Reis, R. A., and Paredes, M. L. L., 2009, "Density and Viscosity of Decalin, Cyclohexane, and Toluene Binary Mixtures at (283.15, 293.15, 303.15, 313.15, and 323.15) K," *Journal of Chemical Engineering Data*. **54**(7), pp. 2067-2072.

Simacek, P., and Advani, S. G., 2003, "A numerical model to predict fiber tow saturation during liquid composite molding," *Composites Science and Technology*, **63**(12), pp. 1725-1736.

Sharma, A., Tyagi, V. V., Chen, C. R., and Buddhi, D., 2009, "Review on thermal energy storage with phase change materials and applications," *Renewable and Sustainable Energy Reviews*, **13**(2), pp. 318-345.

Soukane, S., and Trochu, F., 2006, "Application of the level set method to the simulation of resin transfer molding," *Composites Science and Technology*, **66**(7), pp. 1067-1080.

Spaid, A. A. M., and Phelan Jr, F. R., 1998, "Modeling void formation dynamics in fibrous porous media with the lattice Boltzmann method," *Composites Part A*, **29**(7), pp. 749-755.

Stansby, P. K., Chegini, A., and Barnes, T. C. D., 1998, "The initial stages of dam-break flow," *Journal of Fluid Mechanics*, **374**(1), pp. 407-424.

Sui, Y., and Spelt, P. D. M., 2011, "Sustained inertial-capillary oscillations and jet formation in displacement flow in a tube," *Physics of Fluids*, **23**(12), pp. 122104-1–11.

Sulfredge, C. D., Chow, L. C., and Tagavi, K. A., 1999, "Initiation and growth of solidification shrinkage voids," *Annual Reviews of Heat Transfer*, **10**, Chapter 6, pp. 221-278, Begell House, Inc.

Sultan, K., DeGroot, C. T., Straatman, A. G., Gallego, N. C. and Jangan, H., 2009, "Thermal characterization of porous graphitic foam – Convection in impinging flow," *International Journal of Heat and Mass Transfer*, **52**(19), pp. 4296-4301.

Sussman, M., and Puckett, E. G., 2000, "A coupled level set and volume-of-fluid method for computing 3D and axisymmetric incompressible two-phase flows," *Journal of Computational Physics*, **162**(2), pp. 301-337.

Tong, X., Khan, J. A., and Amin, M. R., 1996, "Enhancement of heat transfer by inserting a metal matrix into a phase change material," *Numerical Heat Transfer, Part A*, **30**, pp. 125-141.

Tritt, T. M., 2004, *Thermal conductivity: theory, properties and applications*, Kluwer Academic/ Plenum Publishers, New York, NY.

Tuzovskaya, I., Pacheco Benito, S., Chinthaginjala, J. K., Reed, C., Lefferts, L. and van der Meer, T., 2012, "Heat exchange performance of stainless steel and carbon foams modified with carbon nano fibers," *International Journal of Heat and Mass Transfer*, **55**(21-22), pp. 5769-5776.

Ubbink, O., and Issa, R. I., 1999, "A method for capturing sharp fluid interfaces on arbitrary meshes," *Journal of Computational Physics*, **153**(1), pp. 26-50.

US EIA, 2012, "Annual energy review 2011," *Energy Information Administration*, US Department of Energy: Washington, DC, www.eia.doe.gov/emeu/aer (accessed May 2013).

Van Wylen, G. J., Sonntag, R. E., and Borgnakke, C., 1994, *Fundamentals of Classical Thermodynamics*, Wiley, New York, NY.

Voller, V. R., Brent, A. D., and Prakash, C., 1989, "The modeling of heat, mass and solute transport in solidification systems," *International Journal of Heat and Mass Transfer*, **32**(9), pp. 1719-1731.

Voller, V. R., Cross, M., and Markatos, N. C., 1987, "An enthalpy method for convection/ diffusion phase change," *International Journal of Numerical Methods in Engineering*, **24**(1), pp. 271-284.

Voller, V. R., and Prakash, C., 1987, "A fixed grid numerical modeling methodology for convection-diffusion mushy region phase-change problems," *International Journal of Heat and Mass Transfer*, **30**(8), pp. 1709-1719.

Wacławczyk, T. and Koronowicz, T., 2008, "Comparison of CICSAM and HRIC high-resolution schemes for interface capturing," *Journal of Theoretical and Applied Mechanics*, **46**(2), pp. 325-345.

Wang, L. W., Metcalf, S. J., Critoph, R. E., Thorpe, R. and Tamainot-Telto, Z., 2011, "Thermal conductivity and permeability of consolidated expanded natural graphite treated with sulphuric acid," *Carbon*, **49**(14), pp. 4812-4819.

Wang, X. Q., and Mujumdar, A.S., 2007, "Heat transfer characteristics of nanofluids: a review," *International Journal of Thermal Sciences*, **46**, pp. 1-19.

Wang, Z., Yang, J., and Stern, F., 2012, "A new volume-of-fluid method with a constructed distance function on general structured grids," *Journal of Computational Physics*, **231**(9), pp. 3703-3722.

Washburn, E. W., 1921, "The dynamics of capillary flow," *Physical Review*, **17**(3), pp. 273-283.

Weymouth, G. D., and Yue, D. K.-P., 2010, "Conservative Volume-of-Fluid method for free-surface simulations on Cartesian-grids," *Journal of Computational Physics*, **229**(8), pp. 2853-2865.

Williams, Z. A. and Roux, J. A., 2006, "Graphite foam thermal management of a high packing density array of power amplifiers," *Journal of Electronic Packaging*, **128**(4), pp. 456-465.

Xia, L., Zhang, P. and Wang, R. Z., 2010, "Preparation and thermal characterization of expanded graphite/paraffin composite phase change material," *Carbon*, **48**(9), pp. 2538-2548.

Yamaleev, N., and Mohan, R., 2006, "Effect of the phase transition on intra-tow flow behavior and void formatiFon in liquid composite molding," *International Journal of Multiphase Flow*. **32**, pp. 1219-1233.

Yang, X., James, A. J., Lowengrub, J., Zheng, X., and Cristini, V., 2006, "An adaptive coupled level-set/volume-of-fluid interface capturing method for unstructured triangular grids," *Journal of Computational Physics*, **217**(2), pp. 364-394.

Yadav, A., Kumar, R., Bhatia, G. and Verma, G. L., 2011, "Development of mesophase pitch derived high thermal conductivity graphite foam using a template method," *Carbon*, **49**(11), pp. 3622-3630.

Yaws, C. L., 2008, *Thermophysical Properties of Chemicals and Hydrocarbons*, First edition, William Andrew, New York, NY.

Yu, Q., Thompson, B. E. and Straatman, A. G., 2006, "A unit cube-based model for heat transfer and fluid flow in porous carbon foam," *Journal of Heat Transfer*, **128**(4), pp. 352-360.

Yu, Q., Straatman, A. G. and Thompson, B. E., 2006, "Carbon-foam finned tubes in air–water heat exchangers," *Applied Thermal Engineering*, **26**(2), pp. 131-143.

Zheng, R., Gao, J., Wang, J., and Chen, G., 2011, “Reversible temperature regulation of electrical and thermal conductivity using liquid–solid phase transitions,” *Nature communications*, **2**, pp. 289-1–6.

Zhong, Y., Guo, Q., Li, S., Shi, J. and Liu, L., 2010, “Heat transfer enhancement of paraffin wax using graphite foam for thermal energy storage,” *Solar Energy Materials and Solar Cells*, **94**(6), pp. 1011–1014.

Zhong, Y., Li, S., Wei, X., Liu, Z., Guo, Q., Shi, J. and Liu, L., 2010, “Heat transfer enhancement of paraffin wax using compressed expanded natural graphite for thermal energy storage,” *Carbon*, **48**(1), pp. 300-304.

Appendix A Verification of the VOF Method Incorporated in the Fluent Package

Before conducting the numerical simulations of infiltration for wetting and non-wetting liquids, the results of computations based on the VOF method incorporated in the Fluent package were verified. For this purpose, a classic case previously studied and available in literature, was selected and simulated using the VOF method. The results of the simulations were compared against the available data in the literature obtained using different methods to assess agreement in predicting the flow characteristics. The pertinent details are presented in this appendix.

The dam-break problem was studied by a number of researchers using different numerical and experimental methods to understand the behavior of water and flooding waves upon breaking a dam. A classic two-dimensional model, proposed for this problem, consists of water with high depth behind a vertical wall (upstream) with a shallow water layer downstream, as the initial state, as shown in figure A.1a. Upon breaking the dam, the body of water discharges freely and floods toward downstream. There are numerous papers in literature focusing on the behavior of water in this system, flooding waves, pressure variation, resulting forces, and spatial and time domain of flooding after breaking the dam. However, for assessing the accuracy of the solver and verification purposes, the initial stages of dam-break flow was considered here and compared to the reported experimental results in the literature.

The experimental studies (Stansby et al., 1998; Ozmen-Cagatay and Kocaman, 2011) indicate that a breaking wave is created at the initial stages of dam-break moving toward downstream. Similarly, the proposed model and the VOF approach used in this study, show the

evolution of a wave traveling downstream in agreement with previous findings, as shown in figure A.1. While, preliminary work in this field (such as the marker and cell method by Harlow and Welch, 1965) cannot give the details of wave formation and propagation, some simplified models and solutions, proposed previously such as 1D surge flows (Hsu and Yeh, 2002), can predict a jump in water front; however, such models cannot precisely predict the shape and evolution of the wave. Furthermore, the problem of dam-break was studied by Abdolmaleki et al. (2004) using the VOF method. Comparing the obtained numerical results with the experimental measurements, they reported good agreement between the results as verification of VOF method in the Fluent package.

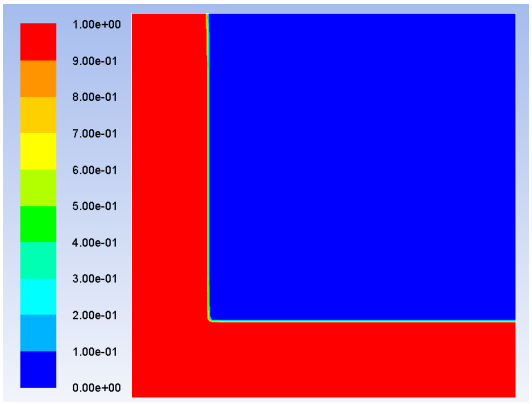

(a) t=0 sec, initial conditions

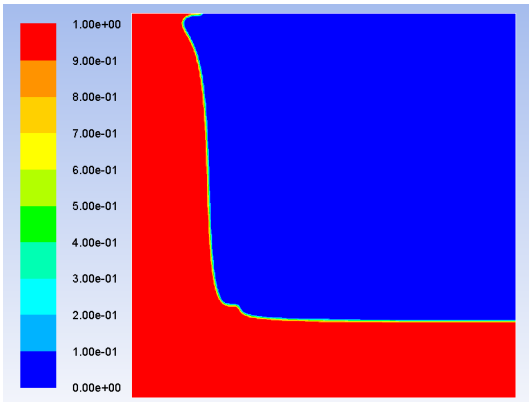

(b) t=0.01 sec

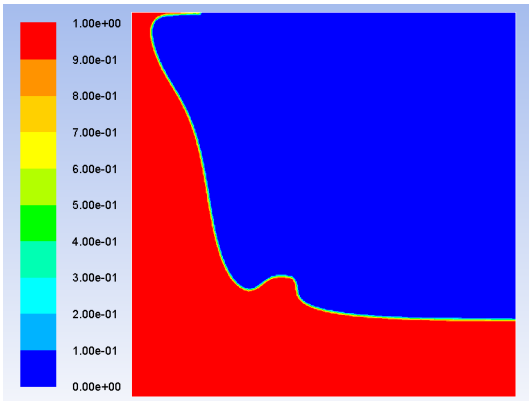

(c) t=0.02 sec

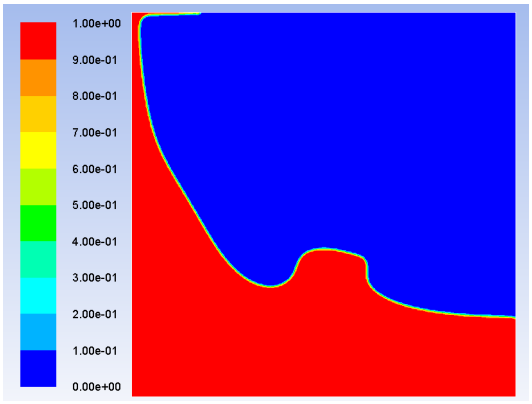

(d) t=0.03 sec

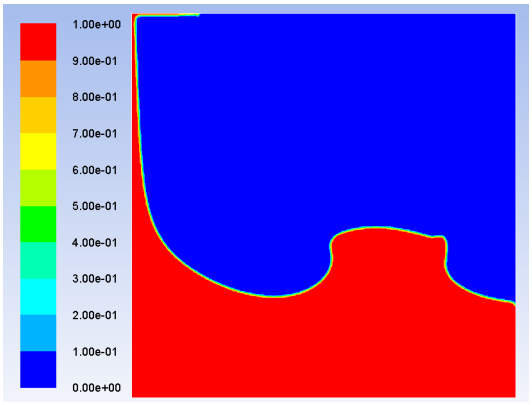

(e) t=0.04 sec

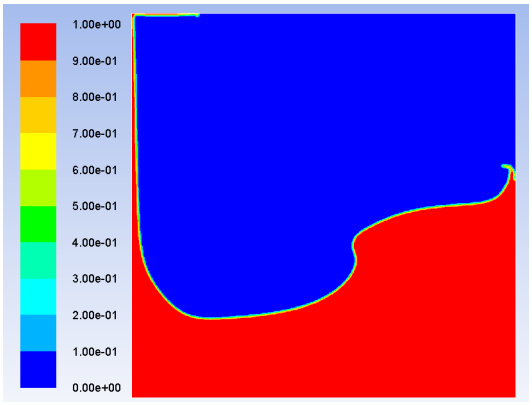

(f) t=0.05 sec

Figure A.1 Evolution of the wave in the initial stages of the dam-break flow at selected time instants of (a) t=0 sec, initial state, (b) t=0.01 sec, (c) t=0.02 sec, (d) t=0.03 sec, (e) t=0.04 sec, (f) t=0.05 sec (water is in red color, while air is in blue).

Appendix B Verification of Volume-Change during Phase Change using Combined VOF and Enthalpy-Porosity Method

A combination of the VOF and enthalpy-porosity methods was proposed in chapter 3 for the investigation of phase change processes in presence of voids within the pores of a porous structure. It was mentioned that the proposed method is capable of predicting the volume-change, resulting from the variation of the density during the solidification and melting processes. Since there are contributing effects from the presence of void and interfacial effects in the original analysis at pore-level, it is necessary to verify the capability of the proposed method in predicting the volume-change during phase change. In this appendix, a numerical simulation of solidification was conducted for water in a two-dimensional cavity with the purpose of verifying the volume-change during the freezing process. The interfacial effects are not present due to the scale of the problem and combined VOF and enthalpy porosity method was used for the simulation as described in chapter 3.

The density of ice/water was considered as a function of temperature over the range of applied thermal conditions, as shown in figure B.1 (Haynes and Lide, 2010). The density of solid (ice) was constant (915 kg/m^3 below 273.0 K), while it was considered as a function of temperature for liquid phase and in mushy zone. The density varies linearly with temperature in mushy zone (from 273.0 K to 273.15 K). The variation of density accounts for the ensuing volume changes in the form of contraction or expansion during the phase change processes between the liquid and solid phases. For water, as an anomaly, the density of ice is less than that

of liquid (as given in figure B.1), leading to its expansion during freezing. The density varies from 999.84 kg/m^3 in liquid state to 915 kg/m^3 in solid state (ice), resulting a theoretical volume expansion of 9.29% for water during the freezing process. The density varies with temperature in liquid phase (from 999.84 kg/m^3 at 273.15 K to 999.965 kg/m^3 at 276 K), although its variation is very small compared to density variation during the phase change. Furthermore, the viscosity and thermal conductivity of water were defined as functions of temperature over the considered temperature range (Van Wylen et al., 1994; Sengers and Watson, 1986).

The two-dimensional model for simulating this problem was developed as a square cavity partially filled with water (60%), while air filled the rest of the cavity at the top as shown in figure B.2a. The applied thermal boundary conditions on the four walls are given in figure B.2b and the initial temperature of water and air within the cavity was set to be 275 K. Employing the combined VOF and enthalpy-porosity method, the freezing process was simulated and the relevant details were obtained. The evolving contours of liquid fraction during freezing of water are given at selected time instants in figure B.3. Solidification is initially driven by conduction heat transfer (for $t < 15$ sec) and water freezes next to the bottom and side walls of the cavity. However, after $t = 15$ sec, convection patterns appear in the liquid due to anomalous density variation of water, as it is observed in figure B.3.

A comparison of initial and final states of solidification is given in figure B.4 and reveals that the final volume of frozen water (ice) is higher than the initial volume of water in the square cavity. The final volume of ice in the cavity was evaluated to be 65.44% of the cavity, which in comparison with 60% initial volume of water yields a volume expansion of 9.07% during the phase change for water. The obtained volume expansion of 9.07% is in good agreement with the theoretical volume expansion of 9.29% (with a deviation of 2.37%). As a result, the proposed

method (combined VOF and enthalpy-porosity) is capable of predicting volume-change (expansion or shrinkage) during the phase change processes (solidification and melting). Furthermore, the contours of density during the solidification of water are shown in figure B.5, representing the prevailing natural convection patterns and the variation of density during the freezing of water within the cavity.

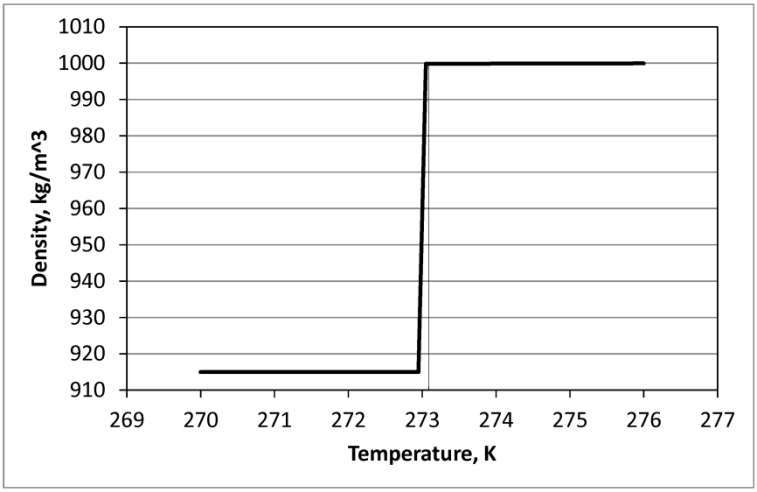

Figure B.1 Density of water/ice as a function of temperature, considering the phase change process from 273.15 K (liquidus temperature) to 273.0 K (solidus temperature).

(a)

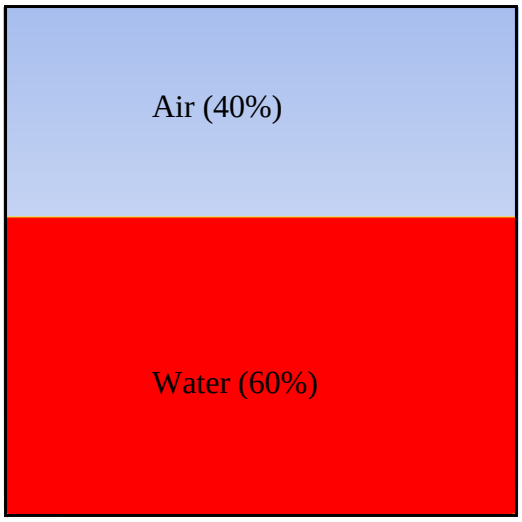

(b)

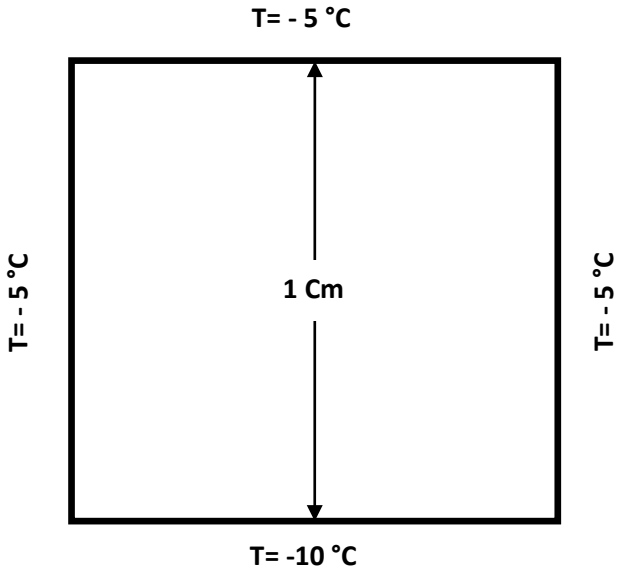

Figure B.2 (a) Two-dimensional model of water freezing and contributing phases, and (b) Thermal conditions applied to the model (2D square cavity).

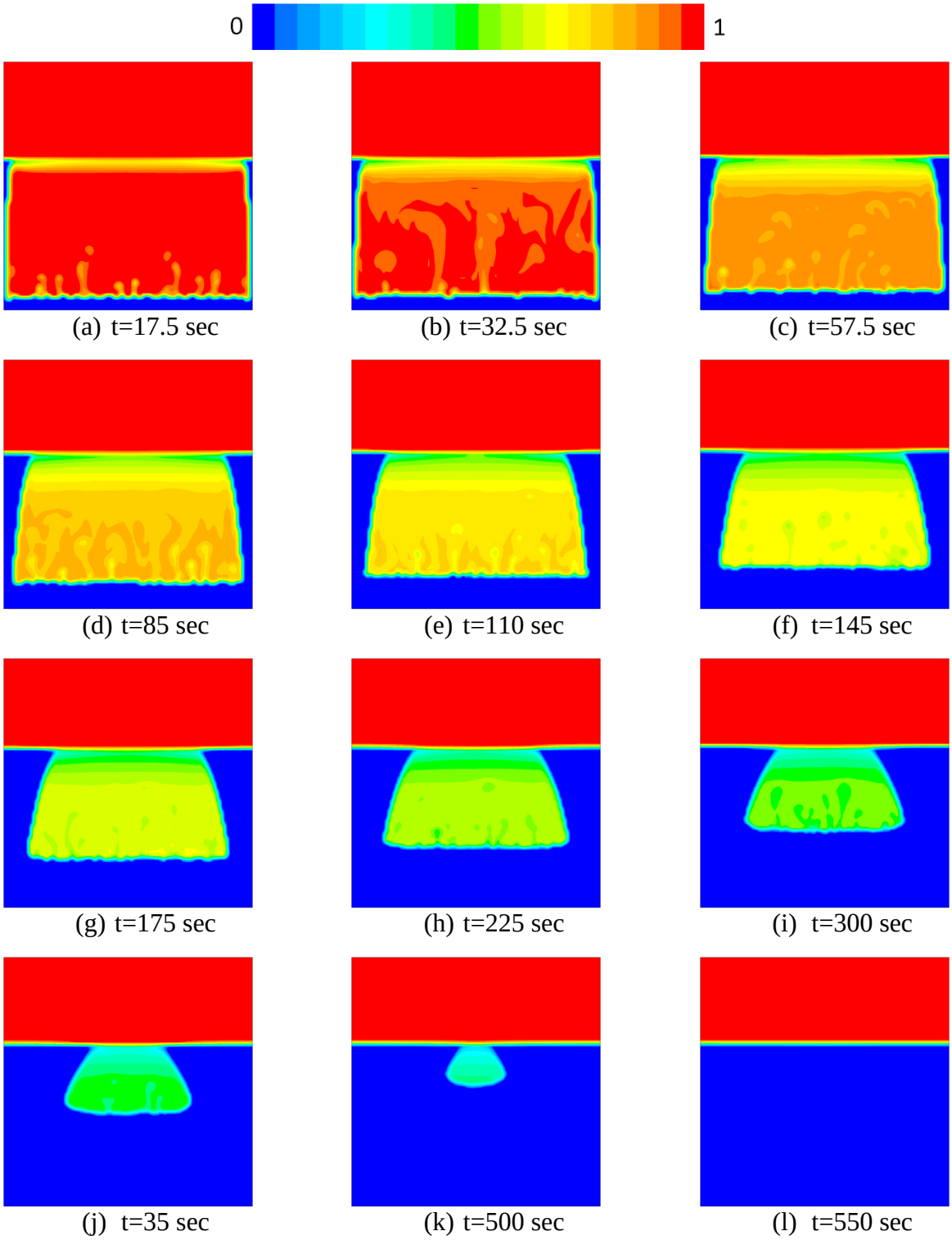

Figure B.3 Evolving contours of liquid fraction during freezing of water at selected time instants (liquid is in red while ice is in blue color).

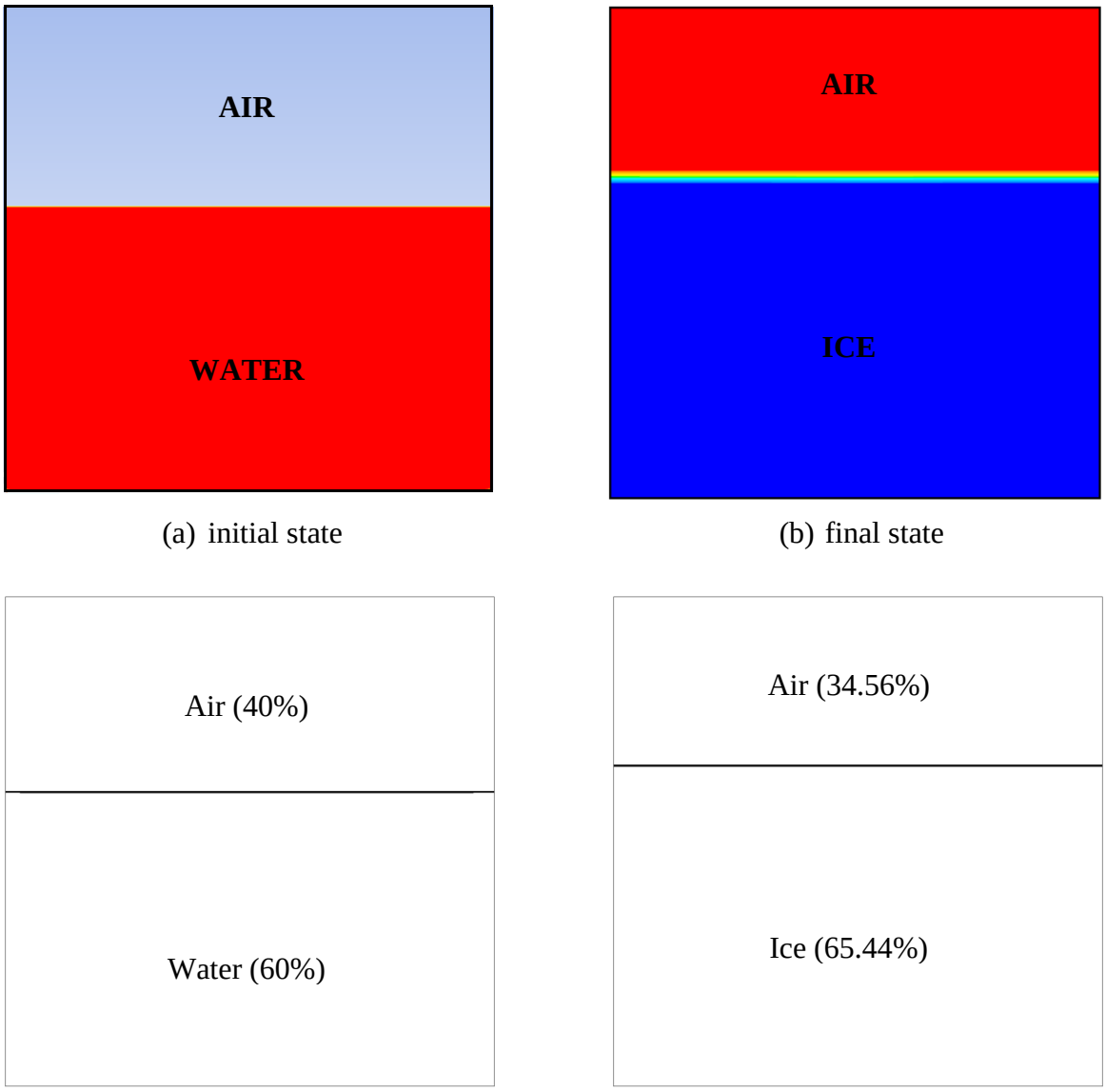

(a) initial state

(b) final state

(c) air-water interface at initial condition

(d) air-ice interface at final condition

Figure B.4 Comparison of the initial and final states of solidification, representing 9.07% volume expansion of water within the square cavity.

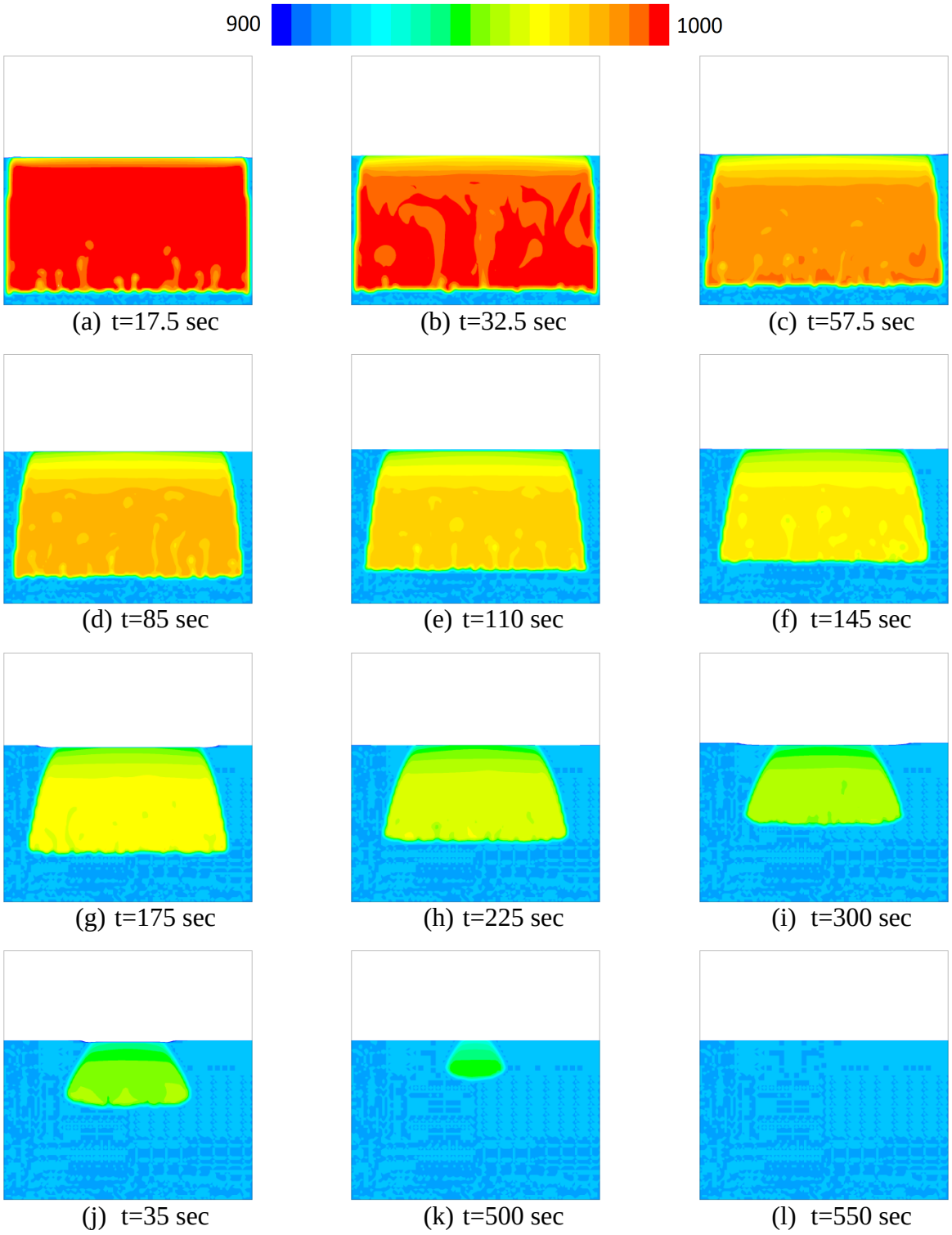

Figure B.5 Evolving contours of density during freezing of water at selected time instants (the density range is from 900 to 1000 kg/m^3).